INVESTIGATING THE LIMIT OF THREE-PHOTON MICROSCOPY IN BRAIN IMAGING

A Dissertation

Presented to the Faculty of the Graduate School

of Cornell University

in Partial Fulfillment of the Requirements for the Degree of

Doctor of Philosophy

by

Mengran Wang

May 2019

INVESTIGATING THE LIMIT OF THREE-PHOTON MICROSCOPY IN BRAIN IMAGING

Mengran Wang, Ph.D.

Cornell University 2019

One of the main challenges to understand how brain works is to map out all of the neurons as well as their activities. The requirement of breadth, depth as well as precision triggers a search for new tools. Two-photon microscopy (2PM) has been widely used in brain studies since its invention in 1990. However, the fundamental limit of signal-to-background-ratio (SBR) stops 2PM from imaging deep into biological sample.

Three-photon microscopy (3PM) combines longer-wavelength excitation and higher order of nonlienarity to achieve deeper tissue penetration. Light attenuation in thick biological tissues, caused by a combination of absorption and scattering, limits the imaging depth in multiphoton microscopy (MPM). Both tissue scattering and absorption are dependent on wavelengths, which makes it essential to choose the right wavelength with minimum attenuation for deep imaging. Tissue scattering and absorption impact the excitation and emission light in different ways for multiphoton imaging. In this thesis, I will describe the key points in selecting the optimum excitation wavelengths and emission wavelengths theoretically and experimentally. We show that the excitation wavelength has more impact on imaging depth than emission wavelength and the advantage of long wavelength dyes for multiphoton deep imaging is almost entirely due to the long excitation wavelengths.

Then we applied three-photon microscopy to image the subventricular zone

(SVZ), which is a heterogeneous neurogenic stem cell niche deep in the brain. We show 3PM visualisation of typical neural stem cells (NSC), intermediate progenitors and neuroblasts in both postnatal and adult SVZ. 3PM provides the first non-damaging opportunity to image the SVZ, distinguish cell morphologies in live animals and has the potential of dynamically imaging stem cell lineage progression in situ at various ages.

Lastly, we did chronic neural activity imaging in *Drosophila* and captured neural structure and activity through the intact fly cuticle. We performed chronic functional imaging of odour-evoked neural activity in the mushroom body Kenyon cells and found odour responses changed over time; sharp odour evoked responses gradually switched to persistent neural activity. This demonstrates that three-photon microscopy extends the time limits of the current *in vivo* imaging methods used in flies for anatomical and functional imaging, and opens up new ways to chronically capture neural activity from the fly brain.

BIOGRAPHICAL SKETCH

Mengran Wang was born in Shandong, China in 1992. After finishing her undergraduate studies in the University of Science and Technology of China, she came to Cornell in the summer of 2014 to pursue her Ph.D. and a year later joined Prof. Chris Xu's lab to work on three-photon brain imaging research.

This document is dedicated to my family.

ACKNOWLEDGEMENTS

I would like to thank my advisor Professor Chris Xu, who gave me tremendous support and freedom for me to learn and to grow. I am always impressed by his professional perspective, depth of knowledge and rigorous scholarship, which has deeply influenced my way of thinking and my working attitudes. Without his guidance, support and inspiration during the most critical period of my Ph.D. journey, I would not have been able to accomplish this study.

I would like to thank Prof. Nilay Yapici, who has been encouraging and supportive about our collaborating projects. Her enthusiasm kept inspiring me in the past two years. I would like to thank my collaborator Max Aragon, who never ceases to amaze me as a quick learner and problem solver during the two years of collaboration. I wish you all the success in your graduate school and your future life. I would also like to thank my collaborator and friend Dr. Bin Sun, whose positive attitudes and the courage to pursue the dream truly impressed me.

I would like to thank Professor Warren Zipfel and Professor Clifford Pollock for your support and advice as members of my dissertation committee and Professor Lois Pollack for being the faculty member representing the Biophysics field. I would like to thank all the professors who supported and inspired my research and learning at Cornell.

I would also like to thank all the members and alumni in Xu Group. I would like to thank Dr. Dimitre Ouzounov, Dr. David Sinefeld, Dr. Bo Li, Dr. Kriti Charan, Dr. Tianyu Wang, Dr. Xusan Yang, Dr. Kibaek Choe, Dr. Yusaku Hontani, Fei Xia, Najva Akbari, Chunyan Wu, Aaron Mok, Thomas Ciavatti, Yifan Qin, Chi Huang and Minsu Kim for their scientific advice and knowledge and many insightful discussions and suggestions. They are my primary resource

for getting my science questions answered and was instrumental in helping me finish this thesis. It is a great to have become colleagues and friends with you and I had great pleasure working with you. I wish all of you great success in the future.

Finally, I would like to thank my parents and my grandparents for their unconditional care and love during my life. I am so blessed to be born in such a loving family. Life is hard, but I know you will always be there with me. I would also like to thank all my friends in the US and in China. Life is more interesting and colorful because of you.

TABLE OF CONTENTS

LIST OF TABLES

LIST OF FIGURES

CHAPTER 1

INTRODUCTION AND OVERVIEW

1.1 Introduction of multiphoton microscopy

Broadly speaking, multiphoton microscopy can be referred to any microscopy method that involves the process of nonlinear interaction of photons with matter. Here, we will focus on two categories: two-photon excited fluorescence (2PEF) and three-photon excited fluorescence (3PEF). In multiphoton microscopy, as the name suggests, fluorescent molecules absorb multiple photons (usually two/three photons) simultaneously to transition from ground states to excited states, as opposed to only one photon absorbed in conventional fluorescence microscopy. Since the excited molecules emit only one photon to return to the ground state, this emitted photon possesses higher energy than the excitation photons, leading to a red shift of excitation photons compared to emitted single photon (see Fig. 1.1).

Since its invention [5], two-photon microscopy (2PM) has found wide applications in biology due to its performance in depth penetration through scattering tissues with high spatial resolution. (For reviews on two-photon microscopy, see ref. [6, 7, 18, 22, 12, 30, 11, 20]). The concept of three-photon excitation (3PE) was proposed decades ago, yet, due to the limitations of laser source and the lack of clear motivation, three-photon microscopy (3PM) has not been brought to reality until recently [13, 15]. 3PM improves the SBR limit by another few orders of magnitude. Together with the longer excitation wavelengths, 3PM provides the ability to penetrate deeper into the intact mouse brain than 2PM.

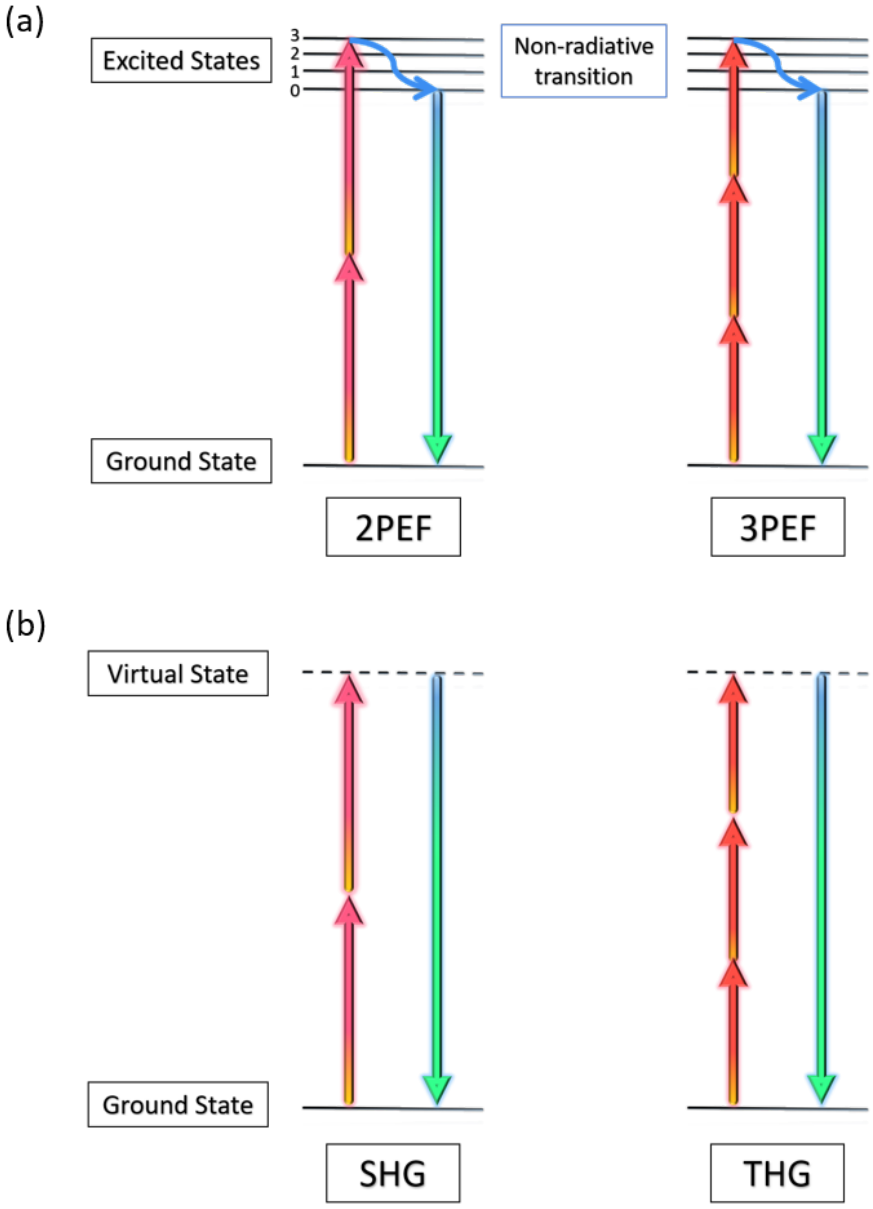

Figure 1.1: Energy diagram of different imaging modalities. (a) Two-photon excited fluorescence (2PEF) and three-photon excited fluorescence (3PEF). (b) Second-harmonic generation (SHG) and third-harmonic generation (THG). Solid lines representing real energy states, dashed lines representing virtual energy states.

1.2 Second harmonic generation and third harmonic generation

Unlike multiphoton excited fluorescence, second harmonic generation (SHG) and third harmonic generation (THG) are both parametric processes, in which there is no real change in molecular state after excitation. This means that the response time of these processes are much shorter than that of fluorescence. The difference between 2PEF/3PEF and SHG/THG is demonstrated in Fig. 1.1.

The label-free nature of SHG and THG imaging has advantage in photobleaching and phototoxicity [16]. In addition, the fact that no labeling is needed enables imaging samples which are hard to be stained or physiology-changed after staining.

The SHG and THG signal depends on the nth-order sus-ceptibility of the material. SHG is good for imaging structures without inversion symmetry such as collagen and microtubules [29, 9]. THG is more versatile since all materials have non-zero third-order susceptibility. THG signal is used for imaging interface with different refractive indices or with different nonlinear susceptibilities [1].

Based on the slight difference of emission wavelength between 2PEF/3PEF and SHG/THG, the two emission channels could be separated during imaging. Implementing SHG or THG into a MPM is easy since most of the requirements are similar except the simple change of detection filters, which is also why SHG or THG channels always exists in parallel with multiphoton fluorescence channels.

Specifically for THG, the thick myelin sheath structure in brain white matter, which functions to speed up impulse propagation in nervous system, gives a strong THG signal [8], which complements three-photon fluorescence imaging by locating the white matter inside a live brain.

1.3 Advantage of three-photon microscopy

The advantage of 3PM in deep tissue imaging lies in two aspects. On one hand, long excitation wavelengths used in 3PM tends to reduce tissue scattering, thus reducing the tissue attenuation potentially. Penetration depth is determined by the tissue attenuation. With the same level optical power imposed on the sample, less tissue attenuation allows for deeper penetration, whereas more tissue attenuation limits the penetration depth. On the other hand, 3PE has better 3D localization due to the use of higher (3rd) order of nonlinearity, creating orders-of-magnitude improvement in SBR.

The requirement of simultaneous absorption of three photons gives rise to the relation of signal proportional to the light intensity cubic:

$$F_{3P} \propto I^3 \tag{1.1}$$

where F_{3P} is the fluorescence signal in 3PM, I is the excitation light intensity. Whereas in 2PM, fluorescence is proportional to the light intensity squared, $F_{2P} \propto I^2$.

This leads to more localized fluorescence occurring at the focal point in 3PM, which has the highest light intensity and less fluorescence excitation from out-of-focus planes.

1.4 Instrumental requirements for three-photon microscopy

1.4.1 Choosing the right objectives

In conventional microscopy, high NA objective is used in order to construct a high resolution image. In general, such a high NA objective, is easier to design with small focal length. In addition, the fixed number of imaging pixels limits the field of view in the high-resolution image, therefore, high NA objectives are normally associated with high magnification and small field of view. In laser scanning microscopy, however, the situation is different since the image is constructed by the scanning beam, and there is no limit by the pixels in the collection channel. If the magnification of the objective is too high, the field of view of the scanning beam will be too small. Thus, the objectives being used in MPM should have high NA in order to generate small excitation volume, but relatively small magnification.

Besides, from collection point of view, higher NA and low magnification objectives result in higher collection efficiency due to the large angles and collection area supported by the objective. In general, high NA and low magnification objectives are preferred in MPM, where every emitted photon is precious.

Excitation volume vs NA for 2PM and 3PM

In multiphoton microscopy, excitation volume is a more practical term to describe the effect of 3D localization rather than full-width-at-half-maximum (FWHM) used to describe spatial resolutions in conventional optical imaging. In single-photon microscopy, due to the linear dependence of signal to light in-

tensity ($F \propto I$), the excitation volume is dependent on sample thickness. However, for MPM, the spatial localization property makes it independent on sample thickness as long as the sample is thick enough compared to focal volume, enabling to utilize the term excitation volume.

Through calculations [25], we got focal volume for multiphoton excitation is

$$V \propto \frac{n_0 \, \lambda^3}{NA^4} \tag{1.2}$$

Where n_0 is the refractive index of objective immersion medium, λ is the excitation wavelength

From this equation, larger NA leads to a tighter excitation volume, which potentially increases the 3D localization during multiphoton imaging.

Total fluorescence excitation vs NA for 2PM and 3PM

High NA setting brings a tighter focus and better 3D localization, but shrunken excitation volume may reduce the total signal level. The trade-off between higher light intensity at the focus and reduced excitation volume urges us to examine the dependence of total fluorescence on NA. By integrating the excitation distribution over the excitation volume, we get the total fluorescence excitation for 2PE:

$$F \propto \int_V I^2 dV \propto \frac{n_0 P^2}{\lambda} \tag{1.3}$$

For 3PE:

$$F \propto \int_V I^3 dV \propto \frac{n_0 (NA)^2 P^3}{\lambda^3} \tag{1.4}$$

Here we conclude that for 2PE, the total fluorescence is independent of NA, however, for 3PE, it is proportional to the square of NA. An intuitive way to un-

derstand this discrepancy is that the quadratic dependence on intensity in 2PM leads to complete counteractions between the trade-off in higher focal intensity and shrunken excitation volume. For three-photon excitation however, the cubic dependence on intensity places more importance on focal intensity which leads to an overall preference for higher NA.

Taking into account of all the above considerations, high NA objective is essential in 3PM while preferred in 2PM. The common practice in multiphoton fluorescence microscopy was to overfill the back aperture to maximize signal and to get the highest resolution [1]. For example, under scalar approximation, 3PM and 4PM signals are proportional to NA^2 and NA^4 , respectively. This means overfilling the back aperture of the objective lens maximizes the signal. Underfilling leads to a decrease in the effective NA and signal reduction. However, we realize that in deep-tissue 3PM and 4PM, there is a competing effect that could lead to signal reduction as the back aperture became more filled: The rays converging at a larger angle will experience more attenuation than those at smaller angles (see Fig. 1.1). Consequently, for fixed power deposited on the sample after the objective lens, the more the lens filled, the smaller the signal due to the excessive loss experienced by the large-angle rays.

1.4.2 Choosing the right lasers

3PE has a different requirement from 2PE in terms of laser specifications. The higher order nonlinearity requires more photons to arrive simultaneously to excite the molecule compared to two-photon scenario. This reduces the probability of excitation by orders of magnitude, which is characterized by the term

cross section [24, 23]. The small cross section of three-photon excitation requires higher light intensity at focal point, which can be achieved spatially and temporally.

Spatially, tighter focus is achieved by higher NA, which has been discussed above.

Temporally, in order to achieve high photon density, an ultra-short pulsed laser is essential for MPM. The fluorescence signal is dependent on the peak intensity I_{peak}, thus, we have

$$F_n \propto \int I_{\text{peak}}^n dt = \left(\frac{\langle I \rangle}{f\tau}\right)^n (f\tau) = \frac{\langle P \rangle^n}{(f\tau)^{n-1}} \tag{1.5}$$

Where f is the repetition rate and τ is the pulse width, $f\tau$ gives duty cycle, which indicates the faction of the pulses duration over one cycle. $\langle I \rangle$ is average power which is given by:

$$\langle I \rangle = I_{peak}\ (f\tau) \tag{1.6}$$

So for two-photon process (n=2), the signal is inversely proportional to the duty cycle, and for three-photon process (n=3), the signal is inversely proportional to the duty cycle square. In order to get a reasonable signal, we need laser sources with short pulse width and low repetition rate at a given average power.

Besides boosting the signal level, it is also important to maintain low average power on the biological sample especially for *in vivo* imaging. The limit for maximum power which could be put on the brain *in vivo* without causing damage is dependent on wavelength. 3PM at the longer wavelength windows lowers the maximum permissible power when compared to 2PM because of the

strong water absorption in the long wavelength spectral range. Thus the requirement of higher peak power and lower average power makes it essential to use low-repetition-rate laser sources in 3PM.

Standard Ti-Sapphire lasers that are commonly used as excitation source for two-photon imaging are not suitable for 3PM because their spectral range cannot reach the longer wavelengths needed as well as their high repetition rate.

Recently, a number of new laser sources have been developed for the purpose of three-photon imaging.

One option is to use fiber lasers which can supply high pulse energy (μJ) with low repetition rate. The main difficulty is that such sources are usually fixed around 1550nm or 1060 nm, which is not optimum for 3PM imaging. Nevertheless, it is possible to use such a laser in combination with soliton self-frequency shift (SSFS) [31, 21] in a fiber or photonic-crystal (PC) rod. In this way it is possible to shift the wavelength to 1700 nm. This solution is limited though in the pulse energy that can be transferred through the photonic-crystal rod.

Another option, which allows much higher pulse energies at long wavelength range, is to use optical parametric amplifier (OPA) which is pumped with a amplifier. Such systems were developed a few years ago, but they fit mostly to the technical requirements of 3PM.

1.4.3 Choosing the right detectors

Avalanche photodiodes (APD) have internal gain comparable to normal photodiodes (PD), which enables sensitive and single-photon detection. However,

the small active area limits its applications in MPM. Due to the wide-field fluorescence collection settings used in MPM, there is a need for high efficiency and high gain detectors with large detection area. Photomultiplier tubes (PMT) are the main currently used in MPM.

PMT utilizes photoelectric effect to convert photons to photoelectrons with internal gain. The photocathode utilizes photoelectric effect to convert photons to photoelectrons. The conversion efficiency is determined by the photocathode sensitivity and is dependent on wavelengths. The photocathode material is selected based on the spectral response, quantum efficiency. Several parameters are relevant to choose among different PMTs. Spectral response is usually characterized by quantum efficiency and radiant sensitivity. Quantum efficiency (QE) is defined as the ratio of the number of photoelectrons emitted from the photocathode to the number of incident photons.

Radiant sensitivity (S) is the photoelectric current from the photocathode divided by the incident radiant power at a given wavelength, expressed in A/W.

QE and S have the following relationship: $QE = \frac{1240xS}{\lambda}x100\ (\%)$, where λ is the wavelength in nm.

The photocathode is usually set at high negative voltage relative to the anode, so that the photoelectrons can be accelerated from the photocathode to the dynode. Each accelerated electron can produce multiple secondary electrons on the next dynode, thus each electron is amplified to multiple electrons. And each generated secondary electrons will repeat the same process on the subsequent dynodes, thus each initial electron is amplified to multiple electrons and eventually reach the anode to be converted to photoelectric current. The in-

ternal gain, depending on the applied voltage, enables the detection of single photons. The gain is defined as the ratio of the anode output current to the photoelectric current from the photocathode. The dark noise is referring that there is current even if no light is incident on the PMT, which is mainly induced by the thermionic emission of electrons, which can be controlled by reducing the operating temperature.

GaAsP is the most commonly used PMT for fluorescence detection at visible range (400-650 nm). GaAs PMTs extend the spectral range to around 850 nm, which can be used for near-infrared (NIR) fluorescence detection, with slightly lower QE. The small effective area necessities the use of focusing lens for fluorescence collection. Ultra bialkali (UBA) PMT (Hamamatsu, R7600U-200) which is light-weight with large effective area makes it ideal for THG signal detection (centered at 433 nm for 1300 nm excitation and 567 nm for 1700 nm excitation).

1.5 Limit the damage in three-photon microscopy

Water absorption increases dramatically when the wavelength is beyond the range of 1um, which poses a big challenge for imaging with long excitation wavelengths since water occupies approximately 70% of the total weight in brain, 70% in heart and 80% in lungs of human body. The excitation spectra window for 3PM is located in the infrared (IR) region, which overlaps with the water absorption spectra. For this reason, the maximum average power that can be put on the biological sample is limited in order to reduce the heating effect especially for *in vivo* experiments. For *in vivo* 2PM in the near IR, absorption by the blood dominates.

The heating effect is dependent on wavelength, imaging duration and tissue variance [17]. In general, tissue just below the surface is especially vulnerable to linear absorption, and this is because the surface bears the highest average power but is also eased due to the dissipation of heat with the help of cranial window and immersion medium. One approach to limit the average power imposed on the sample is to increase the peak power while keeping the average power the same. This can be easily achieved by reducing the repetition rate of the laser pulse. The pulse energy can be calculated by the ratio of the average power to the repetition rate, so more energetic pulses can be generated by reducing the repetition rate. However, high pulse energy tends to induce nonlinear damage at the focal point, which sets a lower limit to the repetition rate. Besides, 3P fluorophore saturation occurs at pulse energy typically several times below the nonlinear ablative threshold.

1.6 Applications in neural activity imaging

MPM can measure dynamics of nervous system through fluorescence change during imaging. Calcium ions play an essential role in cellular signaling, specifically for nervous system. When a neuron is firing, calcium channels will open and a large number of calcium ions will flow in and fill in the neuronal cytoplasm. The big difference in the intracellular calcium concentrations between silent and active state makes it a perfect candidate as an indicator of neuronal activity [10].

Calcium indicators undergo conformational change by binding to calcium ions, and change fluorescence properties. Thus, combining with optical imag-

ing, neuronal activity will be reflected by fluorescence change. This allows us to watch the activity of a group of neurons simultaneously. Calcium indicators provide a tool to optically probe intracellular calcium concentrations which enables dynamic measurement of brain function. Both chemical indicators and generically encoded calcium indicators (GECIs) are used extensively in imaging research [19, 26].

GCaMPs [14, 3], as a group of green GECIs, are powerful fluorescent tools for brain activity imaging due to its high sensitivity and high signal-to-noise-ratio (SNR). More work is being done to extend the spectral window of GECIs to add flexibility in imaging. Red GECIs [28, 4], which are a group of newcomers in the field of calcium indicators, has been drawing more and more attention to neuroscientists. The advantage of less scattering using longer excitation wavelengths gives them the potential for imaging deeper tissue. More importantly, the unique strength in combining optogenetics [2, 27] and calcium imaging makes it a new favorite, which is hard to achieve for GCaMPs due to the overlap in excitation spectra. Combining calcium imaging with optogenetics provides a platform of optical interrogation of nervous system by simultaneous manipulating and recording neural activity.

Bibliography

[1] Y. Barad, H. Eisenberg, M. Horowitz, and Y. Silberberg. Nonlinear scanning laser microscopy by third harmonic generation. 70(8):922–924.

[2] Edward S. Boyden, Feng Zhang, Ernst Bamberg, Georg Nagel, and Karl

Deisseroth. Millisecond-timescale, genetically targeted optical control of neural activity. 8(9):1263–1268.

[3] Tsai-Wen Chen, Trevor J. Wardill, Yi Sun, Stefan R. Pulver, Sabine L. Renninger, Amy Baohan, Eric R. Schreiter, Rex A. Kerr, Michael B. Orger, Vivek Jayaraman, Loren L. Looger, Karel Svoboda, and Douglas S. Kim. Ultrasensitive fluorescent proteins for imaging neuronal activity. *Nature*, 499(7458):295–300, July 2013.

[4] Hod Dana, Boaz Mohar, Yi Sun, Sujatha Narayan, Andrew Gordus, Jeremy P. Hasseman, Getahun Tsegaye, Graham T. Holt, Amy Hu, Deepika Walpita, Ronak Patel, John J. Macklin, Cornelia I. Bargmann, Misha B. Ahrens, Eric R. Schreiter, Vivek Jayaraman, Loren L. Looger, Karel Svoboda, and Douglas S. Kim. Sensitive red protein calcium indicators for imaging neural activity. *eLife*, 5:e12727, March 2016.

[5] W. Denk, J. H. Strickler, and W. W. Webb. Two-photon laser scanning fluorescence microscopy. 248(4951):73–76.

[6] Winfried Denk, David W. Piston, and Watt W. Webb. Two-photon molecular excitation in laser-scanning microscopy. pages 445–458.

[7] Winfried Denk and Karel Svoboda. Photon upmanship: Why multiphoton imaging is more than a gimmick. 18(3):351–357.

[8] Matthew J. Farrar, Frank W. Wise, Joseph R. Fetcho, and Chris B. Schaffer. In vivo imaging of myelin in the vertebrate central nervous system using third harmonic generation microscopy. 100(5):1362–1371.

[9] Isaac Freund and Moshe Deutsch. Second-harmonic microscopy of biological tissue. 11(2):94–96.

[10] Christine Grienberger and Arthur Konnerth. Imaging calcium in neurons. 73(5):862–885.

[11] Fritjof Helmchen and Winfried Denk. Deep tissue two-photon microscopy. 2(12):932–940.

[12] Fritjof Helmchen and Winfried Denk. New developments in multiphoton microscopy. 12(5):593–601.

[13] Nicholas G. Horton, Ke Wang, Demirhan Kobat, Catharine G. Clark, Frank W. Wise, Chris B. Schaffer, and Chris Xu. *In vivo* three-photon microscopy of subcortical structures within an intact mouse brain. *Nat. Photonics*, 7(3):205–209, March 2013.

[14] Junichi Nakai, Masamichi Ohkura, and Keiji Imoto. A high signal-to-noise ca2+ probe composed of a single green fluorescent protein. 19(2):137–141.

[15] Dimitre G. Ouzounov, Tianyu Wang, Mengran Wang, Danielle D. Feng, Nicholas G. Horton, Jean C. Cruz-Hernndez, Yu-Ting Cheng, Jacob Reimer, Andreas S. Tolias, Nozomi Nishimura, and Chris Xu. In vivo three-photon imaging of activity of GCaMP6-labeled neurons deep in intact mouse brain. 14(4):388–390.

[16] Periklis Pantazis, James Maloney, David Wu, and Scott E. Fraser. Second harmonic generating (SHG) nanoprobes for in vivo imaging. 107(33):14535–14540.

[17] Kaspar Podgorski and Gayathri Ranganathan. Brain heating induced by near-infrared lasers during multiphoton microscopy. 116(3):1012–1023.

[18] Peter T. C. So, Chen Y. Dong, Barry R. Masters, and Keith M. Berland. Two-photon excitation fluorescence microscopy. 2(1):399–429.

[19] Christoph Stosiek, Olga Garaschuk, Knut Holthoff, and Arthur Konnerth. In vivo two-photon calcium imaging of neuronal networks. 100(12):7319–7324.

[20] A. Ustione and D.w. Piston. A simple introduction to multiphoton microscopy. 243(3):221–226.

[21] Ke Wang and Chris Xu. Tunable high-energy soliton pulse generation from a large-mode-area fiber and its application to third harmonic generation microscopy. 99(7):071112.

[22] Rebecca M Williams, Warren R Zipfel, and Watt W Webb. Multiphoton microscopy in biological research. 5(5):603–608.

[23] C Xu, W Zipfel, J B Shear, R M Williams, and W W Webb. Multiphoton fluorescence excitation: new spectral windows for biological nonlinear microscopy. 93(20):10763–10768.

[24] Chris Xu and Watt W. Webb. Measurement of two-photon excitation cross sections of molecular fluorophores with data from 690 to 1050 nm. 13(3):481–491.

[25] Chris Xu and Watt W. Webb. Multiphoton excitation of molecular fluorophores and nonlinear laser microscopy. In *Topics in Fluorescence Spectroscopy*, volume 5, pages 471–540. Springer, New York, 1997.

[26] Rafael Yuste and Winfried Denk. Dendritic spines as basic functional units of neuronal integration. 375(6533):682–684.

[27] Feng Zhang, Li-Ping Wang, Martin Brauner, Jana F. Liewald, Kenneth Kay, Natalie Watzke, Phillip G. Wood, Ernst Bamberg, Georg Nagel, Alexander

Gottschalk, and Karl Deisseroth. Multimodal fast optical interrogation of neural circuitry. 446(7136):633–639.

[28] Yongxin Zhao, Satoko Araki, Jiahui Wu, Takayuki Teramoto, Yu-Fen Chang, Masahiro Nakano, Ahmed S. Abdelfattah, Manabi Fujiwara, Takeshi Ishihara, Takeharu Nagai, and Robert E. Campbell. An expanded palette of genetically encoded ca2+ indicators. 333(6051):1888–1891.

[29] Warren R. Zipfel, Rebecca M. Williams, Richard Christie, Alexander Yu Nikitin, Bradley T. Hyman, and Watt W. Webb. Live tissue intrinsic emission microscopy using multiphoton-excited native fluorescence and second harmonic generation. 100(12):7075–7080.

[30] Warren R. Zipfel, Rebecca M. Williams, and Watt W. Webb. Nonlinear magic: multiphoton microscopy in the biosciences. 21(11):1369–1377.

[31] B. Zysset, P. Beaud, and W. Hodel. Generation of optical solitons in the wavelength region 1.371.49 m. 50(16):1027–1029.

CHAPTER 2

COMPARING THE EFFECTIVE ATTENUATION LENGTHS FOR LONG WAVELENGTH *IN VIVO* IMAGING OF THE MOUSE BRAIN

2.1 Abstract

Light attenuation in thick biological tissues, caused by a combination of absorption and scattering, limits the penetration depth in multiphoton microscopy (MPM). Both tissue scattering and absorption are dependent on wavelengths, which makes it essential to choose the excitation wavelength with minimum attenuation for deep imaging. Although theoretical models have been established to predict the wavelength dependence of light attenuation in brain tissues, the accuracy of these models in experimental settings needs to be verified. Furthermore, the water absorption contribution to the tissue attenuation, especially at 1450 nm where strong water absorption is predicted to be the dominant contributor in light attenuation, has not been confirmed. Here we performed a systematic study of *in vivo* three-photon imaging at different excitation wavelengths, 1300 nm, 1450 nm, 1500 nm, 1550 nm, and 1700 nm, and quantified the tissue attenuation by calculating the effective attenuation length at each wavelength. The experimental data show that the effective attenuation length at 1450 nm is significantly shorter than that at 1300 nm or 1700 nm. Our results provide unequivocal validation of the theoretical estimations based on water absorption and tissue scattering in predicting the effective attenuation lengths for long wavelength *in vivo* imaging. [1]

[1]This chapter has been published in Biomedical Optics Express: vol 9, issue 8, https://doi.org/10.1364/BOE.9.003534

2.2 Introduction

Multiphoton microscopy (MPM) enables deep imaging in highly scattering biological tissues due to the use of nonlinear excitation and long excitation wavelengths [7, 8, 12, 21]. It has been demonstrated that the multiphoton excited fluorescence signal within the focal volume is mostly generated by ballistic photons (photons that maintain their ballistic trajectories). When imaging deep in scattering biological samples such as the mouse brain, the number of ballistic photons arriving at the focus is significantly reduced due to the absorption and scattering by the tissue [30, 9], characterized by the effective attenuation length (EAL). The ballistic photons as a function of depth (z) can be expressed as:

$$P_z = P_0 e^{-\frac{z}{l_e}}. \tag{2.1}$$

where P_z is the optical power at the focus, P_0 is the optical power on the sample surface, and l_e is the EAL.

The loss of ballistic photons reduces the fluorescence generation. In order to obtain sufficient signal from the focus, the exponential decay of the excitation light needs to be compensated by increasing the total optical power at the surface. Obviously, with the same excitation power, less tissue attenuation (or longer EAL) will allow for deeper tissue penetration [20].

Light attenuation in biological tissues is a combined effect of absorption and scattering. Using mouse brain tissue *in vivo* as an example, at wavelengths between 700 nm and 1060 nm—the wavelength tuning range of the mode-locked Ti:S laser—attenuation of the excitation light is completely dominated by tissue scattering [11], while the absorption (mostly by blood for *in vivo* imaging) is relatively low [23, 10, 14]. Longer wavelengths at approximately 1200 nm–

1850 nm are advantageous for deep brain imaging due to the reduction of light scattering. However, water absorption (water content is >70% in brain tissues [22]) increases significantly in this spectral region and becomes the dominant absorber for *in vivo* imaging. Both water absorption and tissue scattering contribute to the attenuation of the excitation light, therefore, the optimum choice of the excitation wavelength is a trade-off between these two factors. The theoretical model of calculating l_e (Fig. 2.1) is then [12]:

$$\frac{1}{l_e} = \frac{1}{l_a} + \frac{1}{l_s}. \tag{2.2}$$

where l_a is the water absorption length [19], and l_s is the scattering mean-free path, calculated using Mie scattering for a tissue-like colloidal solution containing 1-μm diameter beads at a concentration of 5.4x10^9 beads/mL [25, 4, 26].

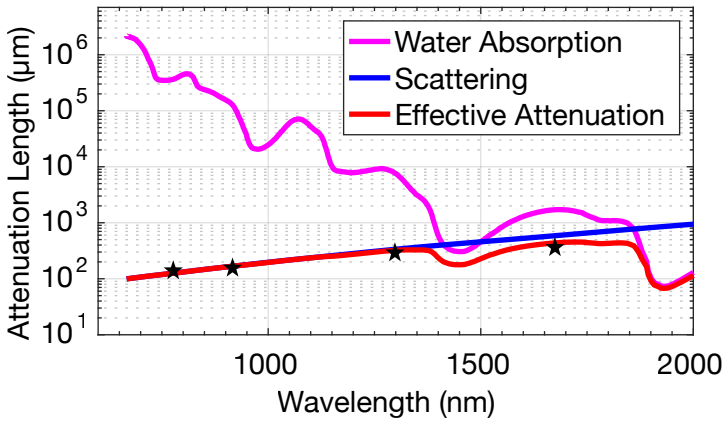

Figure 2.1: Theoretical model of the effective attenuation lengths based on water absorption and Mie scattering. The black stars indicate the reported effective attenuation lengths in mouse brains *in vivo*, 131 μm at 775 nm [17], 152~158 μm at 920 nm [28], 305~319 μm at 1300 nm [28] and 383 μm at 1680 nm [12].

Theoretical estimations based on tissue absorption and scattering predict that the longer excitation wavelength approach is advantages for deeper tissue imaging (Fig. 2.1), and previous experimental works have shown that the

longer wavelength windows of 1300 nm [17, 1, 28, 24, 18, 5] and 1700 nm [12, 5] outperform the shorter wavelengths, such as 775 nm [17], 800 nm [1, 31], 830 nm [16, 15], 920 nm [25, 28, 2], by a factor of 2 to 3 times in terms of imaging depth. However, the attenuation at these wavelengths are all dominated by scattering (i.e., l_a is at least several times larger than l_s). As previous experimental data all lie close to the scattering curve (the blue line in Fig. 2.1), it indicates that scattering alone, without any consideration of the absorption, would have predicted similar wavelength dependence. In particular, the absorption-scattering model predicts that the long wavelength window is not one continuous window. Instead, it indicates that there are two windows for mouse brain imaging centered at ~ 1300 nm and 1700 nm, with a gap at ~ 1450 nm due to strong water absorption (Fig. 2.1). In this paper, we compared the effective attenuation lengths at the excitation wavelengths of 1300 nm, 1450 nm, 1500 nm, 1550 nm, and 1700 nm in mouse brains *in vivo*. Our results confirm the existence of the water absorption feature in the wavelength dependence of EAL, and provide unequivocal support for the absorption-scattering model for ballistic photon penetration.

2.3 Characterization of the excitation source at 1700 nm, 1550 nm, 1500 nm, and 1450 nm

The three-photon imaging setup is similar to that described previously [12, 21]. The excitation source was a wavelength-tunable optical parametric amplifier (OPA, Opera-F, Coherent) pumped by a Monaco amplifier (Coherent) operating at 330 kHz repetition rate. The excitation pulse spectra at 1700 nm, 1550 nm, 1500 nm, and 1450 nm were measured by an Optical Spectrum Analyzer (OSA,

Thorlabs), shown in Fig. 2.2 a.

We measured the dependence of the fluorescence from Texas Red on the excitation power at 1700 nm and 1450 nm to ensure three-photon excitation (Figs. 2.2 b and 2.2 c). The generated fluorescence was detected by a photomultiplier tube (PMT) with a GaAsP photocathode (H7422-40, Hamamatsu Photonics), and recorded by a photon counter (SR400, Stanford Research Systems). The slopes in the log-log plots confirmed three-photon excitation for Texas Red at both 1700 nm and 1450 nm.

Dispersion from the optics in the microscope were pre-compensated using a Si wafer (Edmund Optics) placed at the Brewster angle [13]. Second-order interferometric autocorrelations were performed after the objective lens at each wavelength (Fig. 2.3).

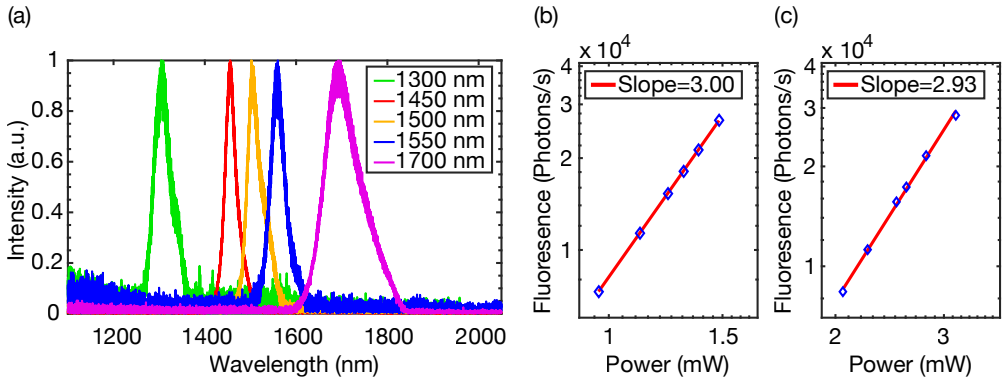

Figure 2.2: (a) Measured spectra of the laser source operating at 1700 nm, 1550 nm, 1500 nm, 1450 nm and 1300 nm. Dependence of three-photon-excited fluorescence on excitation power for (b) 1700 nm and (c) 1450 nm in logarithmic scales. The blue diamonds are the measured data, and the red lines are linear fits to the experimental results. The slope is indicated in each figure.

The excitation beam size at the back aperture of the objective lens impacts the measurements of the EALs, since the marginal rays have longer path lengths in

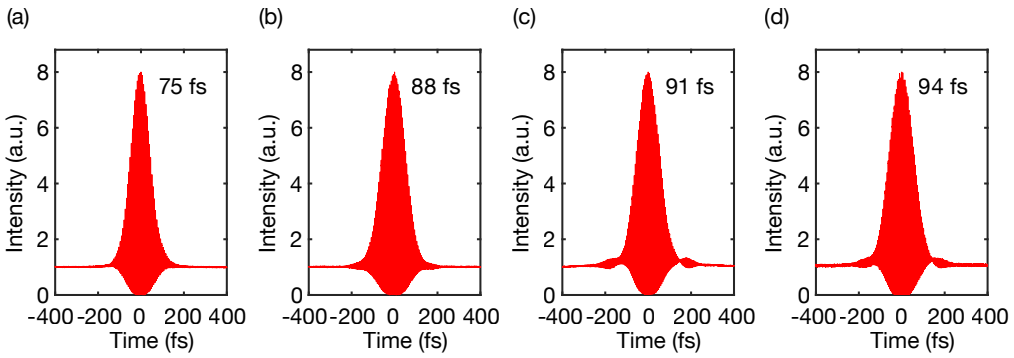

Figure 2.3: Measured second-order interferometric autocorrelations of the laser pulse operating at (a) 1700 nm, (b) 1550 nm, (c) 1500 nm, and (d) 1450 nm. The intensity full-width-at-half-maximum (FWHM) of the pulse is indicated in each figure, assuming a deconvolution factor of 1.54 for sech^2-pulse.

the tissue and experience more attenuation than the chief rays at the center of the lens. To ensure there is no systematic bias in the EAL measurements, we characterized the beam size at each excitation wavelength (Fig. 2.4) using a calibrated InGaAs camera (Axiom Optics, WiDy SWIR 640). The measurements were taken before the scanner and there is a 6x magnification from the scan mirrors to the back aperture of the objective lens. The beam size variation at these wavelengths is below 6%, which has negligible impact on the EAL measurements [27].

2.4 *In vivo* EAL measurements at 1700 nm, 1550 nm, 1500 nm, and 1450 nm excitation wavelengths

A craniotomy was performed on a 10-week-old wild-type mouse (C57BL/6J) and a glass window was placed directly on the intact dura for imaging. The mouse was anesthetized using isoflurane (3% in oxygen for induction and 1.5–

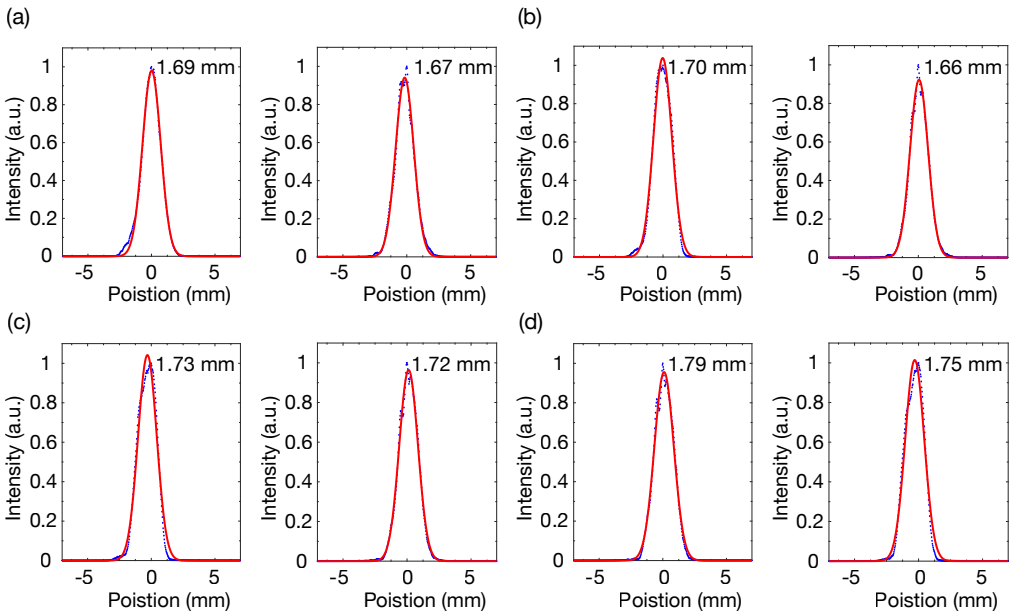

Figure 2.4: Beam size measurements at (a) 1700 nm, (b) 1550 nm, (c) 1500 nm, and (d) 1450 nm. The blue dots are the measured data, and the red lines are Gaussian fits to the measurements. There is some ellipticity in the excitation beam, therefore the measurements were taken along both the long axis (left) and the short axis (right). The FWHM is labeled in each figure.

2% for surgery and imaging to maintain a breathing frequency of 1 Hz). Body temperature was kept at 37.5 °C with a feedback-controlled blanket (Harvard Apparatus), and eye ointment was applied. Dextran-conjugated Texas Red (70kDa, Invitrogen) was injected retro-orbitally for the brain vasculature labeling prior to imaging.

Three-photon imaging was performed in the same intact brain using four different excitation wavelengths, in the order of 1700 nm, 1550 nm, 1500 nm, 1450 nm, and 1700 nm. The 1700 nm excitation was repeated again at the end of the imaging session to ensure that the imaging sequence did not impact the measurements. All imaging were done using the same fluorophore in the same brain regions within the same mouse, which eliminated the uncertainty caused

by the emission-wavelength difference and tissue-to-tissue variation. All images were taken at a frame rate of 0.24 Hz (512 x 512 pixels/frame) with a field of view (FOV) of 340 x 340 µm, and 10 frames were averaged at each depth. The detection path was kept the same for all the wavelengths in this comparison. Thus, the differences in the EALs were only due to the different excitation wavelengths used.

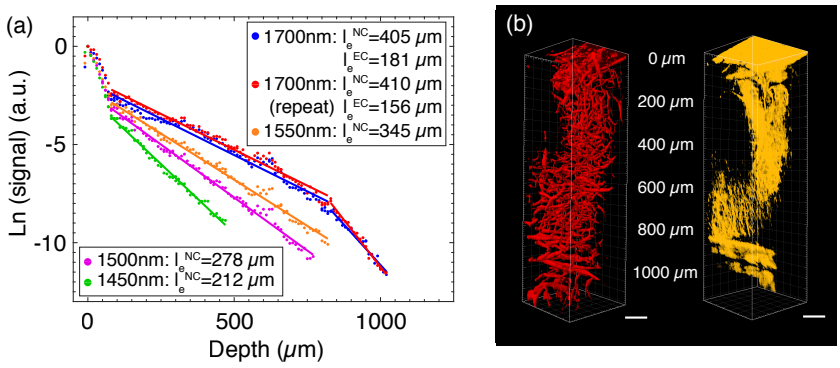

Figure 2.5: (a) Comparison of the fluorescence signal as a function of depth at 1700 nm, 1550 nm, 1500 nm, 1450 nm, and 1700 nm (repeat experiment). The dots are the measured data, and the lines are linear fits to the measurements. With the same maximum average power, imaging at 1700 nm excitation includes both the neocortex (NC) and external capsule (EC), while imaging using the other wavelengths is limited to the NC. (b) 3D reconstruction of three-photon images of Texas Red-labeled brain vasculature, left, fluorescence, right, third harmonic generation (THG). Imaging depths are labeled in the middle. Scale bars, µm.

We acquired approximately 1-mm-deep z-stack, taken at 10-µm depth increment. To avoid potential tissue heating, especially at 1450 nm due to the high water absorption, we kept the maximum average power on the brain surface at 35 mW for all the excitation wavelengths used. Power curves (dependence of the signal value on excitation power) were measured to ensure that no fluo-

rophore saturation (i.e., ground state depletion) occurred at any imaging depth.

The fluorescence signal generated in three-photon microscopy (F_{3P}) is proportional to power cubic [29]. Combining Eq. 2.1, we have:

$$F_{3P} \propto P_z^3 = P_0^3 e^{-\frac{3z}{l_e}}. \tag{2.3}$$

We selected the average value of the brightest 1% of pixels in the x-y image at each depth as the fluorescence signal. In three-photon microscopy (3PM), EAL is defined as the depth at which the normalized signal attenuates by $1/e^3$. By plotting the fluorescence signal as a function of depth, the EALs can be obtained from the slopes of the linear fits in Fig. 2.5 a for the neocortex (NC, 0–840 μm) and the external capsule (EC, 840–1040 μm), assuming the vasculature was labeled homogenously throughout the imaging regions. Measured EALs in the NC at different wavelengths with an uncertainty estimation based on the 95% confidence interval (CI) are: 391~418 μm at 1700 nm, 337~353 μm at 1550 nm, 272~283 μm at 1500 nm, 207~218 μm at 1450 nm, and 398~422 μm at 1700 nm (repeat experiment).

To ensure that the results are not dependent on the selection criteria for the brightest pixels, we varied the selection criteria, and found that this variation did not affect the EAL measurements significantly. Taking the neocortex images acquired at 1700 nm as an example, we selected 0.5% (l_e=400 μm, 386~414 μm with 95% CI), 1% (l_e=405 μm, 391~418 μm with 95% CI), 1.5% (l_e=408 μm, 394~423 μm with 95% CI) and 2% (l_e=410 μm, 396~426 μm with 95% CI) of the brightest pixels. With all the selection criteria between 0.5% and 2%, the resulting EALs vary by ~ 2.5%, which will have no impact on the conclusion of this paper.

We also reconstructed the images from all depths for both fluorescence signal and third harmonic generation (THG) signal. The dense myelin layer in the external capsule (EC) generates strong THG, which allows us to delineate the neocortex and the external capsule (Fig. 2.5 b). Although blood is assumed to be homogeneously distributed within the brain region, the presence of a large blood vessel at the brain surface (see Fig. 2.6 a) results in the steeper slope at the beginning of each decay curve (Fig. 2.5 a, 0–80 μm). Since the brightest pixels are all within this large vessel, the fluorescence signal decays rapidly, reflecting the fact that the attenuation length for blood is much shorter than that of the brain tissue. The measured EALs within this large vessel (0–80 μm, top 1% brightest pixels represented as signal) are: 117 μm at 1700 nm (97~137 μm with 95% CI), 89 μm at 1550 nm (80~98 μm with 95% CI), 81 μm at 1500 nm (76~87 μm with 95% CI), 68 μm at 1450 nm (65~72 μm with 95% CI), and 112 μm at 1700 nm (repeat experiment, 88~136 μm with 95% CI).

Table 2.1: Summary of *in vivo* EAL measurements of the neocortex (NC) in three mice

Mouse	1700 nm	1550 nm	1500 nm	1450 nm	1700 nm (repeat)
Mouse1	405 μm	319 μm	278 μm	212 μm	410 μm
Mouse 2	350 μm	257 μm	220 μm	173 μm	348 μm
Mouse 3	370 μm	283 μm	241 μm	188 μm	370 μm

Similar measurements were repeated on different mice. The absolute EAL values varied somewhat among the different mice, which could be caused by variations in the surgical preparation or the individuality of the mice. Nonetheless, the relative trend of the EALs, i.e., l_e (1700 nm) > l_e (1550 nm) > l_e (1500 nm) > l_e (1450 nm), holds for all the mice. Three of them are listed in Table 2.1.

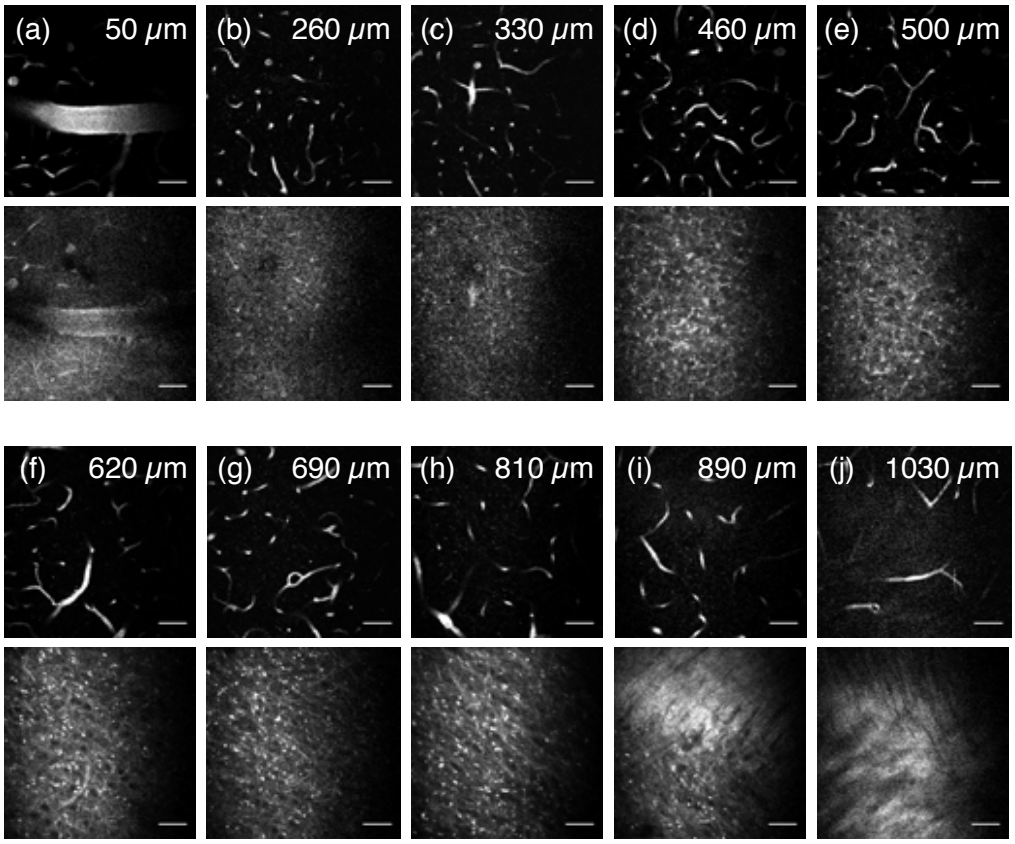

Figure 2.6: Three-photon fluorescence images of the brain vasculature (upper) and THG images (lower) using 1700 nm excitation. The depths are indicated in the images. All the images are shown with the same contrast setting with the brightest 1% pixels saturated. Scale bars, 50 μm.

2.5 *In vivo* EAL measurements at 1300 nm and 1450 nm excitation wavelengths

In order to verify the contribution of water absorption in tissue attenuation at 1450 nm, we performed an additional comparison experiment of EAL measurements at 1300 nm and 1450 nm excitation wavelengths. The laser spectra at 1300 nm and 1450 nm are shown in Fig. 2.2 a. The beam sizes at both excitation wavelengths were measured before the scanner (Figs. 2.7 a and 2.7 b), with

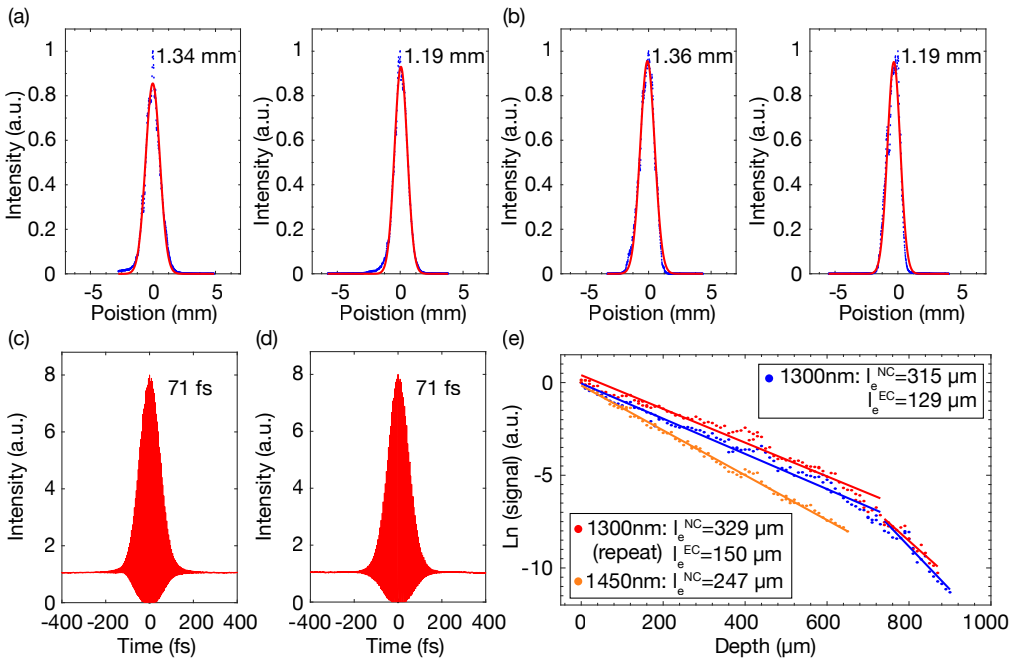

Figure 2.7: Beam size measurements at (a) 1300 nm and (b) 1450 nm. The blue dots are the measured data, and the red lines are Gaussian fits to the measurements. Measurements were taken along both the long axis (left) and the short axis (right). The FWHM is labeled in each figure. Measured second-order interferometric autocorrelations of the laser pulse operating at (c) 1300 nm and (d) 1450 nm. The FWHM of the pulse is indicated in the figure, assuming a deconvolution factor of 1.54 for sech^2-pulse. (e) Comparison of the fluorescence signal as a function of depth at 1300 nm, 1450 nm, and 1300 nm (repeat experiment). The dots are the measured data, and the lines are linear fits to the measurements. With the same maximum average power, imaging by 1300 nm excitation includes both the NC and EC, while imaging by 1450 nm is limited to the NC.

differences less than 1.5%. Second-order interferometric autocorrelations were performed after the objective lens at both wavelengths (Figs. 2.7 c and 2.7 d). The characterization method was the same as described in Section 2.3.

Because a mixture of 2- and 3-photon fluorescence from Texas Red is generated at 1300 nm excitation, we carried out this experiment separately using

Fluorescein. Three-photon imaging was performed on the same Fluorescein-labeled (dextran conjugate, 70kDa, Invitrogen) vasculature in an intact mouse brain *in vivo* in the order of 1300 nm, 1450 nm and 1300 nm (as a repeat). The results are presented in Fig. 2.7 e for the neocortex (NC, 0–740 µm) and the external capsule (EC, 740–900 µm). Measured EALs in the NC at different wavelengths with 95% CI are: 304~326 µm at 1300 nm, 243~251 µm at 1450 nm, 315~345 µm at 1300 nm (repeat experiment). The results at 1300 nm are consistent with previous studies [17, 28, 18] and are longer than that at 1450 nm. This comparison confirmed that water absorption is a key factor in the tissue attenuation at 1450 nm.

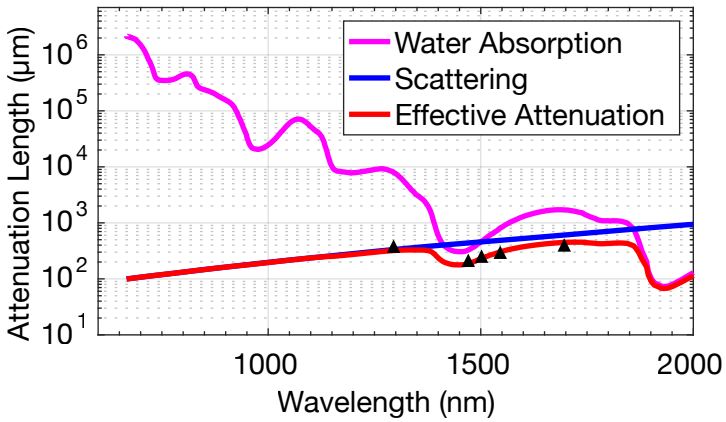

Figure 2.8: Experimental data (averaged from all the measured EALs for each wavelength, black triangles) is shown on the same plot together with the theoretical model, indicating the accuracy of the model at predicting the experimental measurements at these excitation wavelengths.

2.6 Discussion

The average values of the EAL measurements at different wavelengths are plotted together with the theoretical prediction (Fig. 2.8), indicating a close match

between the experiments and theory.

Measurements of the EAL can be influenced by the excitation beam characteristics. The excitation beam in the experiments with fluorescein is somewhat different (e.g., beam diameter) from that with Texas Red, making the comparison of the EALs at 1450 nm obtained by the imaging results based on Texas Red and Fluorescein difficult. Even more important, there can be variations in the tissue properties or animal preparations (e.g., cranial window implant) when different mice are used. For example, the EALs for three different mice varied by approximately 20% in our measurements at 1450 nm (Table 2.1), even with the same beam characteristics and the same fluorophore.

Our comparison results confirm that there is less light attenuation at 1300 nm and 1700 nm than at 1450 nm. Although 1300 nm and 1700 nm are optimum in the long wavelength window for *in vivo* deep tissue multiphoton imaging, the selection between 1300 nm and 1700 nm depends on the imaging applications. There is more tissue attenuation (shorter EAL) at 1300 nm excitation than at 1700 nm; however, 1300 nm has less tissue absorption, which allows for higher excitation power at the brain surface. It is therefore a trade-off between the coefficient (P_0) and the exponent (l_e) in Eq. 2.1, 1300 nm will be the wavelength of choice for relatively shallow regions and 1700 nm will perform better for pushing the absolute imaging depth, especially when the signal-to-background ratio (SBR) is also taken into account [11]. Estimations based on the measured EALs and the permissible average power show that 1300 nm is more appropriate for imaging in the neocortex, while 1700 nm is perhaps more advantageous for imaging subcortical regions. In addition, the choice of the excitation wavelength certainly depends on the fluorophores. For brain activity imaging, for

example, the robust, green fluorescent protein (GFP) based genetically encoded calcium indicators (GECIs) such as GCaMPs [3] dictate the use of 1300 nm excitation, while red fluorescent GECIs (RCaMPs, RGECOs [6]) would require the use of 1700 nm excitation.

2.7 Conclusion

We performed a systematic study of the impact of different excitation wavelengths on multiphoton imaging of the mouse brain *in vivo*. By comparing the effective attenuation lengths at 1300 nm, 1450 nm, 1500 nm, 1550 nm, and 1700 nm excitation wavelengths, we experimentally verified the water absorption contribution in brain tissue attenuation, especially at 1450 nm. Our results show that the theoretical estimations based on water absorption and tissue scattering are accurate in predicting tissue attenuation in the long wavelength window. This study can be used as an experimental guide of selecting excitation wavelengths for mouse brain imaging applications. For MPM of mouse brain *in vivo*, the spectral windows of 1300 nm and 1700 nm are optimum for deep imaging.

Bibliography

[1] M. Balu. Effect of excitation wavelength on penetration depth in nonlinear optical microscopy of turbid media. *J. Biomed. Opt.*, 14:010508, 2009.

[2] Kriti Charan, Bo Li, Mengran Wang, Charles P. Lin, and Chris Xu. Fiber-based tunable repetition rate source for deep tissue two-photon fluorescence microscopy. *Biomed. Opt. Express*, 9(5):2304–2311, May 2018.

[3] Tsai-Wen Chen, Trevor J. Wardill, Yi Sun, Stefan R. Pulver, Sabine L. Renninger, Amy Baohan, Eric R. Schreiter, Rex A. Kerr, Michael B. Orger, Vivek Jayaraman, Loren L. Looger, Karel Svoboda, and Douglas S. Kim. Ultrasensitive fluorescent proteins for imaging neuronal activity. *Nature*, 499(7458):295–300, July 2013.

[4] W. F. Cheong, S. A. Prahl, and A. J. Welch. A review of the optical properties of biological tissues. *IEEE Journal of Quantum Electronics*, 26(12):2166–2185, December 1990.

[5] Shau Poh Chong, Conrad W. Merkle, Dylan F. Cooke, Tingwei Zhang, Harsha Radhakrishnan, Leah Krubitzer, and Vivek J. Srinivasan. Noninvasive, *in vivo* imaging of subcortical mouse brain regions with 1.7 µm optical coherence tomography. *Opt. Lett.*, 40(21):4911–4914, November 2015.

[6] Hod Dana, Boaz Mohar, Yi Sun, Sujatha Narayan, Andrew Gordus, Jeremy P. Hasseman, Getahun Tsegaye, Graham T. Holt, Amy Hu, Deepika Walpita, Ronak Patel, John J. Macklin, Cornelia I. Bargmann, Misha B. Ahrens, Eric R. Schreiter, Vivek Jayaraman, Loren L. Looger, Karel Svoboda, and Douglas S. Kim. Sensitive red protein calcium indicators for imaging neural activity. *eLife*, 5:e12727, March 2016.

[7] W. Denk, J. H. Strickler, and W. W. Webb. Two-photon laser scanning fluorescence microscopy. 248(4951):73–76.

[8] Winfried Denk and Karel Svoboda. Photon upmanship: Why multiphoton imaging is more than a gimmick. 18(3):351–357.

[9] Andrew K. Dunn, Vincent P. Wallace, Mariah Coleno, Michael W. Berns, and Bruce J. Tromberg. Influence of optical properties on two-photon flu-

orescence imaging in turbid samples. *Appl. Opt.*, 39(7):1194–1201, March 2000.

[10] Moritz Friebel, Andre Roggan, Gerhard J. Müller, and Martina C. Meinke. Determination of optical properties of human blood in the spectral range 250 to 1100 nm using Monte Carlo simulations with hematocrit-dependent effective scattering phase functions. *J. Biomed. Opt*, 11(3):034021, May 2006.

[11] Fritjof Helmchen and Winfried Denk. Deep tissue two-photon microscopy. 2(12):932–940.

[12] Nicholas G. Horton, Ke Wang, Demirhan Kobat, Catharine G. Clark, Frank W. Wise, Chris B. Schaffer, and Chris Xu. *In vivo* three-photon microscopy of subcortical structures within an intact mouse brain. *Nat. Photonics*, 7(3):205–209, March 2013.

[13] Nicholas G. Horton and Chris Xu. Dispersion compensation in three-photon fluorescence microscopy at 1,700 nm. *Biomed. Opt. Express*, 6(4):1392–1397, April 2015.

[14] Steven L. Jacques. Optical properties of biological tissues: a review. *Phys. Med. Biol.*, 58(11):R37, 2013.

[15] David Kleinfeld and Winfried Denk. Two-photon imaging of neocortical microcirculation. In *Imaging Neurons: A Laboratory Manual*, pages 23.1–23.15. Cold Spring Harbor Laboratory Press, NY, 1999.

[16] David Kleinfeld, Partha P. Mitra, Fritjof Helmchen, and Winfried Denk. Fluctuations and stimulus-induced changes in blood flow observed in individual capillaries in layers 2 through 4 of rat neocortex. *Proc. Natl. Acad. Sci.*, 95(26):15741–15746, December 1998.

[17] Demirhan Kobat, Michael E. Durst, Nozomi Nishimura, Angela W. Wong, Chris B. Schaffer, and Chris Xu. Deep tissue multiphoton microscopy using longer wavelength excitation. *Opt. Express*, 17(16):13354–13364, August 2009.

[18] Demirhan Kobat, Nicholas G. Horton, and Chris Xu. *In vivo* two-photon microscopy to 1.6-mm depth in mouse cortex. *J. Biomed. Opt*, 16(10):106014, 2011.

[19] L. Kou. Refractive indices of water and ice in the 0.65- to 2.5-μm spectral range. *Appl. Opt.*, 32:3531–3540, 1993.

[20] Martin Oheim, Emmanuel Beaurepaire, Emmanuelle Chaigneau, Jerome Mertz, and Serge Charpak. Two-photon microscopy in brain tissue: parameters influencing the imaging depth. *Journal of Neuroscience Methods*, 111(1):29–37, October 2001.

[21] Dimitre G. Ouzounov, Tianyu Wang, Mengran Wang, Danielle D. Feng, Nicholas G. Horton, Jean C. Cruz-Hernndez, Yu-Ting Cheng, Jacob Reimer, Andreas S. Tolias, Nozomi Nishimura, and Chris Xu. In vivo three-photon imaging of activity of GCaMP6-labeled neurons deep in intact mouse brain. 14(4):388–390.

[22] Raquel F. Reinoso, Brian A. Telfer, and Malcolm Rowland. Tissue water content in rats measured by desiccation. *Journal of Pharmacological and Toxicological Methods*, 38(2):87–92, October 1997.

[23] Andre Roggan, Moritz Friebel, Klaus Doerschel, Andreas Hahn, and Gerhard J. Mueller. Optical properties of circulating human blood in the wavelength range 400–2500 nm. *J. Biomed. Opt*, 4(1):36–47, January 1999.

[24] Vivek J. Srinivasan, Harsha Radhakrishnan, James Y. Jiang, Scott Barry, and Alex E. Cable. Optical coherence microscopy for deep tissue imaging of the cerebral cortex with intrinsic contrast. *Opt. Express*, 20(3):2220–2239, January 2012.

[25] Patrick Theer, Mazahir T. Hasan, and Winfried Denk. Two-photon imaging to a depth of 1000 m in living brains by use of a ti:al$_2$o$_3$ regenerative amplifier. 28(12):1022–1024.

[26] K. Wang, N. G. Horton, K. Charan, and C. Xu. Advanced fiber soliton sources for nonlinear deep tissue imaging in biophotonics. 20(2):50–60.

[27] K. Wang, R. Liang, and P. Qiu. Fluorescence Signal Generation Optimization by Optimal Filling of the High Numerical Aperture Objective Lens for High-Order Deep-Tissue Multiphoton Fluorescence Microscopy. *IEEE Photonics Journal*, 7(6):1–8, December 2015.

[28] Tianyu Wang, Dimitre Ouzounov, Mengran Wang, and Chris Xu. Quantitative Comparison of Two-photon and Three-photon Activity Imaging of GCaMP6s-labeled Neurons *in vivo* in the Mouse Brain. In *Optics in the Life Sciences Congress (2017), paper BrM4B.4*, page BrM4B.4. Optical Society of America, April 2017.

[29] Chris Xu and Watt W. Webb. Multiphoton excitation of molecular fluorophores and nonlinear laser microscopy. In *Topics in Fluorescence Spectroscopy*, volume 5, pages 471–540. Springer, New York, 1997.

[30] Jinpin Ying, Feng Liu, and R. R. Alfano. Effect of scattering on nonlinear optical scanning microscopy imaging of highly scattering media. *Appl. Opt.*, 39(4):509–514, February 2000.

[31] Aikaterini Zoumi, Alvin Yeh, and Bruce J. Tromberg. Imaging cells and extracellular matrix *in vivo* by using second-harmonic generation and two-photon excited fluorescence. *Proc. Natl. Acad. Sci.*, 99(17):11014–11019, August 2002.

CHAPTER 3

IMPACT OF THE EMISSION WAVELENGTHS ON *IN VIVO* MULTIPHOTON IMAGING OF MOUSE BRAINS

3.1 Abstract

Tissue scattering and absorption impact the excitation and emission light in different ways for multiphoton imaging. The collected fluorescence includes both ballistic photons and scattered photons whereas multiphoton excited signal within the focal volume is mostly generated by ballistic photons. The impact of excitation wavelengths on multiphoton imaging has been extensively investigated before; however, experimental data is lacking to evaluate the impact of emission wavelengths on fluorescence attenuation in deep imaging. Here we perform three-photon imaging of mouse brain vasculature *in vivo* using green, red, and near-infrared emission fluorophores, and compare quantitatively the attenuation of the fluorescence signal in the mouse brain at the emission wavelengths of 520 nm, 615 nm and 711 nm. Our results show that the emission wavelengths do not significantly influence the fluorescence collection efficiency. For the green, red and near-infrared fluorophores investigated, the difference in fluorescence collection efficiency is less than a factor of 2 at imaging depths between 0.6 and 1 mm. The advantage of long wavelength dyes for multiphoton deep imaging is almost entirely due to the long excitation wavelengths. [1]

[1]This chapter has been published in Biomedical Optics Express: vol 10, issue 4, https://doi.org/10.1364/BOE.10.001905

3.2 Introduction

Multiphoton microscopy (MPM) utilizes nonlinear excitation to confine the fluorescence generation within the focal volume, which allows the use of efficient, large-area detectors for the fluorescence collection to improve the signal-to-noise ratio (SNR) for deep imaging in scattering biological tissue [8, 9, 28, 26, 14, 24, 21]. Light attenuation in biological tissues is a combined effect of absorption and scattering. Multiphoton excited signal within the focal volume is mostly generated by ballistic photons that are not scattered along the excitation path. However, because of the wide-field geometry for fluorescence collection in MPM, both ballistic and scattered fluorescence photons contribute to the image formation [6]. MPM relies on efficient fluorescence generation and collection for deep tissue penetration [10]. Understanding the transport of light in biological tissue is important in selecting the optimum excitation and emission wavelengths for MPM. Although the advantage of using long excitation wavelengths for MPM has been extensively explored [5, 17, 18, 31, 13, 3], the impact of emission wavelengths on deep imaging has not been systematically investigated before.

In this paper, we performed *in vivo* three-photon imaging in the same mouse brains using the same excitation wavelengths but with green, red, and near-infrared (NIR) emission dyes, and compared the signal attenuation in the tissue at these emission wavelengths. To ensure that all three fluorescent dyes are three-photon excited and there is no bleed-through of third harmonic generation (THG) signal into the fluorescence collection channels, we did two different sets of imaging on dye-labeled brain vasculature *in vivo*. One uses 1450 nm to excite fluorescein and Texas Red, and the other uses 1700 nm to excite Texas Red and

Alexa Fluor 647. The wavelength of the collected fluorescence is defined by the optical filters centered at 520 nm, 615 nm and 711 nm. Our experimental results show that the impact of the emission wavelengths on multiphoton deep imaging (within ~1 mm depth in the mouse brain) is small (less than a factor of 2) for the green, red and NIR fluorescent dyes investigated, and the advantage of long wavelength dyes for deep imaging is mostly contributed by the long excitation wavelengths.

3.3 Characterization of the three-photon imaging setup

The three-photon imaging setup is similar to that described previously [14, 24]. The excitation source was a wavelength-tunable optical parametric amplifier (OPA, Opera-F, Coherent) pumped by a Monaco amplifier (Coherent) operating at 330 kHz repetition rate. The excitation spectra at 1450 nm and 1700 nm were measured by an Optical Spectrum Analyzer (OSA, Thorlabs), shown in Fig. 3.1a.

The generated fluorescence was detected by photomultiplier tubes (PMTs) with GaAsP photocathodes (H7422-40, Hamamatsu Photonics). Three band-pass filters, 520/15 nm (Semrock, FF01-520/15-25), 615/20 nm (Semrock, FF02-615/20-25) and 711/25 nm (Semrock, FF01-711/25-25), were positioned in front of the PMTs to separate the fluorescence generated by fluorescein, Texas Red, and Alexa Fluor 647, respectively. The spectral response of the emission filters (provided by Semrock) is shown in Fig. 3.1b. The transmission at wavelengths >800 nm of these filters has no impact on the experiments due to the spectral response of the GaAsP PMT (cutoff <750 nm). The emission spectra for most fluorescent dyes are not symmetrical, and usually display long emission tails at

the long wavelengths; however, the bleed-through between fluorescence emission spectra does not alter the measurements since the wavelengths of the detected fluorescence were defined by the optical filters rather than the fluorescent dyes. Indeed, a single fluorescent dye would be preferred in this experiment if it could cover a broad emission spectrum from the green to the NIR.

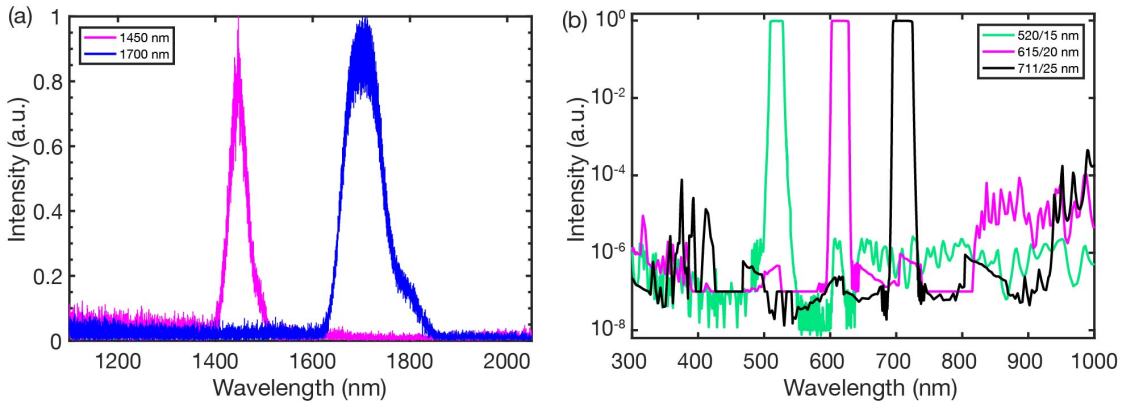

Figure 3.1: (a) Measured spectra of the laser source operating at 1450 nm and 1700 nm. (b) Transmission data for the three emission filters used for fluorescein (520/15 nm), Texas Red (615/20 nm) and Alexa Fluor 647 (711/25 nm).

Three-photon excitation was chosen to compare the impact of the emission wavelength in order to suppress the generation of out-of-focus fluorescence background, which would introduce uncertainties in the comparison [23, 29, 19]. To ensure that all three dyes are three-photon excited, we measured the dependence of the fluorescence on the excitation power for fluorescein and Texas Red with 1450 nm excitation, and Texas Red and Alexa Fluor 647 with 1700 nm excitation (Fig. 3.2). A low repetition rate of 330 kHz was used to increase three-photon excitation relative to two-photon excitation for the redder dyes in the comparisons since the ratio of three-photon to two-photon excited fluorescence is inversely proportional to the duty cycle of the laser pulse train

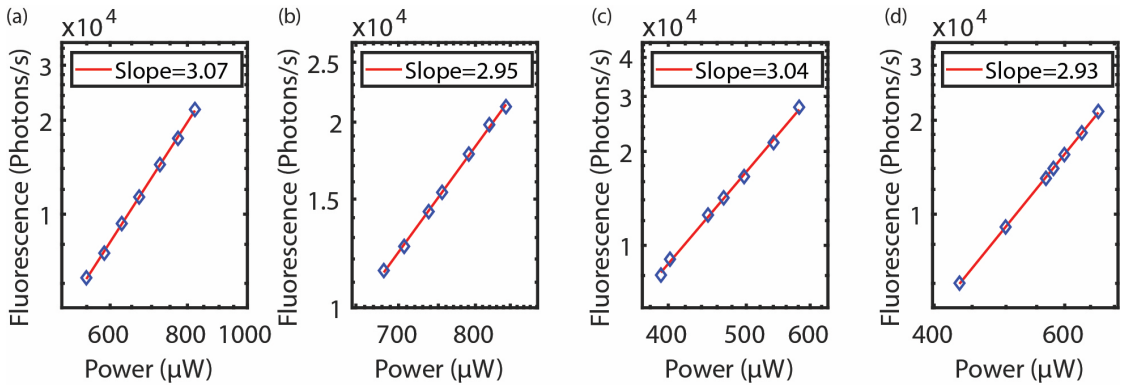

Figure 3.2: Dependence of three-photon-excited fluorescence on excitation power for (a) fluorescein excited at 1450 nm, (b) Texas Red excited at 1450 nm, (c) Texas Red excited at 1700 nm, and (d) Alexa Fluor 647 excited at 1700 nm. The blue diamonds are the measured data, and the red lines are linear fits to the experimental results. The slope is indicated in each figure.

[35]. The generated fluorescence was recorded by a photon counter (SR400, Stanford Research Systems). The slopes in the log-log power-dependence plots confirmed three-photon excitation for all the fluorescent dyes used here.

3.4 *In vivo* comparison of the impact of the emission wavelengths on deep imaging

To compare multiple fluorescent dyes excited by the same wavelengths without systematic bias, we did simultaneous imaging of fluorescein and Texas Red excited at 1450 nm, and Texas Red and Alexa Fluor 647 excited at 1700 nm. 5-mm craniotomies were performed on wild-type mice (C57BL/6J). A glass window was placed directly on the intact dura of each mouse for imaging. The mouse was anesthetized using isoflurane (3% in oxygen for induction and 1.5-2% for

surgery and imaging to maintain a breathing frequency of 1 Hz). Body temperature was kept at 37.5 °C with a feedback-controlled blanket (Harvard Apparatus), and eye ointment was applied.

The imaging conditions were kept the same for all the imaging sessions. The pulse energy at the focus is similar at each imaging depth (< 2nJ). As shown in Fig. 3.2, there is no fluorescence saturation at such pulse energy. Three-photon images were acquired in 20 μm depth increment from the brain surface. The images were taken at a frame rate of 0.24 Hz (512 x 512 pixels/frame) with a field-of-view (FOV) of 340 x 340 μm, and 10 frames were averaged at each depth to ensure high signal-to-noise ratio for all the images.

Since the fluorescence was acquired from the two fluorescent dyes at the same time by separating the signal into two detection channels using the emission bandpass filters, the imaging FOV and the imaging depth of each frame is identical for the two fluorophores. Example images are shown in Fig. 3.3.

For the comparison experiment of fluorescein and Texas Red excited at 1450 nm, dextran-conjugated fluorescein (70kDa, Invitrogen) and Texas Red (70kDa, Invitrogen) were injected retro-orbitally at the same time prior to imaging. Three-photon excited fluorescence was collected by the two detection channels simultaneously. The average value of the brightest 1% of pixels in the x-y image was selected at each depth as the fluorescence signal. To ensure that the results are not dependent on the selection criteria for the brightest pixels, we varied the selection criteria from 0.5% to 2%, and found that this variation did not affect the comparison results significantly.

The fluorescence signal at the depth z (F_z) was normalized to that at the

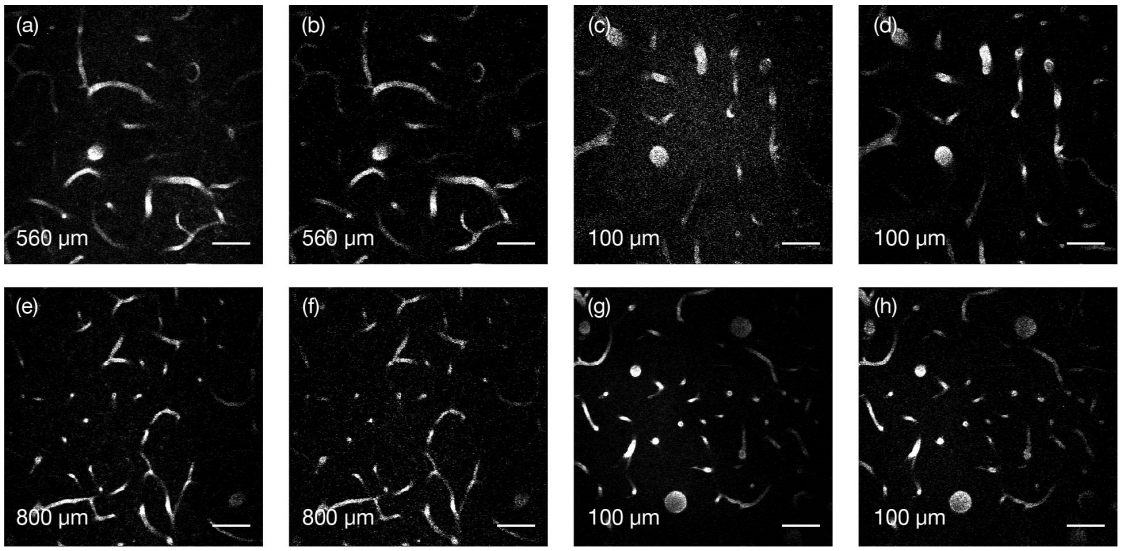

Figure 3.3: Three-photon fluorescence images of the brain vasculature labeled by fluorescein in (a) and (c), and by Texas Red in (b) and (d). Images in (a) to (d) were acquired by using 1450 nm excitation. Three-photon fluorescence images of the brain vasculature labeled by Texas Red in (e) and (g), and by Alexa Fluor 647 in (f) and (h). Images in (e) to (h) were acquired by using 1700 nm excitation. The depths are indicated in the images. All the images are shown with the same contrast setting. Scale bars, 50 µm.

surface (F_0). This is defined as the normalized fluorescence signal F_N, i.e., $F_N = F_z/F_0$. F_N is calculated at each depth and plotted in Fig. 3.4 a. We then calculated the ratio of the normalized Texas Red signal (F_{N-TR}) and the normalized fluorescein signal (F_{N-FL}) at each depth, i.e., F_{N-TR}/F_{N-FL}. The results are shown in Fig. 3.4 b.

Similarly, for the comparison of Texas Red and Alexa Fluor 647 excited at 1700 nm, dextran-conjugated Texas Red and Alexa Fluor 647 (10kDa, Invitrogen) were injected simultaneously into the same mouse and three-photon imaging was performed. We plotted the normalized fluorescence signal F_N as a function of depth in Fig. 3.5 a and the ratio of the normalized Alexa Fluor 647 signal

and Texas Red signal at each depth (i.e., $F_{N-AF647}/F_{N-TR}$) in Fig. 3.5 b.

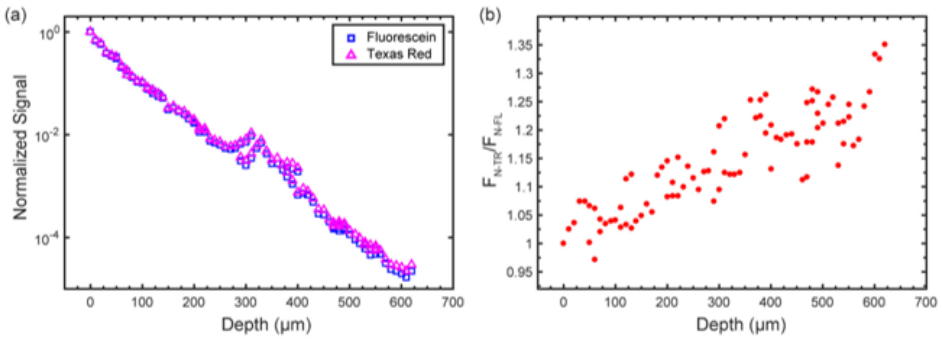

Figure 3.4: Simultaneous imaging of fluorescein and Texas Red using 1450 nm excitation. (a) Normalized fluorescence signal of fluorescein and Texas Red as a function of depth. (b) Ratio of the normalized Texas Red signal and the normalized fluorescein signal at each depth.

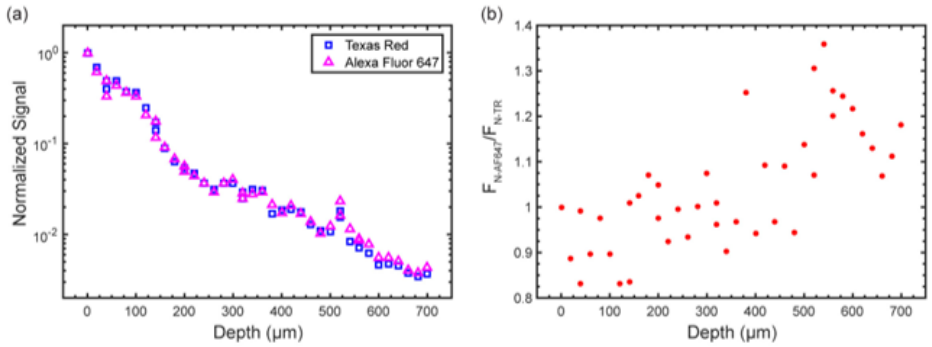

Figure 3.5: Simultaneous imaging of Texas Red and Alexa Fluor 647 using 1700 nm excitation. (a) Normalized fluorescence signal of Texas Red and Alexa Fluor 647 as a function of depth. (b) Ratio of the normalized Alexa Fluor 647 signal and the normalized Texas Red signal at each depth.

We repeated the simultaneous imaging experiments as described above in different mice with age from 8 weeks old to 6 months old (10 mice total for the comparison between fluorescein and Texas Red, and 7 mice total for the comparison between Texas Red and Alexa Fluor 647). For each mouse, we calculated the average ratio of the normalized Texas Red and fluorescein signal at every

100 µm depth interval, e.g., the ratios (F_{N-TR}/F_{N-FL}) obtained from the images between 0 and 100 µm are averaged, and the value is plotted at the 50 µm depth as the average ratio for the depth between 0 and 100 µm (Fig. 3.6a). Similar analysis was done for the Alexa Fluor 647 and Texas Red signal (Fig. 3.6b). We also averaged over all mice to get an average ratio at each depth interval. The results are summarized in Tables 3.1 and 3.2. Based on the experimental results, with the same signal at the brain surface, the Texas Red signal is about 1.34 times the fluorescein signal at 510-600 µm depth, and 1.43 times at 710-800 µm depth. The Alexa Fluor 647 signal is 1.14 times the Texas Red signal at 710-800 µm depth, and 1.14 times at 910-1000 µm depth.

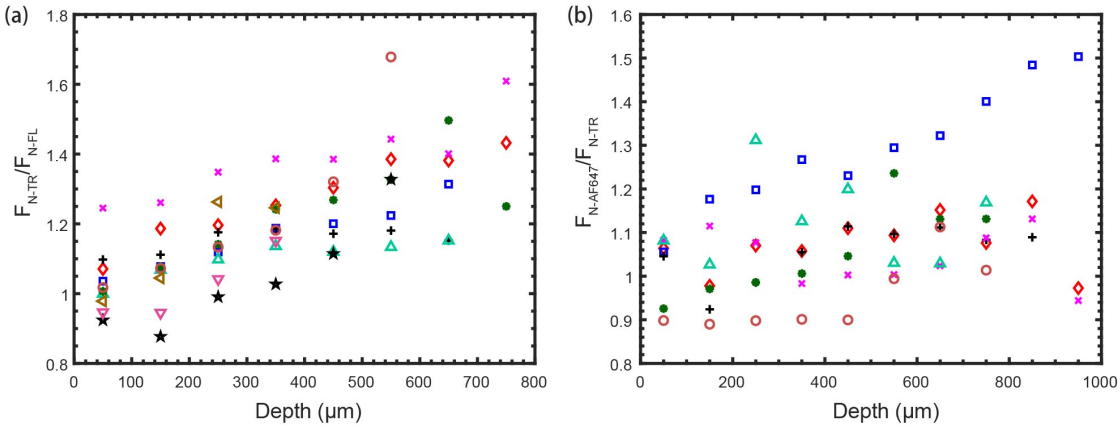

Figure 3.6: (a) Ratio of the normalized fluorescence of Texas Red and fluorescein averaged every 100 µm depth interval in 10 different mice. Each color/marker represents a different mouse. (b) Ratio of the normalized fluorescence of Alexa Fluor 647 and Texas Red averaged every 100 µm depth interval in 7 different mice. Each color/marker represents a different mouse.

Table 3.1: Ratio of the normalized fluorescence of Texas Red and fluorescein for all 10 mice at 100 µm depth interval.

Depth Range (µm)	Average Ratio	Minimum Ratio	Maximum Ratio
0-100	1.03	0.92	1.25
110-200	1.07	0.88	1.26
210-300	1.15	0.99	1.35
310-400	1.20	1.03	1.39
410-500	1.24	1.11	1.39
510-600	1.34	1.13	1.68
610-700	1.32	1.15	1.50
710-800	1.43	1.25	1.61

3.5 Discussion

Although the comparison experiments were performed by three-photon microscopy to reduce the out-of-focus background, the results also apply to two-photon microscopy. In order to put our results into proper context, we discuss several important considerations below, such as interaction between the dyes and the difference in the detection path between the two collection channels. We will then compare our experimental results with estimations obtained from the photon diffusion approximation.

3.5.1 Variations between imaging sessions

In order to calibrate the interaction between the dyes and investigate the difference in the detection path between the two collection channels, we must per-

Table 3.2: Ratio of the normalized fluorescence of Alexa Fluor 647 and Texas Red for all 7 mice at 100 µm depth interval.

Depth Range (µm)	Average Ratio	Minimum Ratio	Maximum Ratio
0-100	1.02	0.90	1.08
110-200	1.01	0.89	1.18
210-300	1.08	0.90	1.31
310-400	1.06	0.90	1.27
410-500	1.09	0.90	1.23
510-600	1.11	0.99	1.29
610-700	1.13	1.02	1.32
710-800	1.14	1.01	1.40
810-900	1.22	1.09	1.48
910-1000	1.14	0.94	1.50

form multiple imaging sessions on the same mouse. Therefore, we first calibrated the variations between different imaging sessions by performing three-photon imaging of the same dye in the same mouse brain repeatedly. The detection path including the detectors and the collection optics was kept the same for all the fluorescent dyes. For each dye, two imaging sessions were performed on the dye-labeled blood vessels and the normalized fluorescence signal is plotted as a function of depth for fluorescein excited at 1450 nm (Fig. 3.7 a), Texas Red excited at 1450 nm (Fig. 3.7 b), Texas Red excited at 1700 nm (Fig. 3.7 c), and Alexa Fluor 647 excited at 1700 nm (Fig. 3.7 d). We then calculated the difference between the two imaging sessions at each depth. After averaging over all depths, we find a difference of 32%, 35%, 29% and 15% for the data presented in Fig. 3.7 a, 3.7 b, 3.7 c and 3.7 d, respectively. The difference is mostly caused

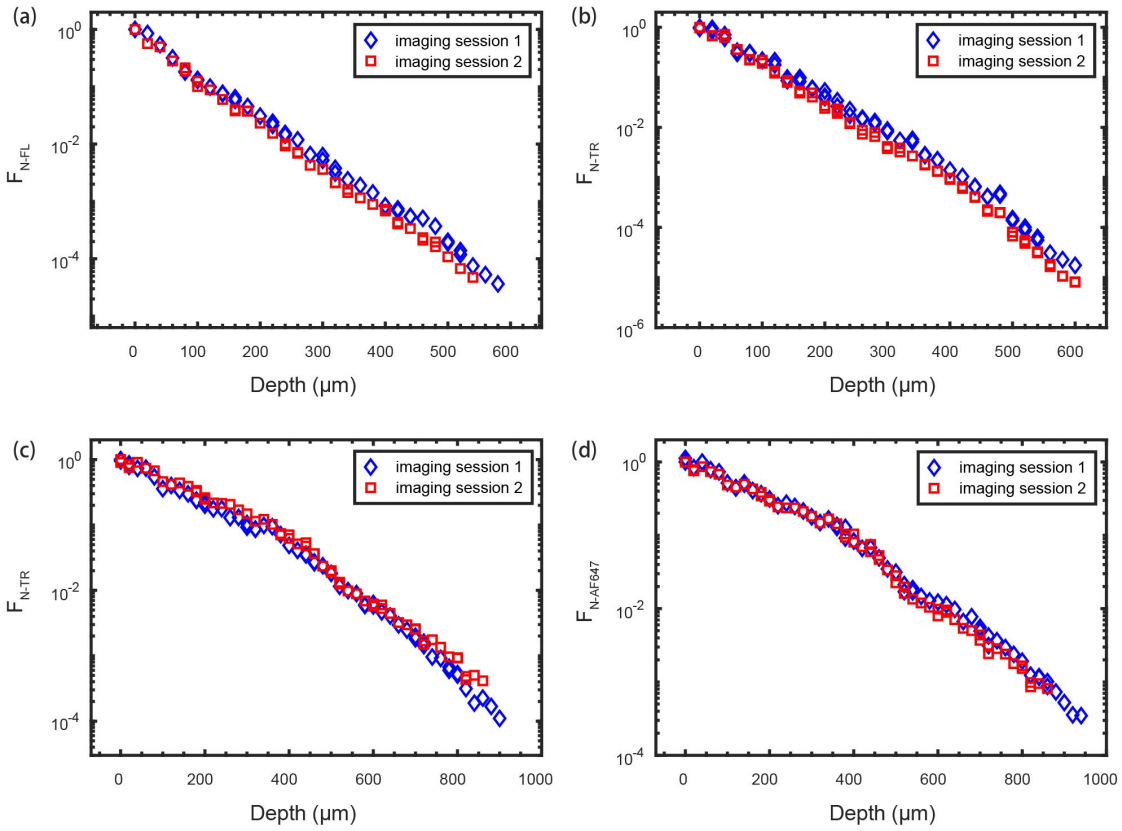

Figure 3.7: Variations between sequential imaging sessions. (a) Normalized fluorescein signal excited at 1450 nm as a function of depth. (b) Normalized Texas Red signal excited at 1450 nm as a function of depth. (c) Normalized Texas Red signal excited at 1700 nm as a function of depth. (d) Normalized Alexa Fluor 647 signal excited at 1700 nm as a function of depth.

by the depth difference between the two imaging sessions since it's difficult to match the imaging depth exactly in two sequential imaging sessions, especially with the 20 μm depth interval in our experiments. We note that such difficulties do not exist in our comparison experiments where simultaneous imaging of the two dyes was performed. These variations between the imaging sessions will be used as references in the following discussion.

3.5.2 Interaction between the dyes

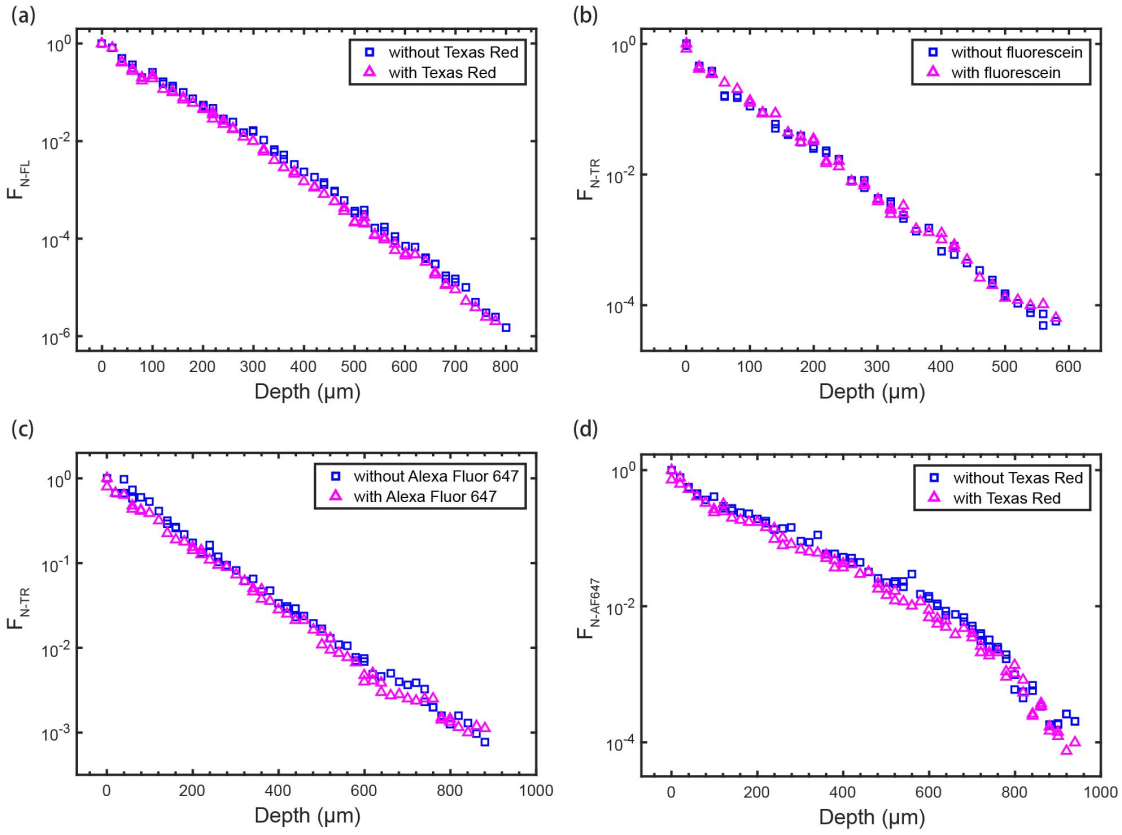

Figure 3.8: Investigation of the interaction between the dyes in simultaneous imaging. (a) Normalized fluorescein signal with and without the existence of Texas Red. The average difference for the fluorescein signal is 23% (b) Normalized Texas Red signal with and without the existence of fluorescein. The average difference for the Texas Red signal is 17%. (c) Normalized Texas Red signal with and without the existence of Alexa Fluor 647. The average difference for the Texas Red signal is 20% (d) Normalized Alexa Fluor 647 signal with and without the existence of Texas Red. The average difference for the Alexa Fluor 647 signal is 24%.

Interaction between the dyes could be a concern, e.g., the emission of the bluer dye may potentially excite the redder dye. Therefore, we compared the imaging results with and without the presence of the second dye. To test whether the presence of Texas Red alters the signal attenuation of fluorescein

in the mouse brain, we first imaged fluorescein. Then Texas Red was injected into the mouse, and fluorescein was imaged again with the presence of Texas Red. The results are shown in Fig. 3.8 a. We performed similar experiments for the dyes in all possible combinations, and the results are summarized in Fig. 3.8. With the same signal level at the brain surface (normalized to 1), the average difference for the fluorescein signal with and without the presence of Texas Red is 23% (Fig. 3.8a), which is comparable to the variations between imaging sessions discussed in Section 3.5.1. Similar results are obtained for all the other dye combinations (Fig. 3.8), which confirmed that the presence of a second dye in the simultaneous imaging experiments has negligible impact on the imaging of the first dye.

3.5.3 Difference between the collection channels

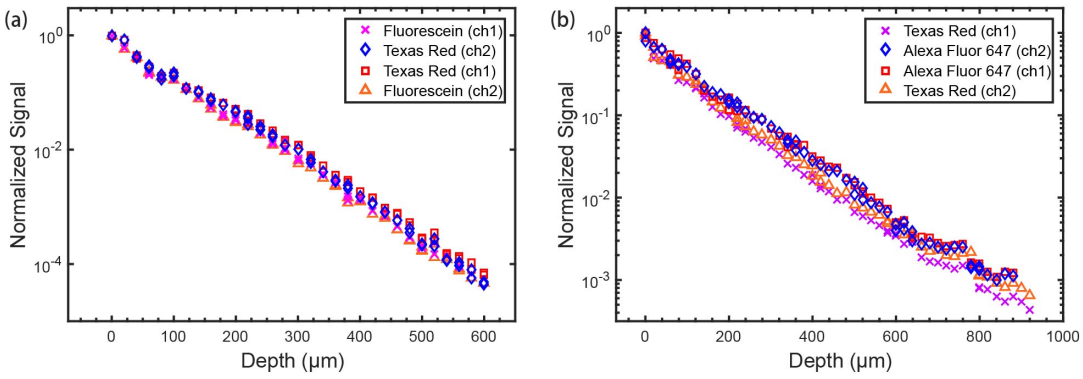

Figure 3.9: Simultaneous imaging before and after channel swapping. (a) Normalized fluorescence signal of fluorescein and Texas Red as a function of depth for the two simultaneous imaging sessions before and after channel swapping. (b) Normalized fluorescence signal of Texas Red and Alexa Fluor 647 as a function of depth for the two simultaneous imaging sessions before and after channel swapping.

To verify that the difference in the collection path for the two channels in simultaneous imaging does not alter the results, we performed experiments by swapping the collection channels. For the comparison of fluorescein and Texas Red excited at 1450 nm, we first performed simultaneous three-photon imaging with channel 1 (ch 1) for fluorescein and channel 2 (ch 2) for Texas Red. We then repeated the imaging experiment by swapping the two channels, with channel 1 for Texas Red and channel 2 for fluorescein. The results are shown in Fig. 3.9 a. We compared the signal level before and after channel swapping, and found that there is an average difference of 9% and 15% for fluorescein and Texas Red, respectively, which is within the variations between imaging sessions. We also performed the same channel-swapping experiments for the comparison of Texas Red and Alexa Fluor 647 excited at 1700 nm (Fig. 3.9 b). The average signal difference before and after channel swapping is 21% for Texas Red and 8% for Alexa Fluor 647, which is again within the variations between imaging sessions. This set of experiments proved that the slight difference in the signal collection path between channel 1 and channel 2 does not introduce significant systematic bias in the comparison results.

3.5.4 Diffusion theory and Beer's law predictions

Diffusion theory can be used to estimate the light transport in biological tissues based on the tissue optical properties, such as absorption coefficient (μ_a), scattering coefficient (μ_s), and anisotropy factor (g).

For the mouse brains *in vivo*, blood absorption dominates the absorbance at the wavelengths investigated in this paper. Oxy-hemoglobin (HbO_2) and

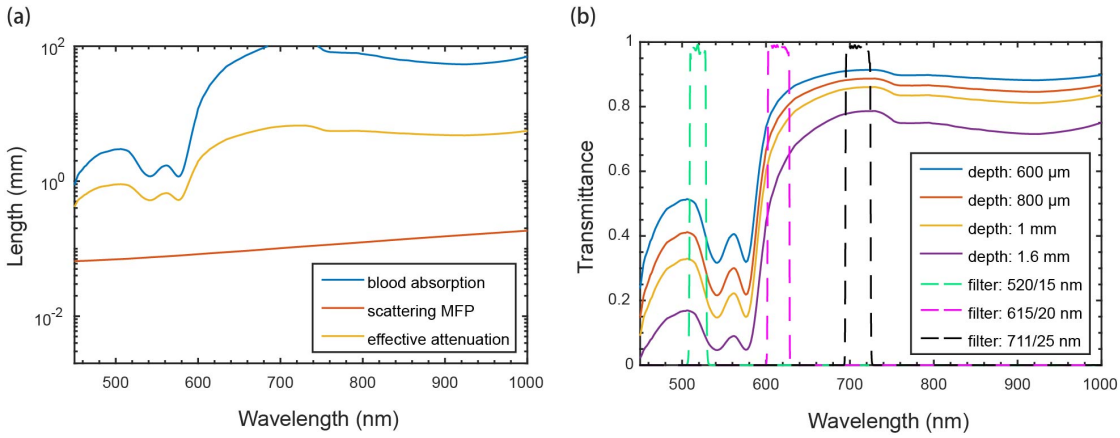

Figure 3.10: Diffusion theory of emission light transport at different wavelengths for mouse brain in vivo. (a) Effective attenuation length of emission light calculated by the modified solution of diffusion theory, Eq. 2. (b) The collected fluorescence at the brain surface from a depth of 600 μm, 800 μm, 1 mm, and 1.6 mm based on the calculated effective attenuation length. The transmission data for the three emission filters used in imaging are also shown.

deoxy-hemoglobin (HbR) are the main optical absorbers in biological tissue in the visible spectral range [1]. Based on the reported values for oxygen saturation (sO_2) measurements, we assume that all the hemoglobin in the arteries are HbO_2 while the veins contain 75% HbO_2 and 25% HbR [32, 40, 39, 15, 11, 36, 33, 27, 37]. Thus, the absorption coefficient for the veins μvein and the arteries μ_{artery} can be expressed based on the relative concentration of oxy- and deoxy-hemoglobin: $\mu_{vein} = 0.75\ \mu_{HbO_2} + 0.25\mu_{HbR}$ and $\mu_{artery} = \mu_{HbO_2}$. Assume that there are 70% veins and 30% arteries in the mouse brain vasculature *in vivo* [16], the effective blood absorption coefficient μ_b is $\mu_b = 0.7\ \mu_{vein} + 0.3\mu_{artery}$.

Calculated from the 2-dimensional three-photon images we took, we found that there is an average of 5% (standard deviation 0.5%, from all 17 mice) blood volume in the imaged brain regions. However, this likely over-estimates the blood volume concentration because the axial resolution (approximately 4 μm

in our experiments [14]) is comparable to the size of the capillary vessels. Nevertheless, the small standard deviation indicates that the blood content for the mice we imaged is overall very consistent. On the other hand, previous measurements using high-resolution 3-dimensional re-construction showed that the blood volume concentration in the same mouse brain region is approximately 3% [34]. Using 3% as the blood volume concentration, the effective absorption coefficient (μ_a) can be estimated as: μ_a =0.03μ_b =0.03 x (0.825μ_{HbO_2} +0.175μ_{HbR}). The effective absorption length ($1/\mu_a$) is plotted in Fig. 3.10 a.

To estimate the scattering coefficient μs and the anisotropy factor g in the brain tissue, Mie scattering is used for a tissue-like colloidal solution containing 1-μm diameter beads at a concentration of $5.4x10^9$ beads/mL [7, 22, 30]. The scattering mean free path (MFP, l_s=$1/\mu_s$) is also plotted in Fig. 3.10 a.

Radiative transfer equation (RTE) can be used to model the photon migration in biological tissues. The diffusion approximation of RTE provides an analytical solution for cases where the absorption of the tissue is negligible compared to the scattering, and the light sources and detectors are far apart so that the photon trajectories can be treated as diffuse. The transport MFP, defined by $l_t = l_s/(1-g)$, describes the average distance over which a photon loses the memory of its initial direction. When the imaging depth (z) is much larger than the transport MFP of the emission photons ($z \leq l_t$), the emitted photons are in the diffusive regime, and the diffusion approximation is well suited to model their propagation [12, 20].

Solving the diffusion equation for the simple case of a time-independent point source in an infinite homogeneous medium, we can find the effective attenuation coefficient [2]:

$$\mu_{eff} = \sqrt{(3\mu_a[\mu_a + \mu_s(1-g)])} \tag{3.1}$$

This simple model needs to be modified in order to apply to the visible spectral regions *in vivo* where tissue absorption is not negligible. A modified solution of the diffusion equation with a weighted dependence on the absorption coefficient can be written as:

$$\mu_{eff} = \sqrt{(3\mu_a[\alpha\mu_a + \mu_s(1-g)])} \tag{3.2}$$

Here we use $\alpha = 0.5$ based on the calculations and experimental validations for a highly anisotropic scattering medium (g<0.8) [4, 25, 38]. Using Eq. 3.1, we plot the effective attenuation length (l_e=$1/\mu_{eff}$) in the mouse brain *in vivo* in Fig. 3.10 a.

The ratio of the normalized fluorescence signal from the same point source at depth z for two different emission wavelengths λ_1 and λ_2 is:

$$Ratio(z) = \frac{e^{-\frac{z}{l_{e\lambda_2}}}}{e^{-\frac{z}{l_{e\lambda_1}}}} \tag{3.3}$$

We calculated the transmission spectrum (Fig. 3.10 b) of a point emitter at depths of 600 µm, 800 µm, 1 mm, and 1.6 mm in the mouse brain using Eq. 3.3. We find that the ratio for the emission between 615 nm and 520 nm is 1.72 at z=600 µm and 2.07 at z=800 µm. The ratio for the emission between 711 nm and 615 nm is 1.16 at z=800 µm and 1.21 at z=1 mm.

As seen from Fig. 3.10, absorption by the brain tissue is relatively small at imaging depth < 1 mm for the green, red and NIR wavelength investigated. This

is the main reason that the impact of the emission wavelength on multiphoton imaging is small. On the other hand, as we push the imaging depth further, the impact of the emission wavelength will become more important. For example, the difference between red and green emissions at 1.6 mm is ~ 4.27.

The estimation using the diffusion approximation matches well with the experimental data for the red and NIR fluorophores. On the other hand, our experimental results showed that the difference in signal collection between green and red fluorescence is less than a factor of 1.5, while the diffusion theory predicts the difference to be close to a factor of 2. The small discrepancies between experimental results and diffusion theory could be caused by several factors such as the difference in blood concentration. Table 3.3 summarizes our experimental data and the estimations using Eq. 3.2 at various blood volume concentrations. As the blood concentration is lowered, the experimental results and the estimations get closer.

Table 3.3: Summary of the experimental results and theoretical calculations with different blood concentrations.

Data	ratio 615/520 at 600 µm	ratio 615/520 at 800 µm	ratio 711/615 at 800 µm	ratio 711/615 at 1 mm
Experimental results	1.34	1.43	1.14	1.14
Estimation with 2% blood	1.53	1.77	1.13	1.16
Estimation with 2.5% blood	1.63	1.92	1.15	1.19
Estimation with 3% blood	1.72	2.07	1.16	1.21
Estimation with 3.5% blood	1.82	2.22	1.18	1.22
Estimation with 4% blood	1.92	2.38	1.19	1.24

In this paper, we used narrow bandwidth filters to define the wavelength

detected precisely. In practical fluorescence imaging, where broader bandwidth filters or even long-pass filters are usually used to improve the fluorescence collection efficiency. In order to evaluate the emission transmission efficiency under the practical fluorescence collection settings, we performed calculations by combining the fluorescence emission spectra (provided by Thermo Fisher Scientific) and the calculated tissue transmission spectrum in Fig. 3.10 b with commonly used broad bandwidth (40 nm bandwidth) filters centered at 530 nm for fluorescein, 610 nm for Texas Red, and 660 nm for Alexa Fluor 647. We further performed calculations with no filters at all and allowed the entire emission spectrum to be detected. The calculated results are summarized in Table 3.4. Compared to the results in Table 3.3, the differences caused by the filter settings are small (< 10%).

Table 3.4: Summary of the fluorescence transmission ratios for fluorescein (FL), Texas Red (TR) and Alexa Fluor 647 (AF647) with 40-nm bandwidth filters and with no filters at all (full emission spectrum). The blood volume concentration is assumed to be 3%.

Data	ratio TR/FL at 600 µm	ratio TR/FL at 800 µm	ratio AF647/TR at 800 µm	ratio AF647/TR at 1 mm
Filters with 40 nm bandwidth	1.83	2.25	1.02	1.06
Full spectrum	1.85	2.25	1.13	1.16

Beer's law is a more straightforward and accessible method compared to the diffusion theory in predicting the absorbance of photons especially for the high absorption regimes such as for the green fluorophores. Here we used Beer's law to calculate the transmission spectra through various thickness of the brain tissue, assuming a uniform concentration of hemoglobin. To be consistent with

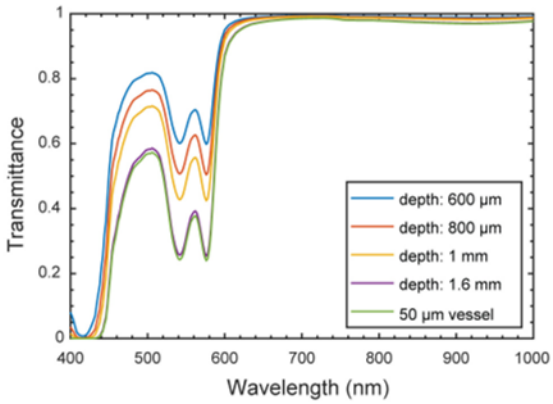

Figure 3.11: Beer's law calculations of emission light transmission from a depth of 600 μm, 800 μm, 1 mm, and 1.6 mm as well as the emission light transmission through a 50-μm-diameter vessel.

the diffusion approximation, we used the same oxygen saturation value (82.5%) of the whole blood and the blood concentration (3%). Fig. 3.11 shows the transmission spectra at depths of 600 μm, 800 μm, 1 mm, and 1.6 mm in the mouse brain. The ratio for the emission between 615 nm and 520 nm is 1.25 at z=600 μm and 1.35 at z=800 μm. The ratio for the emission between 711 nm and 615 nm is 1.02 at z=800 μm and 1.03 at z=1 mm. Fig. 3.11 better predicts the shorter wavelength transmission ratio but underestimates the measurement results in the longer wavelength regime. On the other hand, Fig. 3.11 significantly overestimates the absolute transmission through the brain tissue at all wavelengths by not accounting for tissue scattering (i.e., the zig-zagging photon path).

By comparing the fluorescence signals across the entire FOV, our results represent the average signal attenuation at various depths. Because of the heterogenous nature of the brain tissue, however, locally large variations of attenuation could occur. For example, fluorescence emitted directly below a large diameter blood vessel could have a much stronger dependence on the emission wave-

length than those measured in this paper. To illustrate this argument, we show the transmission of fluorescence through a 50-μm-diameter vessel using Beer's law in Fig. 3.11. The ratio for the transmission between 615 nm and 520 nm is 1.87, which is larger than what we measured at 0.8 mm deep. A possible example of this phenomenon was observed experimentally in a previous publication (Fig. 5 of ref. [17]).

3.6 Conclusion

We systematically compared the emission attenuation of green, red and near-infrared fluorophores by three-photon imaging of the mouse brain *in vivo*. Based on the experimental results, we found that, within 1 mm depth in the mouse brain, the attenuation of the green fluorescence (~ 520 nm) is slightly higher than the red fluorescence (~ 615 nm) fluorescence, with the difference being 1.34-1.43 times for imaging depths of 0.6 to 0.8 mm. The attenuation of the near-infrared fluorescence (~711 nm) is comparable (within ~ 14%) to the red fluorescence. The reason for the small impact of emission wavelength on fluorescence attenuation with depth is that the collected fluorescence is contributed by both scattered and ballistic photons, whereas the signal generation within the focal volume is mainly contributed by ballistic photons. Our results show that the advantage of long wavelength dyes for multiphoton deep imaging is mainly due to the long excitation wavelengths, and the impact of emission wavelengths on multiphoton imaging depth is negligible for imaging within the superficial 1 mm of the mouse brain.

Bibliography

[1] Optical spectra.

[2] Radiative transfer equation and diffusion theory. In *Biomedical Optics*, pages 83–118. Wiley-Blackwell.

[3] Volker Andresen, Stephanie Alexander, Wolfgang-Moritz Heupel, Markus Hirschberg, Robert M. Hoffman, and Peter Friedl. Infrared multiphoton microscopy: subcellular-resolved deep tissue imaging. 20(1):54–62.

[4] Raphael Aronson and Noel Corngold. Photon diffusion coefficient in an absorbing medium. 16(5):1066–1071.

[5] M. Balu. Effect of excitation wavelength on penetration depth in nonlinear optical microscopy of turbid media. *J. Biomed. Opt.*, 14:010508, 2009.

[6] Emmanuel Beaurepaire and Jerome Mertz. Epifluorescence collection in two-photon microscopy. 41(25):5376–5382.

[7] W. F. Cheong, S. A. Prahl, and A. J. Welch. A review of the optical properties of biological tissues. *IEEE Journal of Quantum Electronics*, 26(12):2166–2185, December 1990.

[8] W. Denk, J. H. Strickler, and W. W. Webb. Two-photon laser scanning fluorescence microscopy. 248(4951):73–76.

[9] Winfried Denk and Karel Svoboda. Photon upmanship: Why multiphoton imaging is more than a gimmick. 18(3):351–357.

[10] Andrew K. Dunn, Vincent P. Wallace, Mariah Coleno, Michael W. Berns, and Bruce J. Tromberg. Influence of optical properties on two-photon flu-

orescence imaging in turbid samples. *Appl. Opt.*, 39(7):1194–1201, March 2000.

[11] Zijian Guo, Song Hu, and Lihong V. Wang. Calibration-free absolute quantification of optical absorption coefficients using acoustic spectra in 3d photoacoustic microscopy of biological tissue. 35(12):2067–2069.

[12] Fritjof Helmchen and Winfried Denk. Deep tissue two-photon microscopy. 2(12):932–940.

[13] Josephine Herz, Volker Siffrin, Anja E. Hauser, Alexander U. Brandt, Tina Leuenberger, Helena Radbruch, Frauke Zipp, and Raluca A. Niesner. Expanding two-photon intravital microscopy to the infrared by means of optical parametric oscillator. 98(4):715–723.

[14] Nicholas G. Horton, Ke Wang, Demirhan Kobat, Catharine G. Clark, Frank W. Wise, Chris B. Schaffer, and Chris Xu. *In vivo* three-photon microscopy of subcortical structures within an intact mouse brain. *Nat. Photonics*, 7(3):205–209, March 2013.

[15] Song Hu, Konstantin I. Maslov, Vassiliy Tsytsarev, and Lihong V. Wang. Functional transcranial brain imaging by optical-resolution photoacoustic microscopy. 14(4):040503.

[16] Hyejin Jeong, Seongtae Jeong, Hoi J. Lim, JongUn Lee, and Kyung Y. Yoo. Cerebral oxygen saturation measured by near-infrared spectroscopy and jugular venous bulb oxygen saturation during arthroscopic shoulder surgery in beach chair position under sevoflurane-nitrous oxide or propofol-remifentanil anesthesia. 116(5):1047–1056.

[17] Demirhan Kobat, Michael E. Durst, Nozomi Nishimura, Angela W. Wong, Chris B. Schaffer, and Chris Xu. Deep tissue multiphoton microscopy using longer wavelength excitation. *Opt. Express*, 17(16):13354–13364, August 2009.

[18] Demirhan Kobat, Nicholas G. Horton, and Chris Xu. *In vivo* two-photon microscopy to 1.6-mm depth in mouse cortex. *J. Biomed. Opt*, 16(10):106014, 2011.

[19] A. Leray, C. Odin, E. Huguet, F. Amblard, and Y. Le Grand. Spatially distributed two-photon excitation fluorescence in scattering media: Experiments and time-resolved monte carlo simulations. 272(1):269–278.

[20] A. Leray, C. Odin, and Y. Le Grand. Out-of-focus fluorescence collection in two-photon microscopy of scattering media. 281(24):6139–6144.

[21] Barry R. Masters and Peter So. *Handbook of Biomedical Nonlinear Optical Microscopy*. Oxford University Press. Google-Books-ID: 4mki1ThMgGYC.

[22] Christian Mtzler. MATLAB functions for mie scattering and absorption.

[23] Martin Oheim, Emmanuel Beaurepaire, Emmanuelle Chaigneau, Jerome Mertz, and Serge Charpak. Two-photon microscopy in brain tissue: parameters influencing the imaging depth. *Journal of Neuroscience Methods*, 111(1):29–37, October 2001.

[24] Dimitre G. Ouzounov, Tianyu Wang, Mengran Wang, Danielle D. Feng, Nicholas G. Horton, Jean C. Cruz-Hernndez, Yu-Ting Cheng, Jacob Reimer, Andreas S. Tolias, Nozomi Nishimura, and Chris Xu. In vivo three-photon imaging of activity of GCaMP6-labeled neurons deep in intact mouse brain. 14(4):388–390.

[25] Jorge Ripoll, Doreen Yessayan, Giannis Zacharakis, and Vasilis Ntziachristos. Experimental determination of photon propagation in highly absorbing and scattering media. 22(3):546–551.

[26] Peter T. C. So, Chen Y. Dong, Barry R. Masters, and Keith M. Berland. Two-photon excitation fluorescence microscopy. 2(1):399–429.

[27] Wei Song, Qing Wei, Wenzhong Liu, Tan Liu, Ji Yi, Nader Sheibani, Amani A. Fawzi, Robert A. Linsenmeier, Shuliang Jiao, and Hao F. Zhang. A combined method to quantify the retinal metabolic rate of oxygen using photoacoustic ophthalmoscopy and optical coherence tomography. 4:6525.

[28] Karel Svoboda and Ryohei Yasuda. Principles of two-photon excitation microscopy and its applications to neuroscience. 50(6):823–839.

[29] Patrick Theer and Winfried Denk. On the fundamental imaging-depth limit in two-photon microscopy. 23(12):3139–3149.

[30] Patrick Theer, Mazahir T. Hasan, and Winfried Denk. Two-photon imaging to a depth of 1000 m in living brains by use of a ti:al$_2$o$_3$ regenerative amplifier. 28(12):1022–1024.

[31] Mengran Wang, Chunyan Wu, David Sinefeld, Bo Li, Fei Xia, and Chris Xu. Comparing the effective attenuation lengths for long wavelength in vivo imaging of the mouse brain. 9(8):3534–3543.

[32] Xueding Wang, Xueyi Xie, Geng Ku, Lihong V. Wang, and George Stoica. Noninvasive imaging of hemoglobin concentration and oxygenation in the rat brain using high-resolution photoacoustic tomography. 11(2):024015.

[33] Jun Xia, Amos Danielli, Yan Liu, Lidai Wang, Konstantin Maslov, and Lihong V. Wang. Calibration-free quantification of absolute oxygen saturation based on the dynamics of photoacoustic signals. 38(15):2800–2803.

[34] Benyi Xiong, Anan Li, Yang Lou, Shangbin Chen, Ben Long, Jie Peng, Zhongqin Yang, Tonghui Xu, Xiaoquan Yang, Xiangning Li, Tao Jiang, Qingming Luo, and Hui Gong. Precise cerebral vascular atlas in stereotaxic coordinates of whole mouse brain. 11.

[35] Chris Xu and Watt W. Webb. Multiphoton excitation of molecular fluorophores and nonlinear laser microscopy. In *Topics in Fluorescence Spectroscopy*, volume 5, pages 471–540. Springer, New York, 1997.

[36] Junjie Yao, Konstantin I. Maslov, Yu Zhang, Younan Xia, and Lihong V. Wang. Label-free oxygen-metabolic photoacoustic microscopy *in vivo*. 16(7):076003.

[37] Junjie Yao, Lidai Wang, Joon-Mo Yang, Konstantin I. Maslov, Terence T. W. Wong, Lei Li, Chih-Hsien Huang, Jun Zou, and Lihong V. Wang. High-speed label-free functional photoacoustic microscopy of mouse brain in action. 12(5):407–410.

[38] Giannis Zacharakis, Hirokazu Kambara, Helen Shih, Jorge Ripoll, Jan Grimm, Yoshinaga Saeki, Ralph Weissleder, and Vasilis Ntziachristos. Volumetric tomography of fluorescent proteins through small animals in vivo. 102(51):18252–18257.

[39] Hao F. Zhang, Konstantin Maslov, Mathangi Sivaramakrishnan, Gheorghe Stoica, and Lihong V. Wang. Imaging of hemoglobin oxygen satu-

ration variations in single vessels in vivo using photoacoustic microscopy. 90(5):053901.

[40] Hao F. Zhang, Konstantin Maslov, George Stoica, and Lihong V. Wang. Functional photoacoustic microscopy for high-resolution and noninvasive *in vivo* imaging. 24(7):848–851.

CHAPTER 4

DEEP THREE-PHOTON IMAGING OF THE SUBVENTRICULAR ZONE STEM CELL NICHE IN LIVE MICE

4.1 Abstract

The subventricular zone (SVZ) is a heterogeneous neurogenic stem cell niche so deep in the brain that non-invasive live imaging has been a major challenge. SVZ cell subtypes have been extensively described in histological or *ex vivo* slice preparations but how these techniques affect cell morphology is unknown. We developed and adapted three-photon microscopy (3PM) for non-invasive deep brain imaging in live animals. However, its utility in imaging the SVZ niche was unknown. Here we show 3PM visualisation of typical neural stem cells (NSC), intermediate progenitors and neuroblasts in both postnatal and adult SVZ. Imaging included the whole SVZ and extended to a maximum depth of 1.5 mm from the dura matter. 3PM detected the fine processes of radial glia-like NSC and their physical interaction with niche vasculature with subcellular resolution. Importantly we did not observe any overt signs of inflammation due to the microscopy. 3PM thus provides the first non-damaging opportunity to image the SVZ, can distinguish cell morphologies in live animals and has the potential of dynamically imaging stem cell lineage progression in situ at various ages.

4.2 Introduction

The subventricular zone (SVZ) is a specialised niche lining the lateral ventricles that contains neural stem cells (NSC). It has been extensively characterized at the cellular level and is a robust system for neurodevelopmental mechanism discovery [16, 23, 39]. The SVZ is important for perinatal brain development, as one of the main sources of forebrain glia [22] and olfactory bulb (OB) neurons [1]. This stem cell niche can be stimulated to increase neurogenesis, which limits neuronal injury and neurodegeneration [44]. On the dark side, SVZ stem cells can be tumorigenic, for example transformation by the IDH1R132H mutation in SVZ is accompanied by glioma [5]. Importantly there is firm evidence that the human SVZ is neurogenic during early postnatal life and, in addition to the OB [35], may supply interneurons to the cerebral cortex [31]. Proliferation in the SVZ has been detected histologically [13]. With ^{14}C birth-dating method, one study suggested newborn neurons migrate into the adjacent caudate nucleus [14].

SVZ neurogenesis consists of multiple dynamic cell functions, including neural stem cell (NSC) activation, transit amplifying progenitor (TAP) cell proliferation, neuroblast migration and differentiation. However the SVZ has not been visualised in intact live animals, with the greatest hurdles being its deep location. The highly heterogeneous brain tissue also causes unacceptable photon scattering of short two-photon wavelengths. Nevertheless, two-photon microscopy (2PM) imaging of *ex vivo* slice cultures has been used to analyse neuroblast migration in the SVZ and rostral migratory stream (RMS) [29, 17, 25]. We previously showed that rostral neuroblast migration was interspersed with local exploratory movements, periods of immobility, dorsoventral and caudal

migration. However, differences in the culture media and *in vivo* extracellular fluid can affect NSC proliferation and fate choice and it is unclear how accurately slice culture reflects other cell dynamics *in vivo* [37]

Intravital 2PM is restricted to approximately the surface 500 microns of tissue but the SVZ and SGZ are more than twice as deep. Therefore others have used cortical windows and 2PM in the brain of live mice to image the SGZ stem cell niche [33, 32]. One study generated excellent data over two months and followed individual clones of cells as they expanded and differentiated [32]. Whereas powerful insights into adult neurogenic niche biology can be gathered with this approach, it can be argued that it is in fact a lesion model, a type of traumatic brain injury. We and others have shown that cortical lesions ranging from thin needle stabs to wide aspiration lesions activate neurogenic niches and parenchymal astrocytes [40, 10, 11].

Another approach is coupling of 2PM with gradient reafractve index (GRIN) lenses, lowered into the live brain [28]. GRIN lenses have recently been used to rapidly image behaviourally-relevant changes in SGZ neural activity and found that increasing neurogenesis inhibits activation of neurons by social stress [2]. In our hands GRIN lens approaches caused moderate inflammation and the development of a gliotic scar, which is not surprising given that the lenses range from a few to several hundred microns in diameter [21]. Potential imaging-induced inflammation in or around neurogenic niches must be approached cautiously as inflammation can be rapid and long-lasting and is well known to alter neurogenic niche cell behaviours [12, 27, 18, 6].

To overcome these problems, we developed the use of three-photon microscopy (3PM) to perform non-invasive imaging using lasers that pump pho-

tons at long wavelengths of 1,700 nm which significantly reduces the photon scattering problem. 3PM achieves unprecedented penetration depth in imaging biological tissues by combining improved nonlinear confinement and reduced tissue scattering at long wavelengths [15, 30, 41]. In this method, a fluorophore is excited by the simultaneous absorption of three photons of infra-red wavelength. As the wavelength is three times longer than that needed for conventional (single photon) fluorescence excitation, it can lie in the range where scattering and absorption are much lower. 3PM also exhibits high resolution, improves signal to background ratio, captures frames every tens of seconds and is compatible with a wide range of fluorophores. However it was unclear if 3PM could be used to study the deep subcortical SVZ with subcellular resolution to explore cell diversity during lineage progression. Here we shown that with 3PM the cellular morphologies of different cell types were successfully identified in the SVZ, at a maximum depth of ~ 1.5 mm.

4.3 Materials and Methods

4.3.1 Fluorescent dye preparation

CellTracker Orange (C34551), CellTracker Red (C34552) and CellTracker CM-DiI (C7000) were purchased from Life Technologies. CellTracker Orange and CellTracker Red were dissolved in 100% DMSO (Sigma) to a final concentration of 10 mM. CellTracker CM-DiI was dissolved in DMSO to the final concentration of 2 mM. 0.1% Fast Green was added to dyes for tracing ventricular injection when necessary.

4.3.2 Mice and brain injection

Nestin-CreERT2 (016261) [20] and Ai9 (007909) lines were purchased from the Jackson Laboratory. In Nestin-CreERT2+/-;Ai9+/- mice, tamoxifen (Sigma, 150mg/kg) was injected intraperitoneally once daily for 5 consecutive days. CD1 mice were used for dye injection postnatal experiments and C57BL/6J mice for dye injection adult experiments. The postnatal lateral ventricle injection was performed as previously published [39]. In brief, the pups were anesthetized by hypothermia. 0.5-1 µl fluorescent dye was injected and the pups were recovered in a 37°C warming box before returning to the dam. For adult lateral ventricle injections, the mice were first anesthetized with isoflurane and 2 µl fluorescent dye was injected. The stereotactic coordinates from Bregma were as follows: -0.75 mm (AP), 1.2 mm (ML) and -1.9 mm (DV) [7]. A craniotomy window was performed for imaging and a glass window affixed (for SVZ imaging, the window was approximately the size of the area surrounded by the sagittal, coronal and lambdoid sutures). Animal procedures were reviewed and approved by the Cornell Institutional Animal Care and Use Committee. Excluding surgical complications, imaging was successful in 8/8 pups and 5/10 adults.

4.3.3 3PM imaging

Excitation source

The excitation source is a wavelength-tuneable optical parametric amplifier (OPA, Opera-F, Coherent) pumped by a femtosecond laser with a MOPA (Master Oscillator Power Amplifier) architecture (Monaco, Coherent) operating at

1650 nm. A silicon wafer is used to compensate for the dispersion of the optics of the light source and the microscope including the objective. The laser repetition rate is maintained at 333 kHz with a maximum power of 55 mW under the objective lens.

Imaging setup

The images were acquired with a custom-built multiphoton microscope with a high-numerical aperture objective (Olympus XLPLN25XWMP2, 25X, NA 1.05). Two detection channels were used to collect the fluorescence signal and the third harmonic generation (THG) signal by photomultiplier tubes (PMT) with a GaAsP photocathode (H7422-40, Hamamatsu). For RFP imaging at 1650 nm, we used a 593 nm long-pass filter (FF01-593/LP-25, Semrock) for fluorescence and a band-pass 562/40 nm filter (FF01-562/40-25, Semrock) for THG collection. For signal sampling, the PMT current is converted to voltage and low-pass-filtered (20 kHz) by a transimpedance amplifier (C7319, Hamamatsu). Analog-to-digital conversion is performed by a data acquisition card (NI PCI- 6110, National Instruments). The signal acquisition system displayed shot-noise limited performance, and light shielding was carefully done to achieve dark counts of 20-40 photons per second under actual imaging conditions without laser scanning. ScanImage 3.8 (Vidrio Technologies) running on MATLAB (MathWorks) was used to acquire images and control a 3D translation stage to move the sample (MP-285, Sutter Instrument Company). All imaging depths and thickness are reported in raw axial movement of the motorized stage. High resolution structural images were typically taken with 512x512 pixels/frame, 0.24 Hz frame rate, and multiple frame averages at each depth.

4.3.4 Immunohistochemistry and confocal imaging

Immunohistochemistry was performed as previously published [39]. In brief, 3PM imaged mice were perfused and brains were fixed with 4% PFA. Brains were sectioned coronally at 30 µm with a microtome and immunohistochemistry carried out on free-floating sections. Sections were blocked with PBS+ (10% donkey serum, 0.1% Triton-X in PBS) and incubated with primary antibodies overnight at 437, followed with Alexa fluor-conjugated secondary antibodies (Invitrogen). The following primary antibodies were used: rat anti-GFAP (1:500, Invitrogen 130300), goat anti-Dcx (1:100, Santa Cruz sc-8066), goat anti-Iba1 (1:500, Abcam ab5076), rabbit anti-S100β (Dako Z031129-2), mouse anti-Mash1 (1:100, BD Biosciences 556604). DAPI (Sigma) was used for counterstaining cell nuclei blue before mounting. Zeiss confocal scanning microscopes (Model 710 or 800) were used for image acquisition. 1 µm intervals were used for Z-stack scanning.

4.3.5 Image analysis

All images were processed with ImageJ and Imaris (Bitplane). For cell type identification based on morphology, images were filtered with ImageJ 3D suite (Median).

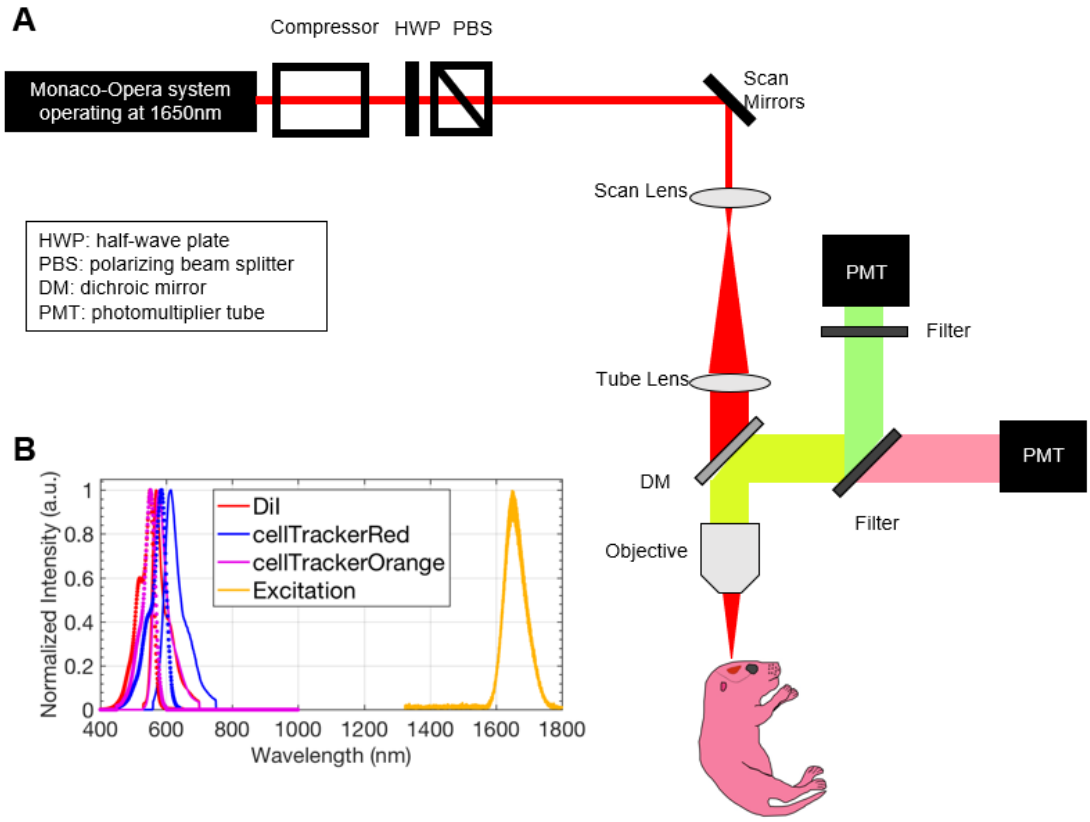

Figure 4.1: 3PM experimental setup and imaging of postnatal SVZ with CTR and DiI (A) Main elements of the 3-photon microscope design. (B) The spectra of the laser (yellow) and excitation (dashed lines) and emission (solid lines) spectra of DiI, CellTracker Red, and CellTracker Orange used for 3-photon imaging. Data for the fluorescent dyes were obtained from Life Technologies, USA.

4.4 Results

We used a custom-built 3PM (Fig. 4.1A). The excitation source was a wavelength-tuneable optical parametric amplifier (OPA, Opera-F, Coherent) operating at 1650 nm to match the excitation wavelength of the fluorescent dyes used in this study. The spectra of the excitation source were confirmed by an Optical Spectrum Analyzer (OSA205C, Thorlabs), shown in Fig. 4.1B. Bandpass

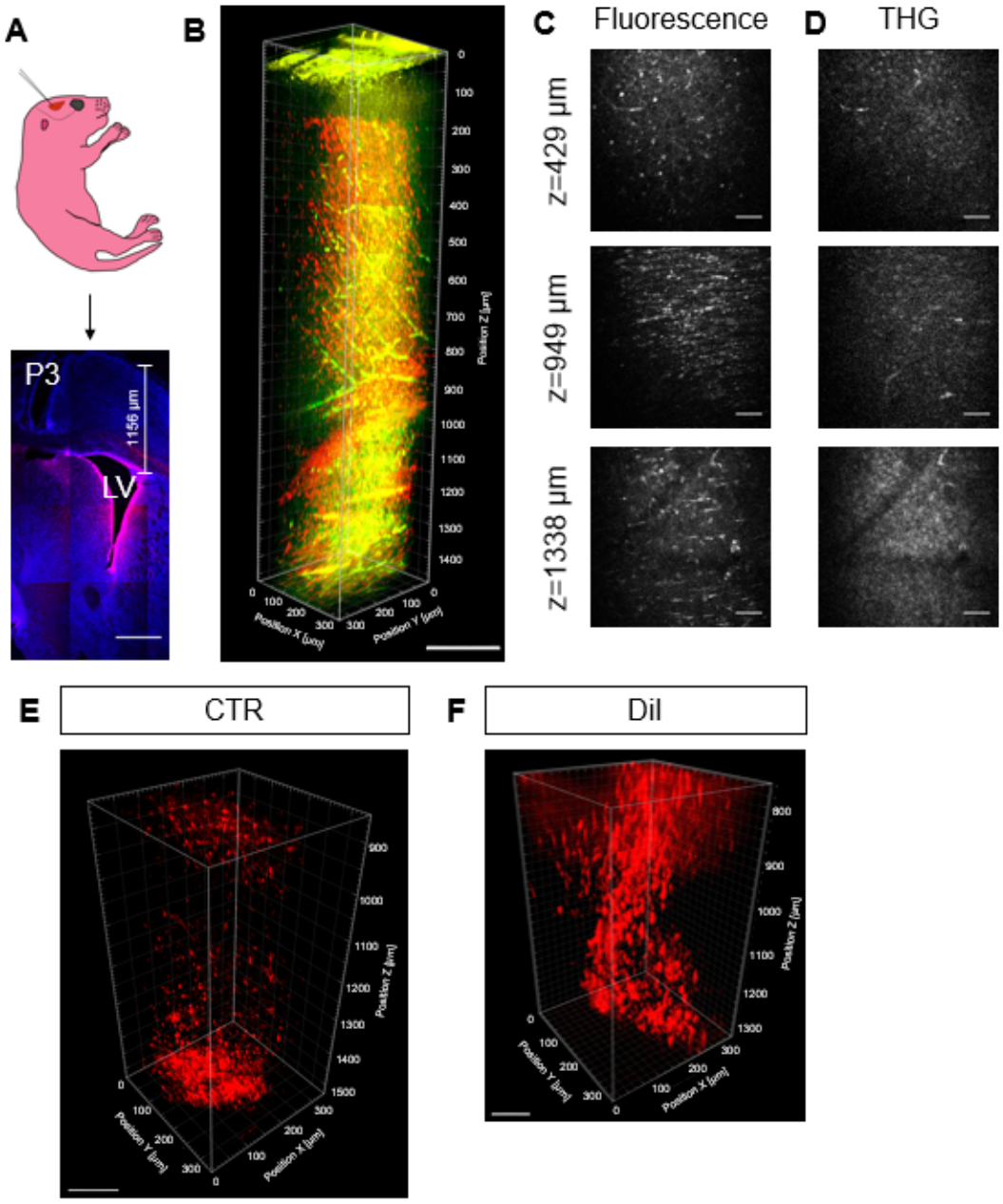

Figure 4.2: Validation of 3PM in postnatal SVZ imaging (A) A schematic of LV injection in postnatal day 1 (P1) pup and confocal imaging of a representative brain section labelled with CTO (red) and DAPI (blue), 2 days post injection. (B) 3D reconstruction from 0-1472 µm below the pial surface (red, CTO fluorescence; green, THG). (C-D) Selected XY frames at different depths in (B). (E) 3D reconstruction of white matter and SVZ of pups injected with CTR. (F) 3D reconstruction of white matter and SVZ of pups injected with DiI. Scale bars represent 500 µm in A, 200 µm in B, 50 µm in C and D, 100 µm in E; 80 µm in F.

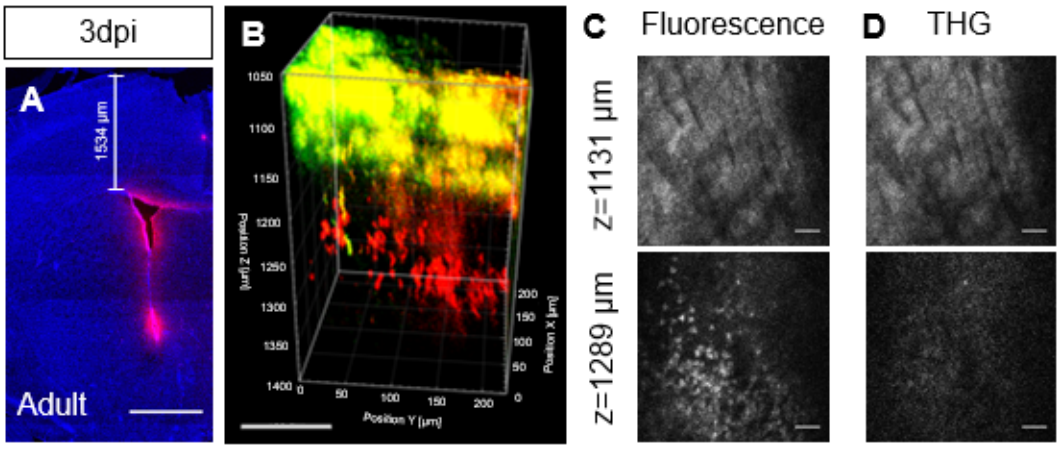

Figure 4.3: Validation of 3PM in adult SVZ imaging (A) Confocal imaging of a representative adult brain section labelled with CTO (red) and DAPI (blue) at 3dpi. (B) 3D reconstruction of white matter (THG) and CTO-labelled SVZ from the depth of 1050-1400 µm in an adult mouse (red, CTO fluorescence; green, THG). (C-D) Selected XY frames at different depths in (B). Scale bars represent 1000 µm in A, 100 µm in B, 30 µm in C and D.

filters were added in the detection paths to separate third-harmonic generation (THG) signal from fluorescence signal. THG is generated at the interface of materials with different third-order susceptibility [4]. In this study, we used THG to locate corpus callosum (CC) white matter depth as the SVZ lies immediately below the CC. CellTracker Orange (CTO) was injected into the lateral ventricle (LV) of P0-P1 pups under anaesthesia and imaging was performed 3 days post injection (dpi) (Fig. 4.2A). We acquired approximately 1500 µm stacks (Fig. 4.2B, C, D). CTO fluorescent signals were found throughout the stack, but predominantly below 1000 µm, which was also confirmed with post-imaging histology (Fig. 4.2A, B). Other fluorescent dyes tested included CellTracker Red (CTR) (Fig. 4.2E) and DiI (Fig. 4.2F), and similar results were obtained. Compared to postnatal brains, young adult brains contain mature myelinating oligodendrocytes in the corpus callosum and are therefore more light scattering. To confirm

SVZ visualisation in young adult brains, we injected CTO into the LV of 5 to 8-week-old mice. CTO fluorescence was detected around the LV as well as in the corpus callosum, resulting from the injection and diffusion of the dye into adjacent regions (Figs. 4.3A). The THG signal in the CC was more distinguishable in young adults than in neonates and extended from ~1000 µm to ~1153 µm in depth. Below the CC we found clearly labelled CTO+ cells (Fig. 4.3B, C, D). For depth measurement, the slightly larger index of refraction in brain tissue (1.35 - 1.40 for the cortex [3, 8] and as high as 1.47 for the white matter [3], relative to water (~1.33), resulted in a slight underestimate (5-10%) of the actual imaging depth within the tissue, because the imaging depths reported here are the raw axial movement of the objective lens. To provide an upper-bound estimate of the spatial resolution, we measured the lateral brightness distribution of small features within the adult mouse brain (Fig. 4.4A) at 1039 µm depth. The full-widths at half maximum (FWHM) of the lateral brightness distributions is about 0.86 µm (Fig. 4.4B). The axial FWHM value is measured to be around 4.45 µm in pup brain at 1371 µm depth shown in Fig. 4.4C and 4.4D.

To evaluate the cytoarchitecture of the postnatal SVZ, we examined CTO+ cells below the corpus callosum. As examples, at depths of 1288 and 1430 µm, cells with elongating basal processes, with approximate diameters of 1 µm, were observed (Fig. 4.5A, B). These cells lined the LV wall, and morphologically resembled radial glial cells (RGC) which are postnatal SVZ stem cells (Fig. 4.5A, B). Importantly, when we followed these cells to the adjacent striatum, we found their basal processes in close proximity to blood vessels (Fig. 4.5C), which allows NSC to be controlled by extrinsic signals from the vascular niche [26, 36]. To confirm this interaction, 3D reconstructions showed fine processes of NSC surrounding blood vessels (Fig. 4.5D). Direct physical contact between these cells

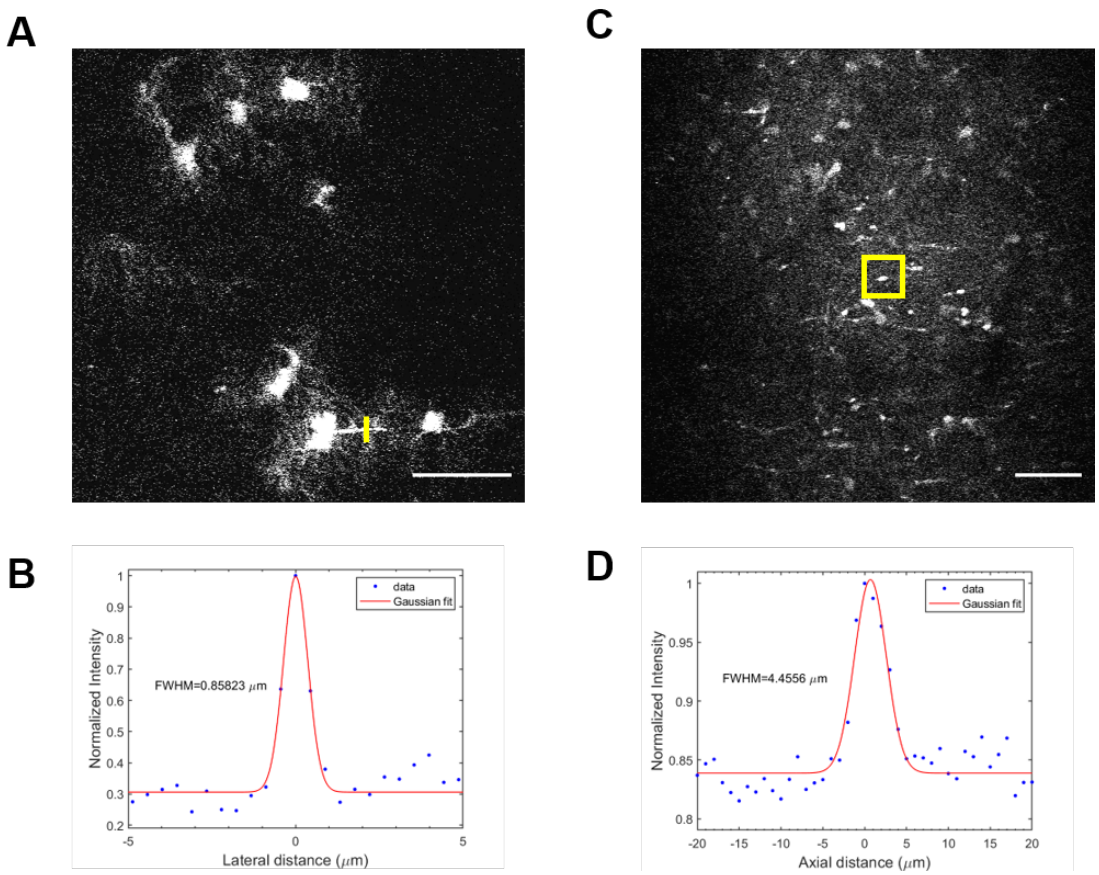

Figure 4.4: Intensity profiles of subcellular structures (A-B) The lateral brightness distribution of small features within the adult mouse brain (A) at 1039 µm depth and the FWHM of the lateral brightness distributions (B). (C-D) The axial brightness distribution of small features within the postnatal mouse brain (C) at 1371 µm depth and the FWHM of the axial brightness distributions (D). Scale bars represent 50 µm in A and C.

was further proved by filament tracking of representative processes (Fig. 4.5E). Immunohistochemistry further confirmed that the CTO+ cells with NSC morphologies described above expressed GFAP, a protein found in NSC (Fig. 4.5F) [16].

To follow SVZ lineage progression, we next imaged pups at a later time point after CTO injection, i.e. P8. Since TAPs are difficult to identify based

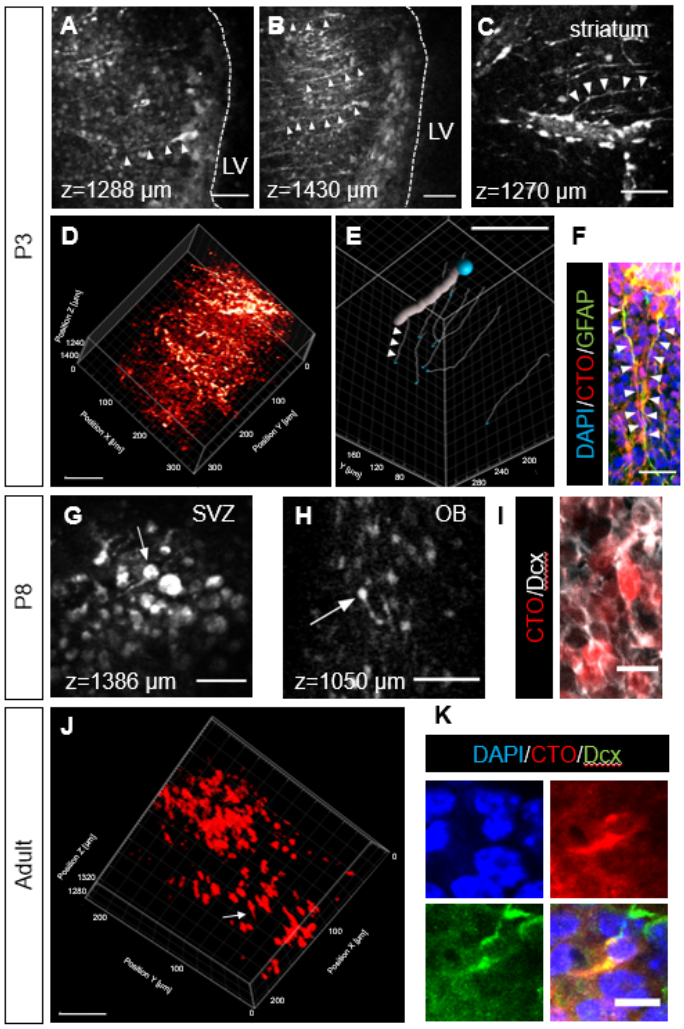

Figure 4.5: 3PM imaging of SVZ and OB cell types (A-C) Representative 3PM images of RGC like neural stem cells at different depths. Arrowheads indicate neural stem cells. (D) 3D reconstruction of white matter and SVZ from the depth of 1150-1472 µm. (E) Filament tracking in 3D reconstruction (D). The thick line indicates a blood vessel and the thin lines indicate individual cellular processes from different 3PM-imaged NSCs. (F) Immunostaining of GFAP in SVZ. The arrowheads indicate the basal processes of two neural stem cells labelled by both CTO and GFAP. (G-H) Representative 3PM images of neuroblasts at the depth of 1386µm in SVZ (G) or 1050µm in OB (H). The arrows indicate neuroblasts. (I) Immunostaining of Dcx in OB showing CTO+ neuroblasts. (J) 3D reconstruction of SVZ from the depth of 1271-1325 µm. (K) Immunostaining of Dcx in SVZ. The arrow indicates a cell with the morphology of a neuroblast. Scale bars represent 50 µm in A, B, C, G, H, J; 80 µm in D; 100 µm in E; 20 µm in F; 10 µm in I and K.

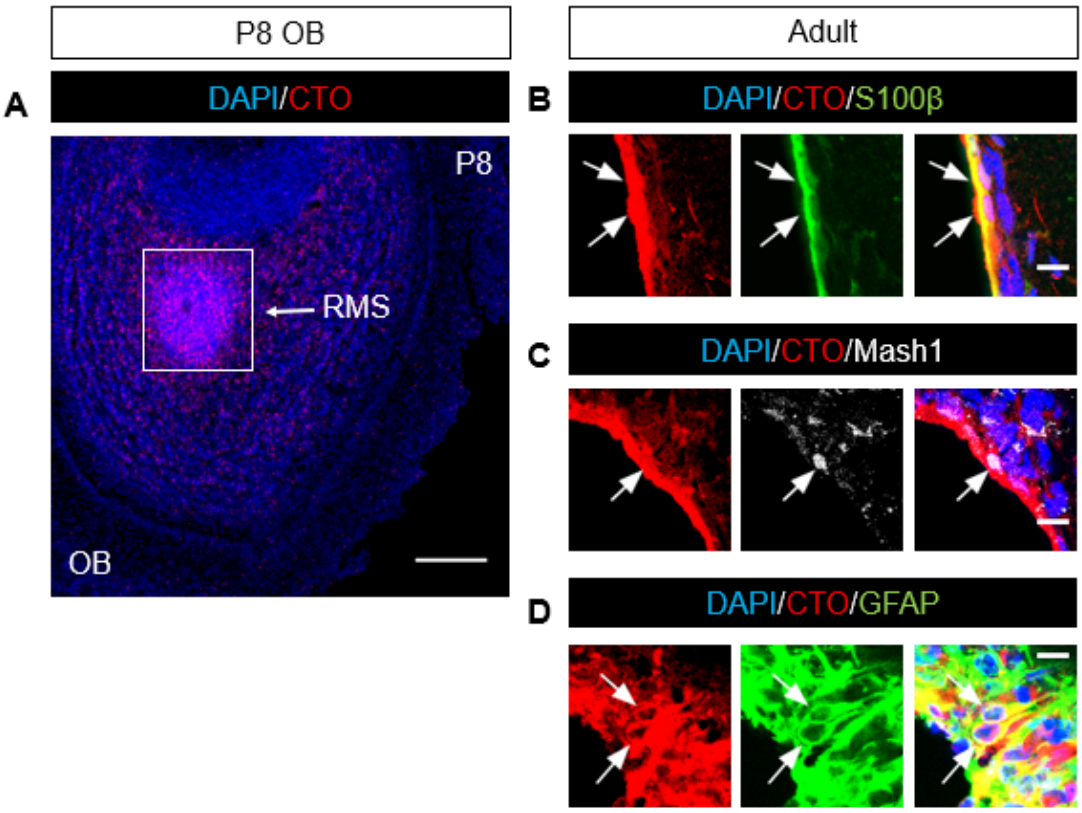

Figure 4.6: Immunohistochemistry of P8 OB and adult SVZ (A) Confocal imaging of a representative brain section labelled with CTO (red) in the RMS extending into the OB. (B) Immunostaining of S100 in the SVZ. Arrows indicate ependymal cells. (C) Immunostaining of Mash1 in the SVZ. The arrow indicates a transit amplifying progenitor. (D) Immunostaining of GFAP in the SVZ. Arrows indicate the neural stem cells. Scale bars represent 200 µm in A; 10 µm in B, C, D.

on morphology, we chose to examine SVZ neuroblasts which are small bipolar cells with distinctive leading processes. Cells with neuroblast-morphology were found in the SVZ, for example at a depth of 1386 µm (Fig. 4.5G). CTO may label multiple cell types in the SVZ rather than revealing lineage progression. Therefore, to more definitively identify lineage progression, we imaged CTO+ neuroblasts generated in the SVZ that migrated into the olfactory bulb (OB) from the RMS. We focused on the OB-core RMS and detected CTO+ cells

(Fig. 4.6A). These 3PM-detected cells exhibited leading processes (Fig. 4.5H) and were co-stained with Dcx (Fig. 4.5I), which together supported their neuroblast identity.

In the adult brain, CTO+ cells also exhibited morphological diversity (Fig. 4.5J). An example of a 3PM-detected unipolar neuroblast with a leading process is shown in Fig. 4.5J, and a cell with similar morphology was confirmed to be a neuroblast with Dcx staining (Fig. 4.5K). Post-imaging immunohistochemical analysis confirmed various other SVZ niche cell types, S100β+ ependymal cells (Fig. 4.6B), Mash1+ TAPs (Fig. 4.6C) and GFAP+ NSC (Fig. 4.6D) and which were labelled by CTO at 3 days post injection (3dpi) or 17dpi. Conditionally inducible Nestin-CreERT2;Ai9 mice were then used to specifically label SVZ stem cells and their progeny [20, 24]. Expression of tdTomato was induced in NSC with tamoxifen injections, and imaging was performed 4 weeks later to analyse lineage progression (Fig. 4.7A). A dense population of tdTomato+ cells was observed in the SVZ, surrounded by white matter (Fig. 4.7B). These experiments confirm the CTO data above and show that 3PM can be used to study live SVZ neurogenesis in this frequently used reporter mouse. Although the majority of SVZ NSC generate interneurons in the OB, a small proportion of them contribute to the astrocyte turnover in the corpus callosum [43, 38]. Consistently, tdTomato+ cells were found in the white matter, for example at the depth of 1037 µm (Fig. 4.7C). Unlike bushy protoplasmic astrocytes, these cells exhibited fewer but thicker branches (Fig. 4.7C), a feature of fibrous astrocytes in the white matter [34].

We kept the maximum power at the brain surface to be below 55 mW for all imaging sessions, and we queried if our *in vivo* 3PM imaging may cause inflam-

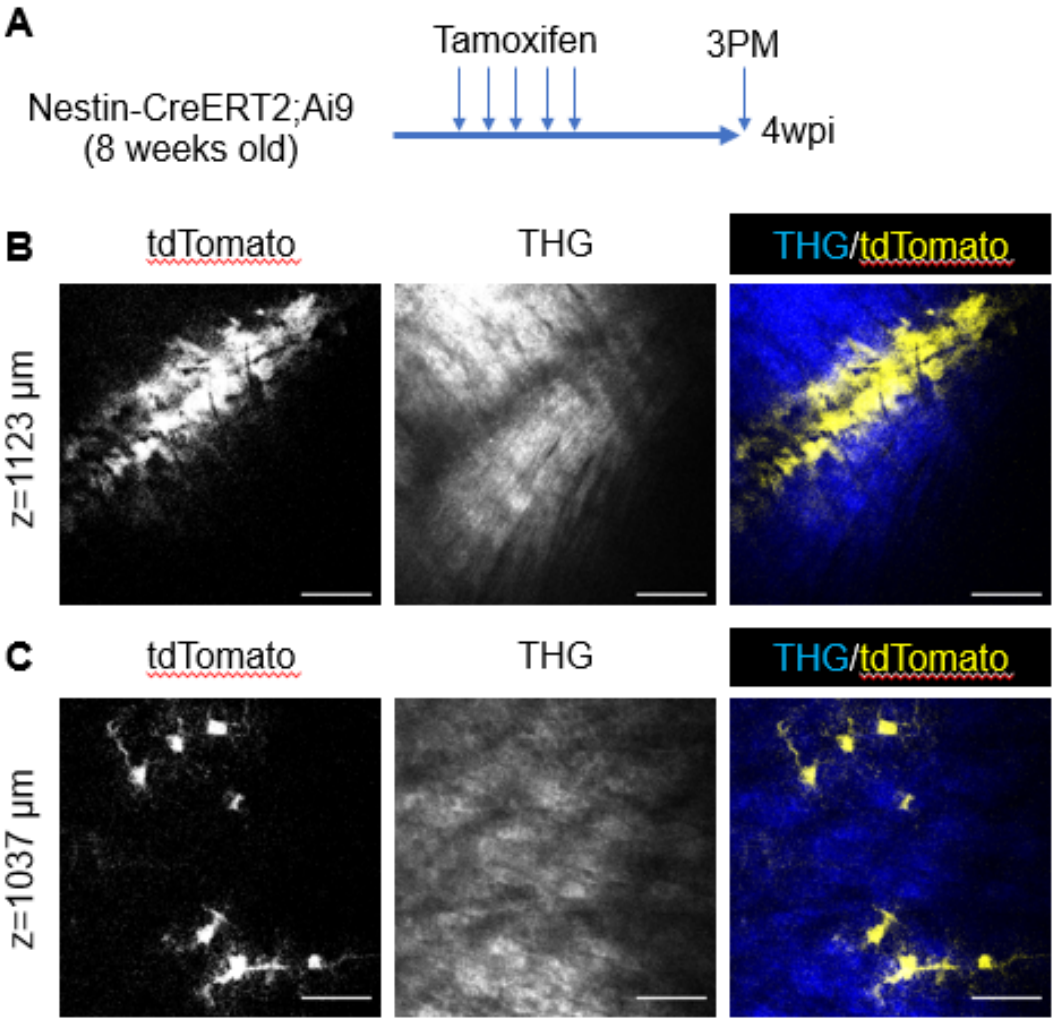

Figure 4.7: 3PM imaging of Nestin-CreER2;Ai9 (A) A schematic of the experimental design. (B) A representative image of the SVZ at the depth of 1123 µm. (C) A representative image of the corpus callosum with fibrous astrocytes (yellow) at the depth of 1037 µm. Scale bars represent 50 µm in B and C.

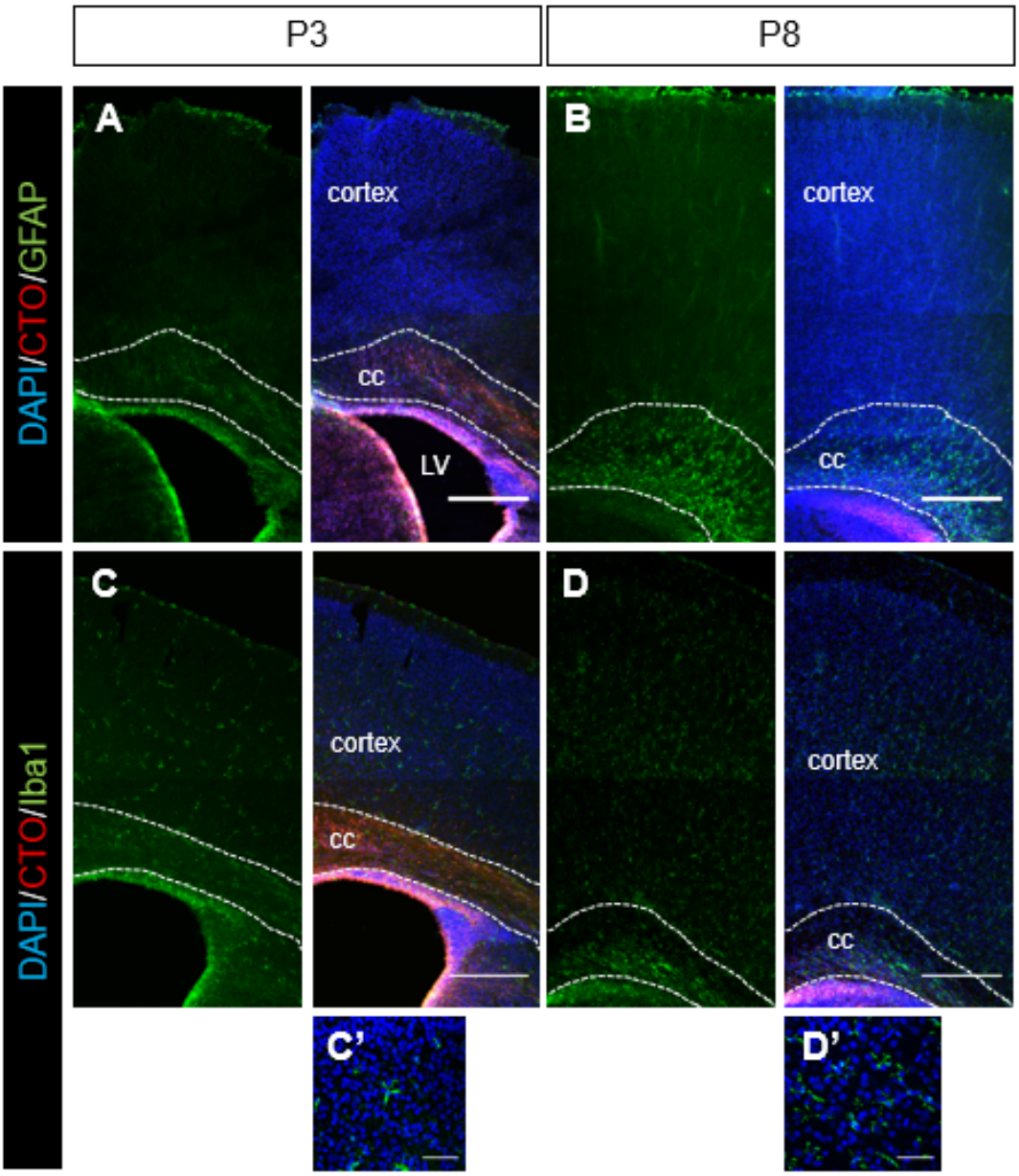

Figure 4.8: Gliosis analysis in the ipsilateral cortex of 3PM imaged postnatal pups (A-B) Immunohistochemistry of GFAP in P3 and P8 brain sections. (C-D) Immunohistochemistry of Iba1 in P3 and P8 brain sections. c′ and d′ are high magnification images of Iba1+ cells in cortex in c and d, respectively. Scale bars represent 300 µm in A, B, C, and D; µm in C′ and D′.

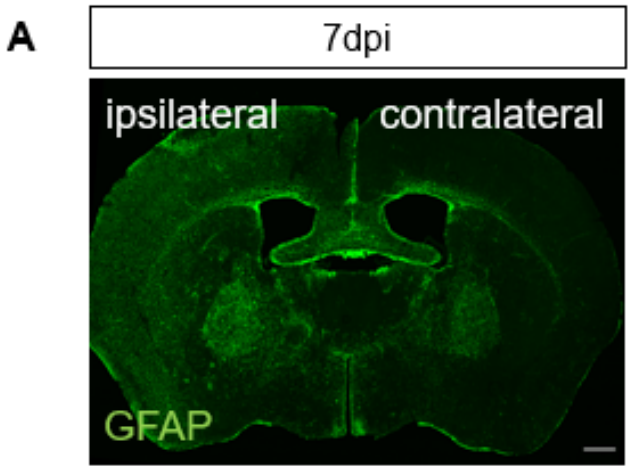

Figure 4.9: Immunohistochemistry of non-imaged brain (A) Immunohistochemistry of GFAP in adult brain sections from mice with craniotomy surgery, but which did not have 3PM imaging. Scale bar represents 500 µm.

mation. We investigated cortical gliosis, a hallmark of inflammation, in mice imaged at different ages. When assessing P3 an P8 pups after acute imaging with 3PM, we could see neither reactive GFAP+ astrocytes (Fig. 4.8A, B) nor Iba1+ activated microglia (Fig. 4.8C, D) in the cerebral cortex. Reactive GFAP+ astrocytes were found in the ipsilateral side of the adult cortex at both 3dpi and 17dpi (Fig. 4.10A), however, without obvious inflammation (Iba1) (Fig. 4.10B). Without 3PM imaging, astrocyte activation was also noticed in animals with craniotomy surgery (Fig. 4.9A). This is consistent with evidence that open-skull glass windows, as used here, activate cortical astrocytes [42].

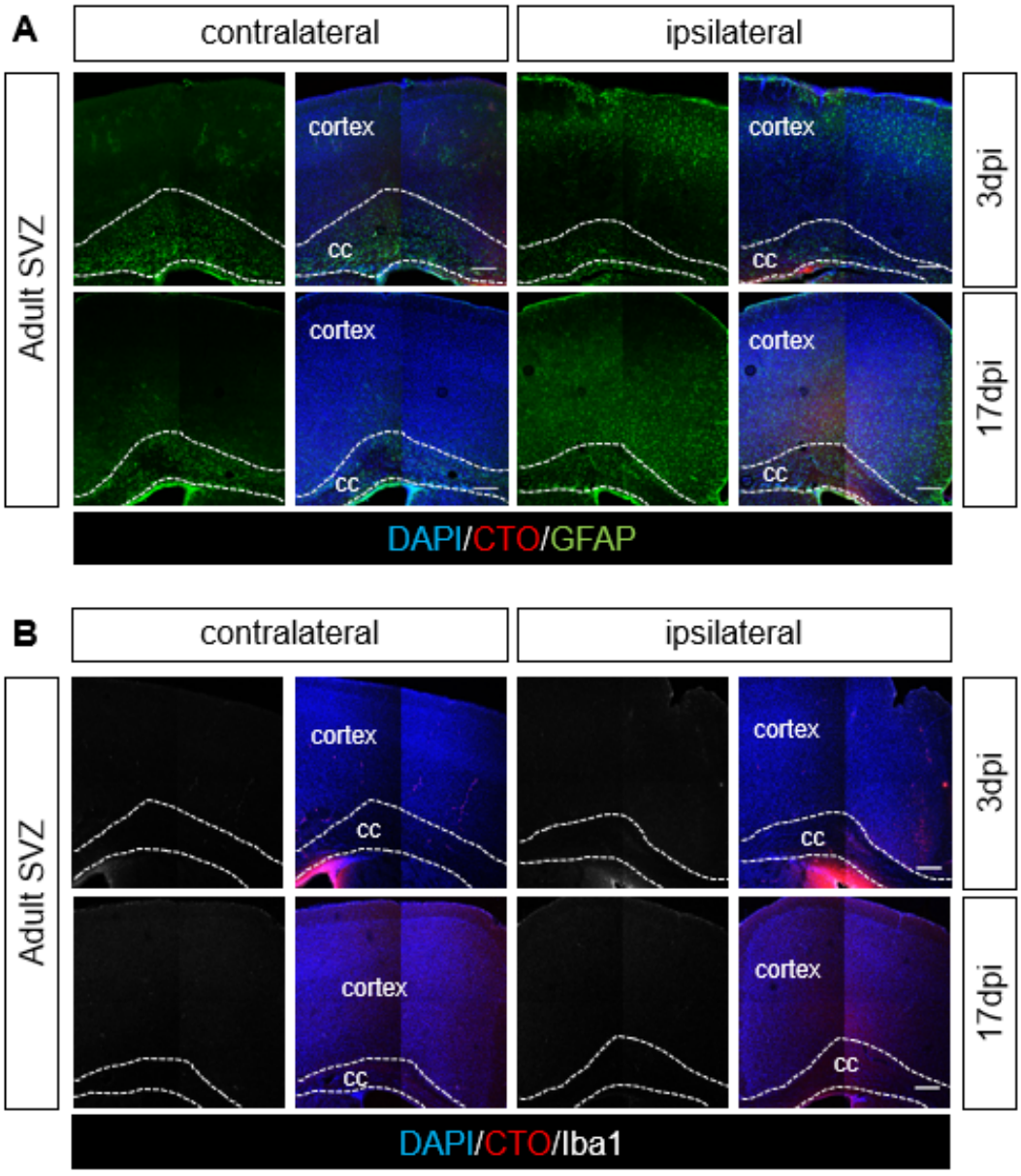

Figure 4.10: (A) Immunohistochemistry of GFAP in adult brain sections, 3 days or 17 days post injection. (B) Immunohistochemistry of Iba1 in adult brain sections, 3 days or 17 days post injection. Scale bars represent 200 µm in A and B.

4.5 Discussion

In summary, we proved the utility of 3PM to visualise the murine SVZ at different ages. Of note was that multiple means of labelling SVZ cells with dyes and genetically were compatible with 3PM. SVZ cell type identification has long been a major challenge for live imaging [19]. Here with 3PM, we successfully identified multiple cell types based on morphological analysis. Results from post-hoc immunohistochemistry and multiple labelling techniques show good morphological concordance between 3PM and histological or ex-vivo detection of morphological SVZ cell types.

3PM requires robust advanced laser sources which are now available from commercial suppliers (Coherent and Spectra-Physics). The optical parametric amplifier systems provided the correct combination of short-pulse duration, repetition rate and pulse energy required for effective imaging. The higher penetration depth presented further challenges; the non-uniform refractive index structure of brain means wavefronts of light propagating to the focus can be distorted, resulting in blurred aberrations with reduced intensity. The reduction in intensity is particularly problematic in 3PM, as the fluorescence excitation efficiency is proportional to the third power of the focal intensity. A 50% drop in focal intensity causes the fluorescence to drop to 12.5% of its original level. Even though longer excitation wavelengths are less susceptible to scattering, aberration effects are significant at depths of 100 s of micrometres to millimetres and can easily cause a drop in focal intensity to below 10%. There is a solution to this problem in the form of adaptive optics (AO), whereby active optical elements, such as deformable mirrors or spatial light modulators, compensate for the aberrations. Thus, focus can be restored to near ideal state and the excitation

efficiency improved [9].

In conclusion, we have developed a non-damaging approach to imaging the live SVZ over multiple ages. This system should be useful for acute imaging of very rapid cellular events such as changes in calcium concentrations (milliseconds to seconds). It could also be suitable for key SVZ cell behaviours such as migration (minutes to hours) and stem cell activation or proliferation (hours to days). Similar to [33], 3PM could be used for imaging clonal evolution in homeostasis or in models of SVZ gliomagenesis [5]. We predict that 3PM will also become very useful for imaging and the study of molecular mechanisms and the response of the SVZ to models and treatment of disease.

Bibliography

[1] Joseph Altman. Autoradiographic and histological studies of postnatal neurogenesis. IV. cell proliferation and migration in the anterior forebrain, with special reference to persisting neurogenesis in the olfactory bulb. 137(4):433–457.

[2] Christoph Anacker, Victor M. Luna, Gregory S. Stevens, Amira Millette, Ryan Shores, Jessica C. Jimenez, Briana Chen, and Ren Hen. Hippocampal neurogenesis confers stress resilience by inhibiting the ventral dentate gyrus. 559(7712):98.

[3] Robert Bacallao, Sadaf Sohrab, and Carrie Phillips. Guiding principles of specimen preservation for confocal fluorescence microscopy. In James B. Pawley, editor, *Handbook Of Biological Confocal Microscopy*, pages 368–380. Springer US.

[4] Y. Barad, H. Eisenberg, M. Horowitz, and Y. Silberberg. Nonlinear scanning laser microscopy by third harmonic generation. 70(8):922–924.

[5] Chiara Bardella, Osama Al-Dalahmah, Daniel Krell, Pijus Brazauskas, Khalid Al-Qahtani, Marketa Tomkova, Julie Adam, Sbastien Serres, Helen Lockstone, Luke Freeman-Mills, Inga Pfeffer, Nicola Sibson, Robert Goldin, Benjamin Schuster-Beckler, PatrickJ. Pollard, Tomoyoshi Soga, JamesS. McCullagh, ChristopherJ. Schofield, Paul Mulholland, Olaf Ansorge, Skirmantas Kriaucionis, PeterJ. Ratcliffe, FrancisG. Szele, and Ian Tomlinson. Expression of idh1r132h in the murine subventricular zone stem cell niche recapitulates features of early gliomagenesis. 30(4):578–594.

[6] Chiara Bardella, Abeer R. Al-Shammari, Luana Soares, Ian Tomlinson, Eric O'Neill, and Francis G. Szele. The role of inflammation in subventricular zone cancer. 170:37–52.

[7] Ruth Beckervordersandforth, Pratibha Tripathi, Jovica Ninkovic, Efil Bayam, Alexandra Lepier, Barbara Stempfhuber, Frank Kirchhoff, Johannes Hirrlinger, Anja Haslinger, D. Chichung Lie, Johannes Beckers, Bradley Yoder, Martin Irmler, and Magdalena Gtz. In vivo fate mapping and expression analysis reveals molecular hallmarks of prospectively isolated adult neural stem cells. 8(1):119.

[8] Jonas Binding, Juliette Ben Arous, Jean-Franois Lger, Sylvain Gigan, Claude Boccara, and Laurent Bourdieu. Brain refractive index measured in vivo with high-NA defocus-corrected full-field OCT and consequences for two-photon microscopy. 19(6):4833–4847.

[9] Martin J. Booth, Mark A. A. Neil, Rimas Jukaitis, and Tony Wilson. Adaptive aberration correction in a confocal microscope. 99(9):5788–5792.

[10] Annalisa Buffo, Inmaculada Rite, Pratibha Tripathi, Alexandra Lepier, Dilek Colak, Ana-Paula Horn, Tetsuji Mori, and Magdalena Gtz. Origin and progeny of reactive gliosis: A source of multipotent cells in the injured brain. 105(9):3581–3586.

[11] Eun Hyuk Chang, Istvan Adorjan, Mayara V. Mundim, Bin Sun, Maria L. V. Dizon, and Francis G. Szele. Traumatic brain injury activation of the adult subventricular zone neurogenic niche. 10.

[12] Christine T. Ekdahl, Jan-Hendrik Claasen, Sara Bonde, Zaal Kokaia, and Olle Lindvall. Inflammation is detrimental for neurogenesis in adult brain. 100(23):13632–13637.

[13] Peter S. Eriksson, Ekaterina Perfilieva, Thomas Bjrk-Eriksson, Ann-Marie Alborn, Claes Nordborg, Daniel A. Peterson, and Fred H. Gage. Neurogenesis in the adult human hippocampus. 4(11):1313–1317.

[14] Aurlie Ernst, Kanar Alkass, Samuel Bernard, Mehran Salehpour, Shira Perl, John Tisdale, Gran Possnert, Henrik Druid, and Jonas Frisn. Neurogenesis in the striatum of the adult human brain. 156(5):1072–1083.

[15] Nicholas G. Horton, Ke Wang, Demirhan Kobat, Catharine G. Clark, Frank W. Wise, Chris B. Schaffer, and Chris Xu. *In vivo* three-photon microscopy of subcortical structures within an intact mouse brain. *Nat. Photonics*, 7(3):205–209, March 2013.

[16] RebeccaA. Ihrie and Arturo lvarez Buylla. Lake-front property: A unique germinal niche by the lateral ventricles of the adult brain. 70(4):674–686.

[17] Rachel James, Yongsoo Kim, Philip Hockberger, and Francis G. Szele. Sub-

ventricular zone cell migration: Lessons from quantitative two-photon microscopy. 5.

[18] Rachel E. James, James Hillis, Istvn Adorjn, Betty Gration, Mayara V. Mundim, Asif J. Iqbal, Moon-Moon Majumdar, Richard L. Yates, Maureen M. H. Richards, Gwendolyn E. Goings, Gabriele C. DeLuca, David R. Greaves, Stephen D. Miller, and Francis G. Szele. Loss of galectin-3 decreases the number of immune cells in the subventricular zone and restores proliferation in a viral model of multiple sclerosis. 64(1):105–121.

[19] Benjamin Lacar, Stephanie Z. Young, Jean-Claude Platel, and Angelique Bordey. Imaging and recording subventricular zone progenitor cells in live tissue of postnatal mice. 4.

[20] Diane C. Lagace, Mary C. Whitman, Michele A. Noonan, Jessica L. Ables, Nathan A. DeCarolis, Amy A. Arguello, Michael H. Donovan, Stephanie J. Fischer, Laure A. Farnbauch, Robert D. Beech, Ralph J. DiLeone, Charles A. Greer, Chitra D. Mandyam, and Amelia J. Eisch. Dynamic contribution of nestin-expressing stem cells to adult neurogenesis. 27(46):12623–12629.

[21] Seon A. Lee, Kevin S. Holly, Vladislav Voziyanov, Stephanie L. Villalba, Rudi Tong, Holly E. Grigsby, Edward Glasscock, Francis G. Szele, Ioannis Vlachos, and Teresa A. Murray. Gradient index microlens implanted in prefrontal cortex of mouse does not affect behavioral test performance over time. 11(1):e0146533.

[22] Steven W. Levison and James E. Goldman. Both oligodendrocytes and astrocytes develop from progenitors in the subventricular zone of postnatal rat forebrain. 10(2):201–212.

[23] Enric Llorens-Bobadilla, Sheng Zhao, Avni Baser, Gonzalo Saiz-Castro, Klara Zwadlo, and Ana Martin-Villalba. Single-cell transcriptomics reveals a population of dormant neural stem cells that become activated upon brain injury. 17(3):329–340.

[24] Linda Madisen, Theresa A. Zwingman, Susan M. Sunkin, Seung Wook Oh, Hatim A. Zariwala, Hong Gu, Lydia L. Ng, Richard D. Palmiter, Michael J. Hawrylycz, Allan R. Jones, Ed S. Lein, and Hongkui Zeng. A robust and high-throughput cre reporting and characterization system for the whole mouse brain. 13(1):133–140.

[25] Noelia Martinez-Molina, Yongsoo Kim, Philip Hockberger, and Francis G. Szele. Rostral migratory stream neuroblasts turn and change directions in stereotypic patterns. 5(1):83–95.

[26] Zaman Mirzadeh, Florian T. Merkle, Mario Soriano-Navarro, Jose Manuel Garcia-Verdugo, and Arturo Alvarez-Buylla. Neural stem cells confer unique pinwheel architecture to the ventricular surface in neurogenic regions of the adult brain. 3(3):265–278.

[27] Michelle L. Monje, Hiroki Toda, and Theo D. Palmer. Inflammatory blockade restores adult hippocampal neurogenesis. 302(5651):1760–1765.

[28] Teresa A. Murray and Michael J. Levene. Singlet gradient index lens for deep *in vivo* multiphoton microscopy. 17(2):021106.

[29] Sang Chae Nam, Yongsoo Kim, Dilyan Dryanovski, Avery Walker, Gwendolyn Goings, Kevin Woolfrey, Seong Su Kang, Chris Chu, Anjen Chenn, Ferenc Erdelyi, Gabor Szabo, Philip Hockberger, and Francis G. Szele.

Dynamic features of postnatal subventricular zone cell motility: A two-photon time-lapse study. 505(2):190–208.

[30] Dimitre G. Ouzounov, Tianyu Wang, Mengran Wang, Danielle D. Feng, Nicholas G. Horton, Jean C. Cruz-Hernndez, Yu-Ting Cheng, Jacob Reimer, Andreas S. Tolias, Nozomi Nishimura, and Chris Xu. In vivo three-photon imaging of activity of GCaMP6-labeled neurons deep in intact mouse brain. 14(4):388–390.

[31] Mercedes F. Paredes, David James, Sara Gil-Perotin, Hosung Kim, Jennifer A. Cotter, Carissa Ng, Kadellyn Sandoval, David H. Rowitch, Duan Xu, Patrick S. McQuillen, Jose-Manuel Garcia-Verdugo, Eric J. Huang, and Arturo Alvarez-Buylla. Extensive migration of young neurons into the infant human frontal lobe. 354(6308):aaf7073.

[32] Gregor-Alexander Pilz, Sara Bottes, Marion Betizeau, David J. Jrg, Stefano Carta, Benjamin D. Simons, Fritjof Helmchen, and Sebastian Jessberger. Live imaging of neurogenesis in the adult mouse hippocampus. 359(6376):658–662.

[33] Gregor-Alexander Pilz, Stefano Carta, Andreas Stuble, Asli Ayaz, Sebastian Jessberger, and Fritjof Helmchen. Functional imaging of dentate granule cells in the adult mouse hippocampus. 36(28):7407–7414.

[34] Stefanie Robel, Benedikt Berninger, and Magdalena Gtz. The stem cell potential of glia: lessons from reactive gliosis. 12(2):88–104.

[35] Nader Sanai, Thuhien Nguyen, Rebecca A. Ihrie, Zaman Mirzadeh, Hui-Hsin Tsai, Michael Wong, Nalin Gupta, Mitchel S. Berger, Eric Huang, Jose-Manuel Garcia-Verdugo, David H. Rowitch, and Arturo Alvarez-Buylla.

Corridors of migrating neurons in the human brain and their decline during infancy. 478(7369):382–386.

[36] Qin Shen, Yue Wang, Erzsebet Kokovay, Gang Lin, Shu-Mien Chuang, Susan K. Goderie, Badrinath Roysam, and Sally Temple. Adult SVZ stem cells lie in a vascular niche: A quantitative analysis of niche cell-cell interactions. 3(3):289–300.

[37] Violeta Silva-Vargas, Angel R. Maldonado-Soto, Dogukan Mizrak, Paolo Codega, and Fiona Doetsch. Age-dependent niche signals from the choroid plexus regulate adult neural stem cells. 19(5):643–652.

[38] Jiho Sohn, Lori Orosco, Fuzheng Guo, Seung-Hyuk Chung, Peter Bannerman, Emily Mills Ko, Kostas Zarbalis, Wenbin Deng, and David Pleasure. The subventricular zone continues to generate corpus callosum and rostral migratory stream astroglia in normal adult mice. 35(9):3756–3763.

[39] Bin Sun, Eunhyuk Chang, Anna Gerhartl, and Francis G. Szele. Polycomb protein eed is required for neurogenesis and cortical injury activation in the subventricular zone. 28(4):1369–1382.

[40] F. G. Szele and M. F. Chesselet. Cortical lesions induce an increase in cell number and PSA-NCAM expression in the subventricular zone of adult rats. 368(3):439–454.

[41] Mengran Wang, Chunyan Wu, David Sinefeld, Bo Li, Fei Xia, and Chris Xu. Comparing the effective attenuation lengths for long wavelength in vivo imaging of the mouse brain. 9(8):3534–3543.

[42] Hua-Tai Xu, Feng Pan, Guang Yang, and Wen-Biao Gan. Choice of cranial

window type for *in vivo* imaging affects dendritic spine turnover in the cortex. 10(5):549–551.

[43] Helen K. C. Yang, Nikki L. SundholmPeters, Gwendolyn E. Goings, Avery S. Walker, Kenneth Hyland, and Francis G. Szele. Distribution of doublecortin expressing cells near the lateral ventricles in the adult mouse brain. 76(3):282–295.

[44] Christopher C. Young, Keith J. Brooks, Alastair M. Buchan, and Francis G. Szele. Cellular and molecular determinants of stroke-induced changes in subventricular zone cell migration. 14(10):1877–1888.

CHAPTER 5

NON-INVASIVE THREE-PHOTON CHRONIC IMAGING OF NEURAL ACTIVITY IN *DROSOPHILA*

5.1 Abstract

Animals exhibit changes in neural activity over long time scales, affecting behaviours ranging from food foraging to mating drive. A limitation to examining neural activity chronically in the fly, *Drosophila melanogaster*, with current methods is the need to remove the head cuticle and underlying tissue to access the brain, a process that damages circulation and restricts the length of the imaging time. Here, we developed a non-invasive chronic imaging method for flies that uses three-photon microscopy, and captured neural structure and activity through the intact fly cuticle. We performed chronic functional imaging of odour-evoked neural activity in the mushroom body Kenyon cells and found odour responses changed over time; sharp odour evoked responses gradually switched to persistent neural activity. Our results demonstrate that three-photon microscopy extends the time limits of the current *in vivo* imaging methods used in flies for anatomical and functional imaging, and opens up new ways to chronically capture neural activity from the fly brain.

5.2 Introduction

Animal nervous systems across lineages have evolved to solve many of the same problems such as foraging for food and water, finding mates to reproduce,

and avoiding predators to stay alive. They must navigate their environment via coordinated movements, and learn and remember the relative values of sensory stimuli around them in order to maximize their fitness and survival. At each instant in time, an animal must evaluate external sensory information based on its current behavioural state to decide what to do next [35, 22, 11, 6, 20, 18]. A major technological challenge to revealing how the brain encodes behavioural states in real time is that even the simplest neural computation involves interactions across the nervous system at various time scales, while our tools for assessing neural activity are restricted in time and space because of currently available imaging sensors, methods, and preparations [14]. Optical methods remain the most established and fruitful path for revealing population dynamics in neural circuits at long time scales (ranging from minutes to hours) by providing high temporal and spatial resolution measurements [17, 33, 13].

The fly, *Drosophila melanogaster*, offers an ideal experimental system to investigate neural correlates of behavioural states and decisions because of its compact nervous system and diverse state-dependent behaviours that it executes in response to sensory stimuli [6, 43, 2]. To understand how neural circuits evaluate sensory information in different behavioural states, it is critical to capture the activity of the molecularly defined populations of neurons over long time scales as flies are changing their physiological needs [17, 30]. These functional imaging experiments require high-speed volumetric imaging methods and non-invasive imaging preparations, which should allow chronic neural activity imaging for at least 12 to 24 hours. Current methods used in fly optical physiology require the fly head cuticle, trachea, and fat body to be removed by microsurgery to provide optical access to the nervous system [7, 21, 31, 28, 37]. These preparations are limited in imaging duration because after some time, the

brain tissue starts dying. For example, with current imaging preparations, fly olfactory neurons show reliable Ca^{2+} responses for about four to five hours after surgery [37]. A non-invasive imaging method using long wavelength excitation and a preparation in which the head cuticle and underlying tissue are left intact, thereby eliminating the need for traumatic head surgery before functional imaging, is essential for advancing fly neuroscience research in the direction of chronic recordings of neural activity during ongoing behaviours. This includes being able to image the same fly brain across multiple days. In mice, multi-day imaging experiments are achieved by implanting a cranial window following removal of part of the skull [36, 8]. Similar imaging preparations have been developed for flies [7, 31, 10]. However, because imaging window implantation requires a tedious surgery with low success rates, these methods are not commonly used.

Current developments in long wavelength three-photon microscopy overcome the limited penetration of two-photon imaging in mice [23, 38, 39, 9]. Three-photon microscopy not only improves the signal-to-background ratio by several orders of magnitude, but also enables the excitation of conventional fluorophores and fluorescent proteins using longer wavelengths [38]. Three-photon excitation at 1300 nm allowed the functional imaging of neurons labelled with a genetically encoded Ca^{2+} indicator GCaMP6 in the CA1 hippocampal region in an intact mouse brain [23, 9]. These results indicate that three-photon imaging at long wavelength spectral windows opens new opportunities for non-invasive recording of neuronal activity with high spatial and temporal resolution at depths previously inaccessible with optical imaging techniques, such as two-photon imaging. Recently, three-photon microscopy at 1700 nm excitation has shown promising results in imaging the fly brain through the cuticle

[34].

Here, we developed a non-invasive, chronic three-photon imaging preparation for flies to image neural structure and activity through the intact cuticle. Our method allows short term and chronic functional and structural imaging of the fly brain without any microsurgery. Using this method, we captured neural structures of mushroom body Kenyon cells and the central complex ring neurons with cellular resolution at 1320 nm and 1700 nm excitation. We also performed short term and chronic functional imaging of odour-evoked neural activity of Kenyon cell axons comprising the mushroom body γ-lobes using a genetically encoded Ca^{2+} indicator, GCaMP6s [3]. Kenyon cells are the primary intrinsic neurons in the insect mushroom body. Diverse subtypes of Kenyon cells (n=~2200) extend their axons along the pedunculus and in the dorsal and medial lobes [32, 5, 12]. These neurons receive and integrate information from heterogeneous sets of projection neurons which carry olfactory, gustatory, and visual sensory information [42, 24]. In our chronic three-photon functional imaging experiments, we found that odour responses in the mushroom body γ-lobes change with time; sharp odour evoked responses gradually transition to persistent neural activity which outlast the odour stimulus. Our three-photon imaging method thus enables measurements of neural activity over long time scales within an individual animal to capture changes in circuit function, which may reflect alterations in internal physiological state, familiarity/novelty to a sensory stimulus due to habituation or learning and/or alterations in neural activity during sleep-waking cycles. We expect that the methods presented here will significantly improve the current *in vivo* methods that are used for anatomical and functional imaging in fly neuroscience.

5.3 Results

5.3.1 Long-wavelength three-photon excitation allows non-invasive structural imaging of the fly brain

To develop a non-invasive imaging preparation using three-photon excitation, we first tested the transmission efficiency of long-wavelength lasers through the fly head cuticle. Previous experiments showed that the dorsal head cuticle of flies transmits light with an increasing efficiency at higher wavelengths [15]. To measure the transmission efficiency of a long wavelength lasers through the cuticle, we dissected the head cuticle, mounted it between two glass coverslips, and placed it in the beam path between the laser source and the photomultiplier tube (PMT). The transmission through the head cuticle was ~ 60% at 1300 nm and 1700 nm.

Next, we used a custom-built multiphoton microscope equipped with a wavelength-tuneable three-photon laser system to image the brain in head-fixed flies *in vivo* (Fig. 5.1a, Methods). We expressed membrane tagged GFP or RFP selectively in mushroom body Kenyon cells and imaged the fly brain through the cuticle (Fig. 5.2 and Fig. 5.3). Mushroom body Kenyon cells are a bilaterally symmetric group of neurons that are subdivided according to their axonal trajectories. The cell bodies of these neurons are located in the calyx (Fig. 5.2 b). Kenyon cell axons fasciculate into anatomically distinct structures called lobes, with dorsal lobes forming α and α' branches, and the medial lobes containing β, β', and γ branches [5, 12, 44]. Using three-photon microscopy with both 1320 nm and 1700 nm excitation, we were able to visualize different anatomical com-

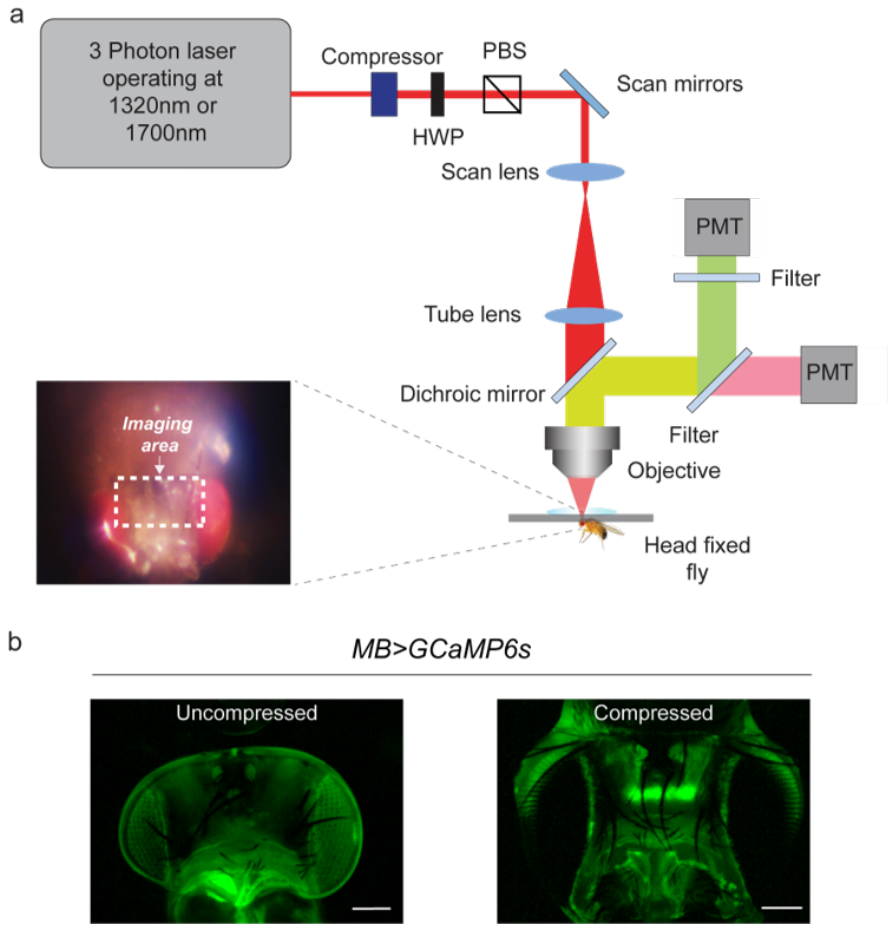

Figure 5.1: Three-photon scanning microscope system for imaging anatomical structures of the fly brain through the cuticle (a) Schematic of the three-photon microscope setup. Fly head is fixed to a cover slip and placed under the objective. The scan lens is a C-coated achromat for high transmission (97%) at 1700 nm, and the transmission of the tube lens is 82%. We use a custom high NA water immersion microscope objective (XL Plan N, Olympus, 25×1.05 NA), which is specially coated for high transmission (83%) at 1700 nm (HWP: half-wave plate, PBS: polarization beam splitter, PMT: photomultiplier tube). The imaging window on the fly head is shown in the picture in panel a (lower-left). (b) Uncompressed and compressed fly head visualized under a fluorescent dissecting microscope (scale bar = 100 µm). The same fly and lamp brightness were used to construct both images. The uncompressed and compressed head images are the average of 57 and 85 frames, respectively. Each averaged image was contrast enhanced (saturated pixels = 0.3%, histogram equalized) and de-noised (bright outliers removed with a pixel radius of 5 and a threshold of 5) using the ImageJ Remove Outliers function.

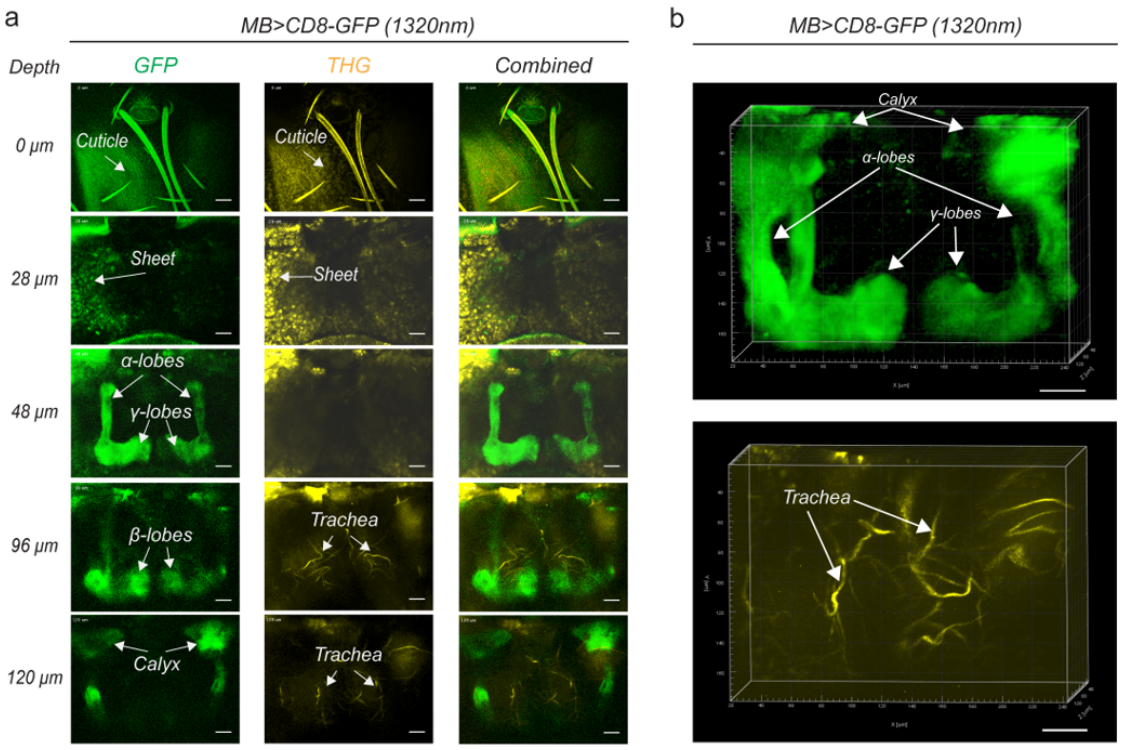

Figure 5.2: Three-photon structural imaging of the mushroom body through the cuticle with 1320 nm excitation. (a) Cross section images of the mushroom body (MB) lobes through the cuticle at 1320 nm (green). Third harmonic generation (THG) imaging visualizes the tracheal arbours (yellow). White arrows indicate different MB compartments that are identified. (b) 3D reconstruction of the z-stack images in Fig. 5.2a, GFP (upper panel), and THG (lower panel) (scale bars= 30 µm).

partments of the mushroom body. We acquired 120 µm stacks starting from the deepest structures we can detect and move to shallower areas in 1 µm depth increments and ended outside of the cuticle (Fig. 5.2 and Fig. 5.3). The calyx and axonal tracts along the peduncle were clearly visible as well as the dorsal and medial lobes containing $\alpha/\ \alpha'$ and β/β' and γ branches, respectively (Fig. 5.2 a and Fig. 5.3 a). We also measured the lateral brightness distribution of small features in the fluorescent and third harmonic generation (THG) signals, which sets an upper bound on the lateral resolution value. The full-widths at half-

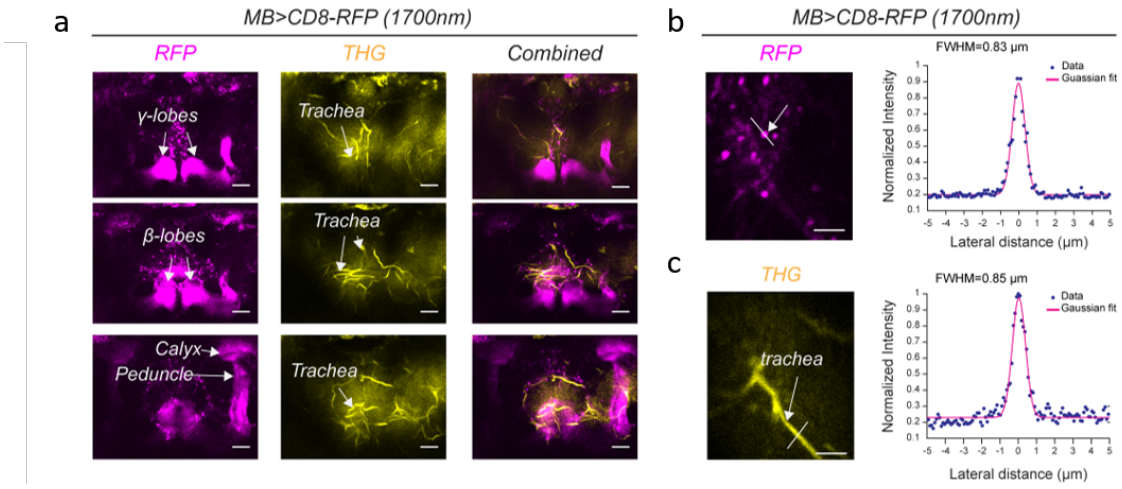

Figure 5.3: Three-photon structural imaging of the mushroom body through the cuticle with 1700 nm excitation. (a) Cross section images of the mushroom body (MB) lobes through the cuticle at 1700 nm excitation. Arrows indicate different MB compartments that are identified (scale bars= 25 µm). (b-c) The RFP and THG profiles of small features (magenta) and the surrounding trachea (yellow) with 1700 nm excitation. Lateral intensity profiles measured along the white lines are fitted by a Gaussian profile for the lateral resolution estimation (scale bars=10 µm).

maximum (FWHM) of the lateral brightness distributions are ~0.83 µm for the small features detected in the fluorescent signal at 1700 nm excitation (Fig. 5.3 a). In addition to the fluorescent signal, adipose, epithelial-like tissues, and tracheal branches surrounding the mushroom body lobes produced a bright THG signal (yellow) [1] (Fig. 5.2 a, and Fig. 5.3 a mid panel). The endothelium-like sheet covering the brain was most apparent right below the cuticle at 28 µm depth (Fig. 5.2a mid panel). We measured the lateral resolution of the THG signal using the smallest tracheal branches and found it to be ~0.85 µm, similar to the lateral resolution of the fluorescence image at 1700 nm excitation (Fig. 5.3 c).

Next, we imaged the central complex, another higher order processing centre, that is located in the dorsal and medial part of the fly brain (Fig. 5.4). The in-

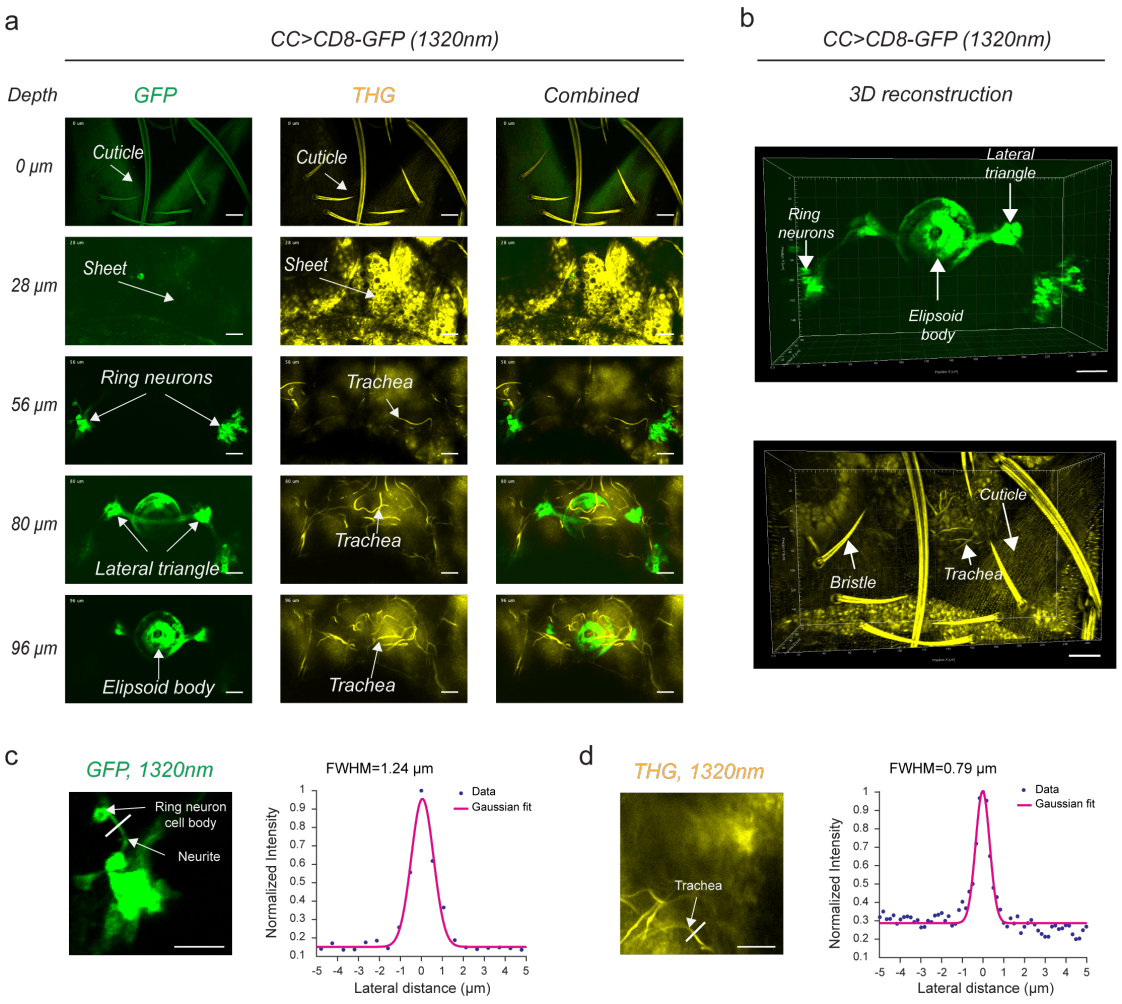

Figure 5.4: Three-photon structural imaging of the central complex through the cuticle with 1320 nm excitation. (a) Cross section imaging of the central complex (CC) ring neurons through the cuticle with 1320 nm excitation (green). Third harmonic generation (THG) imaging visualizes the tracheal arbours (yellow). Arrows indicate different CC compartments that are identified. (b) 3D reconstruction of the z stack images in Fig 5.4a, GFP (upper panel) and THG (lower panel) (scale bars= 30 µm). (c-d) The GFP and THG profiles of CC ring neurons (green) and the surrounding trachea (yellow). Lateral intensity profiles measured along the white lines are fitted by a Gaussian profile for the lateral resolution estimation (scale bars=20 µm).

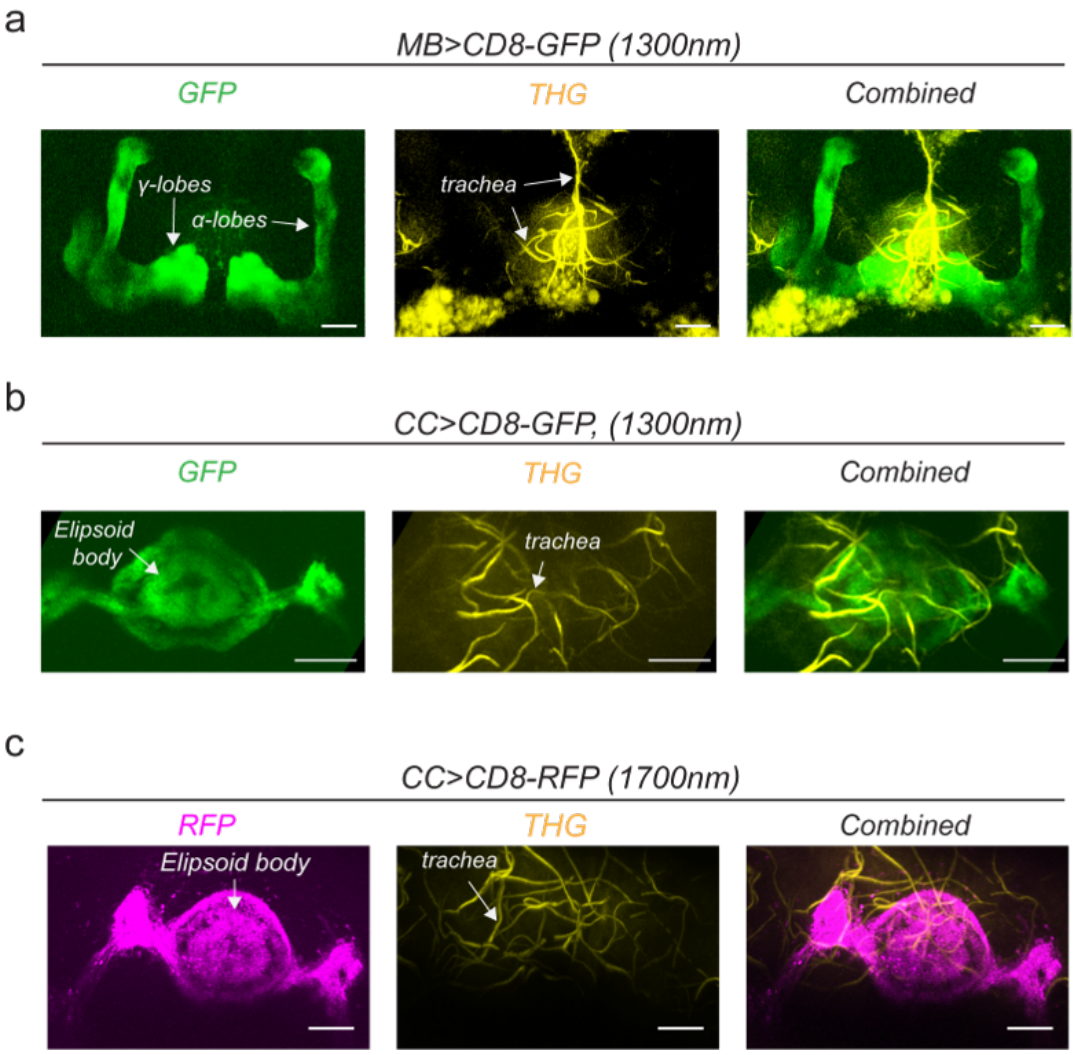

Figure 5.5: Three-photon structural imaging of the fly brain through the cuticle with 1320 nm and 1700 nm excitation. Cross section imaging of the fly brain through the cuticle at 1320 nm. (a) Mushroom Body (MB) lobes (green) and (b) Central Complex (CC) ring neurons (green) are imaged at different depths. Third harmonic generation (THG) imaging visualizes the tracheal arbours (yellow). Arrows indicate different MB and CC compartments that are identified with 3P imaging (scale bars= 25 µm). (c) Central Complex (CC) ring neurons expressing RFP are imaged with 1700 nm excitation (magenta). Third harmonic generation (THG) imaging visualizes the tracheal arbours (yellow). Arrows indicate different MB and CC compartments that are identified with the 3P imaging (scale bars= 25 µm).

sect central complex is a highly interconnected brain neuropil which processes sensory information and guides a diverse set of behavioural responses which include navigation, walking initiation, and turning direction [40, 25, 29]. It is composed of functionally distinct, but anatomically connected compartments: the protocerebral bridge, ellipsoid body, fan-shaped body, and the paired noduli [40]. The ellipsoid body consists of a group of neurons, the ring neurons, that extend their axons to the midline and form a ring-like structure that is composed of different layers [40, 25, 41]. Using a central complex specific promoter, we expressed membrane tagged GFP or RFP in the fly brain and imaged the ring neurons through the cuticle at 1320 nm and 1700 nm excitation (Fig. 5.4 a,b and Fig. 5.5 c). Ring neuron cell bodies, as well as the lateral triangle and the ellipsoid body layers, were clearly visible in both GFP and RFP fluorescent images (Fig. 5.4 a, b and Fig. 5.5 c). The FWHM of the lateral brightness distribution measured by a ring neuron's neurite cross section was ~1.24 µm for the fluorescent signal (Fig. 5.4 c) and ~0.79 µm for tracheal branches captured by the THG signal (Fig. 5.4 d). We also repeated our three-photon imaging experiments using a fibre laser-amplifier system with an integrated infrared optical parametric amplifier (OPA, KM Labs). The results are comparable to what we obtained previously (Fig. 5.5 a,b and Methods), indicating that a more compact, less powerful source is adequate for imaging fly brain structures with three-photon microscopy. Our results demonstrate that non-invasive three-photon microscopy is able to capture single neurons and fine anatomical structures within the mushroom body and central complex at resolutions comparable to the open cuticle preparations using two-photon microscopy [37].

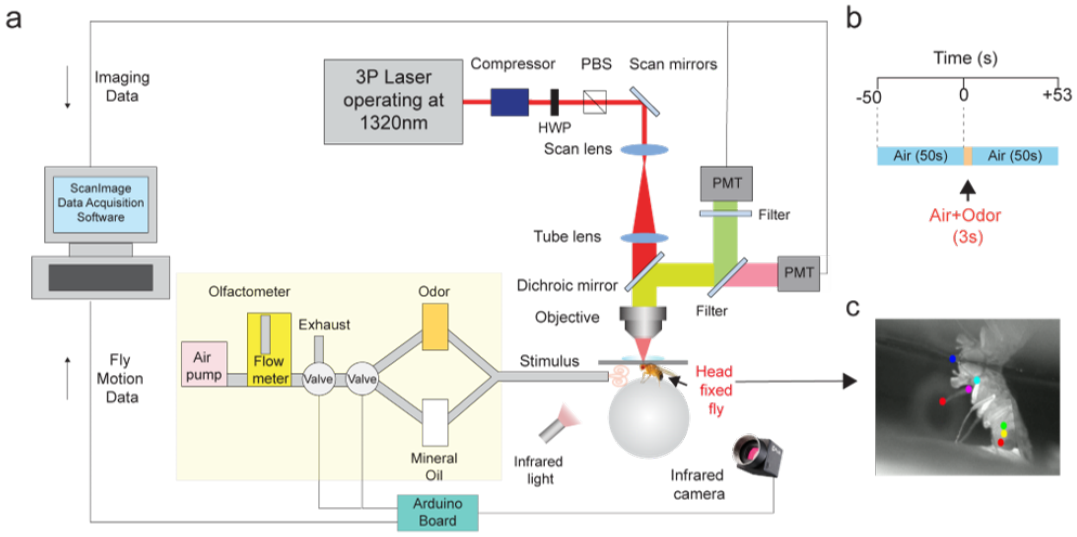

Figure 5.6: Three-photon functional imaging of odour-evoked responses of the mushroom body Kenyon cells. (a) Schematic of the custom made olfactometer. This olfactometer is used to puff odours to the fly that is placed on a water-immersed ball for functional Ca^{2+} imaging using GCaMP6s. An Arduino board synchronizes the FLIR Black Fly S Camera to capture fly behaviour. ScanImage software is used to control PMTs and to capture images at 2.13 Hz at 512x256 resolution. (b) Stimulus timeline. Flies were stimulated with air (50s), before and after the odour stimulus (3s). Each trial lasted 103s. Flies were stimulated 5 times using the same odour stimulus scheme. (c) Picture of the head fixed fly on the ball under the three-photon microscope. The coloured dots show the body parts that were tracked and used to train the DeepLabCut neural network.

5.3.2 Three-photon imaging at 1320 nm allows functional imaging of odour-evoked responses of mushroom body Kenyon cells through the head cuticle

We next tested the applicability of three-photon microscopy to capturing neural activity in the fly brain through the intact cuticle. In these experiments, a custom odour delivery and behaviour system were used, where flies were head

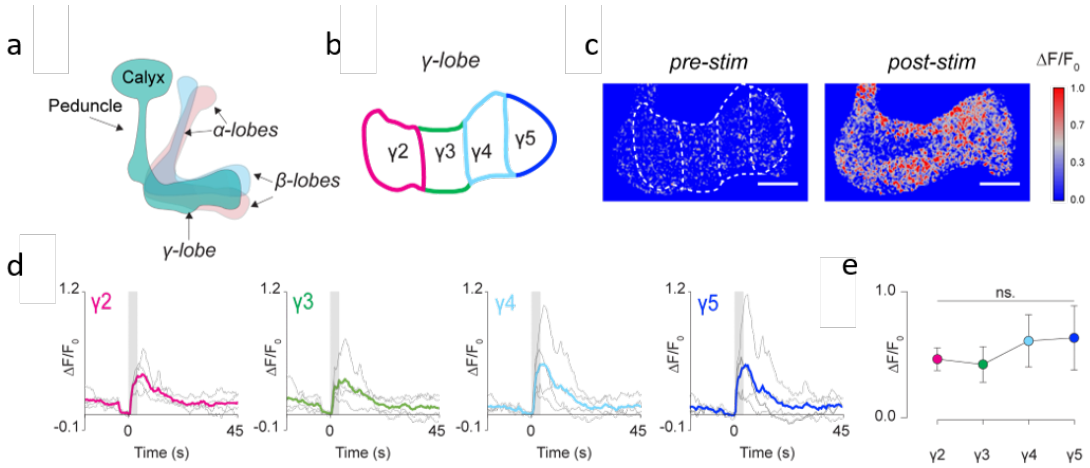

Figure 5.7: Three-photon functional imaging of odour-evoked responses of the mushroom body Kenyon cells. (a) Schematic of the mushroom body anatomy indicating the location of α, β and γ lobes (b) γ lobes have discrete anatomical compartments (shown for γ2-γ5). (c) GCaMP6s is expressed in Kenyon cells using a *Mef*2-promoter. Normalized ($\Delta F_{max}/F_0$) GCaMP6s signal is shown before (left) and after (right) odour stimulus. (d) Quantification of the normalized ($\Delta F_{max}/F_0$) GCaMP6s signal over time in each discrete γ-lobe compartment. Grey bar indicates when the odour stimulus is present (scale bar= 20 µm). (e) Peak normalized ($\Delta F_{max}/F_0$) GCaMP6s signal in each discrete γ-lobe compartment. One-way ANOVA followed by Tukey's multiple comparison tests, ns = not significant.

fixed but otherwise free to move on a polymer ball under the three-photon microscope (Fig. 5.6 a). We expressed GCaMP6s selectively in Kenyon cells and stimulated the fly olfactory sensory organ, the antenna, with the food odour, apple cider vinegar (Fig. 5.6 b). Using a three-photon scanning microscope at 1320 nm excitation, odour evoked Ca^{2+} responses of mushroom body γ-lobes (Fig. 5.7 c) were captured at 512x256 pixel resolution and 2.13 Hz frame rate through the head cuticle. A brief 3s odour stimulus triggered a robust fluorescence increase in Kenyon cell axons comprising the mushroom body γ-lobes (Fig. 5.7 d). Kenyon cell axons are innervated by distinct subsets of dopaminergic neurons, which carry positive and negative contextual information to the

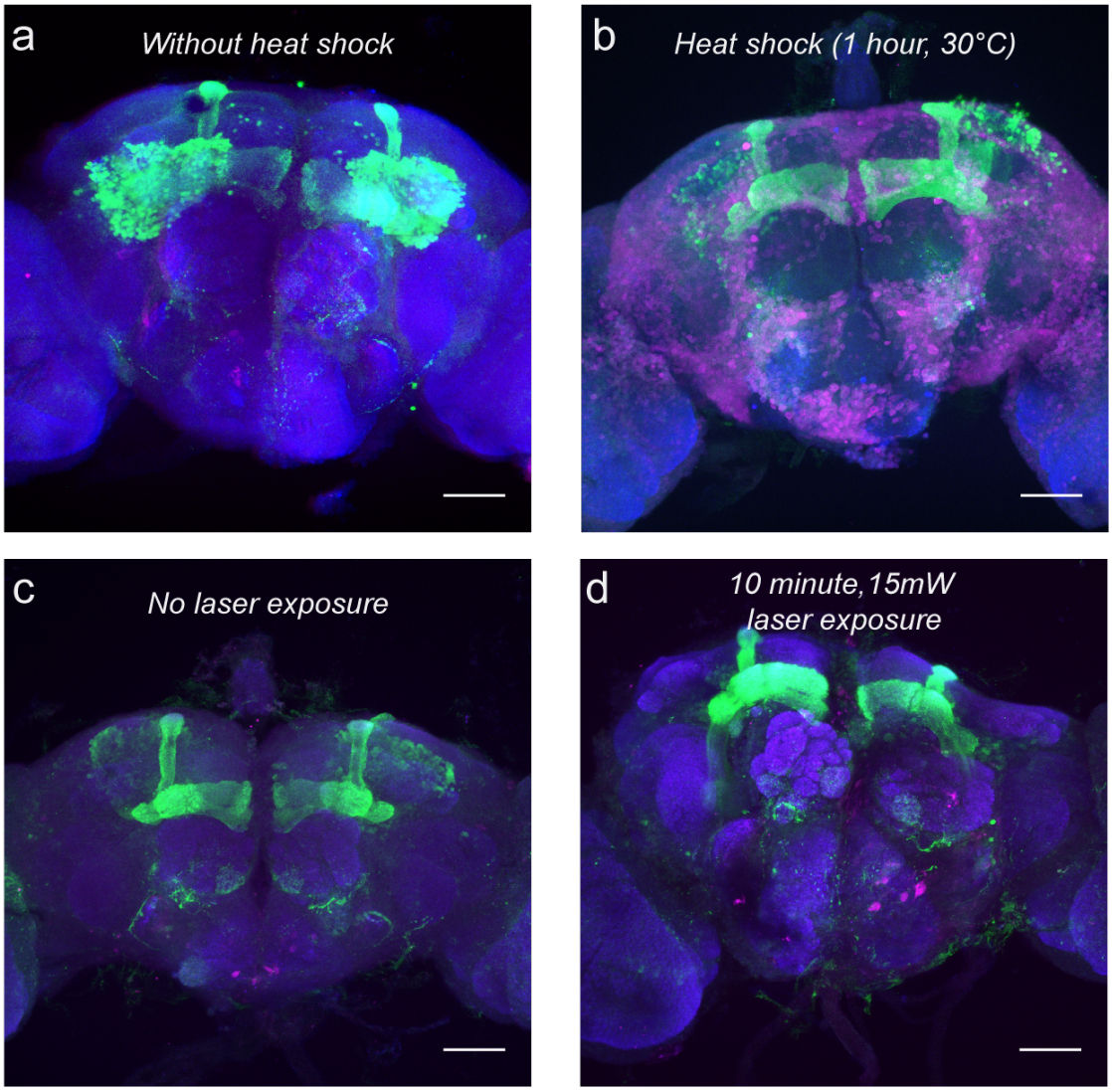

Figure 5.8: HSP70 staining of fly brains to investigate heat induced stress response after three-photon with 1320 excitation. (a) Negative control and (b) positive control for HSP70 staining. (a) Without heat shock there is minimal HSP70 protein expressed in the fly brain. (b) When flies are exposed to heat (30°C) for 1 hours, HSP70 protein level are significantly elevated across the brain. (c-d) HSP70 protein levels in brain without (c) and with (d) 1320nm laser exposure. There is no obvious change in HSP70 protein levels after three-photon imaging (scale bars= 50 µm).

mushroom body depending on a fly's previous experiences. Based on dopaminergic innervation, γ-lobes can be subdivided into five anatomical compartments [4]. To determine whether the localized dopaminergic input along the Kenyon cell axons resulted in differential olfactory responses in the γ-lobes, we calculated the normalized peak fluorescent signal in each compartment of the γ-lobes. We found no differential responses in peak $\Delta F_{max}/F_0$ amplitude to food odour across different compartments (Fig. 5.7 d,e). These results suggested that three-photon microscopy with 1320 nm excitation is effective in capturing odour evoked Ca^{2+} responses in the mushroom body neurons through the intact head cuticle, and achieves temporal and spatial resolutions comparable to two-photon microscopy. We also carried out immunostaining of fly brains and checked for stress responses to laser exposure at 1320 nm three-photon excitation using a HSP70 antibody as a marker for heat-induced responses in glial cells and neurons [26, 16]. Our results showed that there was no obvious tissue damage and heat-stress response under the imaging conditions used for activity recording in this study (Fig. 5.8).

5.3.3 Three-photon imaging of neural activity captures changes in odour evoked responses of Kenyon cells over long-time scales

Studying how neural circuits change activity during learning or in alternating behavioural states requires non-invasive chronic imaging methods that permit recording neural activity over long time scales. Leveraging the non-invasive nature of our preparation, we pushed the limits of functional imaging of the

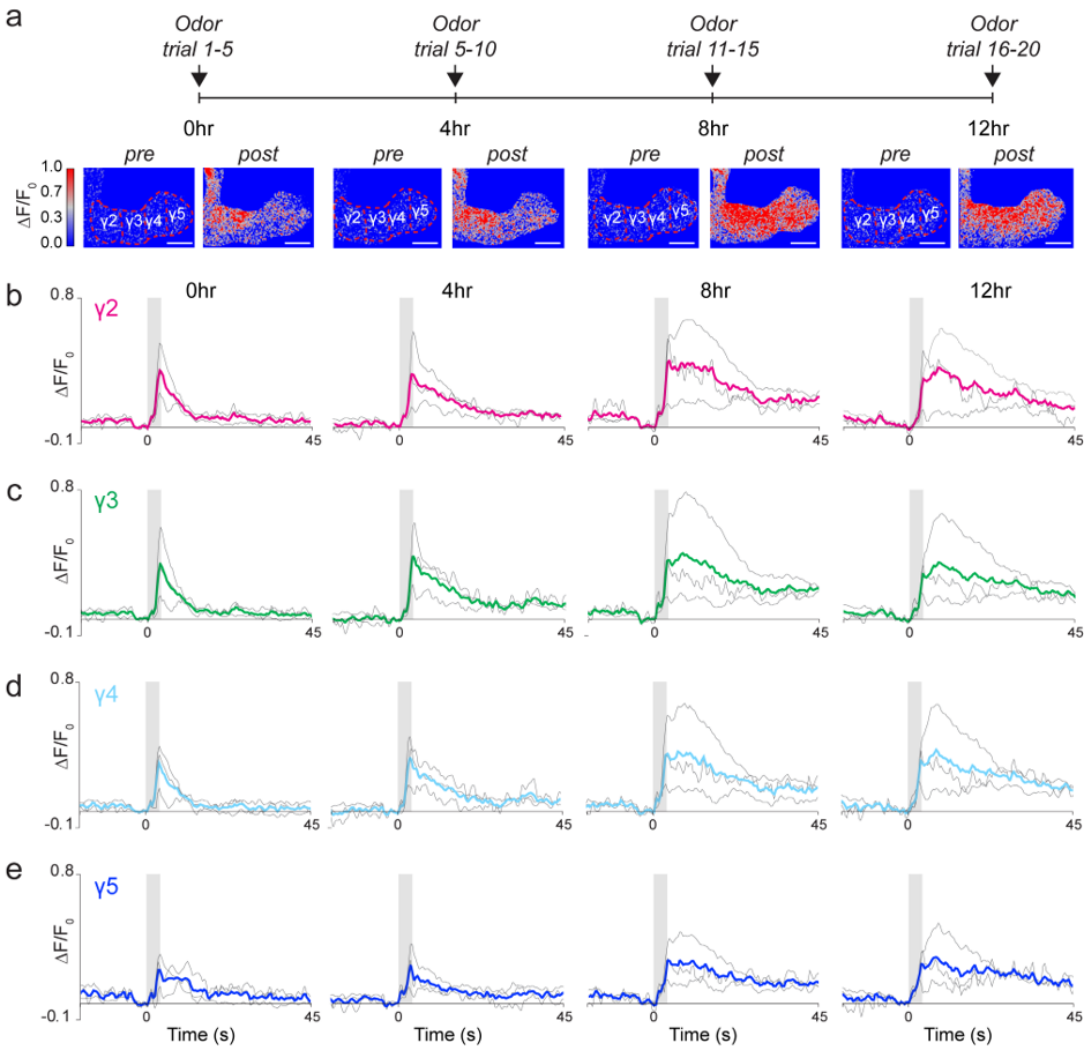

Figure 5.9: Chronic three-photon imaging of odour-evoked responses of the mushroom body Kenyon cells (a) Stimulus timeline for chronic odour imaging. GCaMP6s signal is captured from Kenyon cells axons innervating mushroom body γ-lobes. Normalized $\Delta F_{max}/F_0$ signal is shown before (left) and after (right) the odour stimulus (scale bar= 20 µm). (b-e) Quantification of the normalized $\Delta F_{max}/F_0$ signal over time in each γ-lobe compartment. Each lobe's response is colour coded differently. Grey bar indicates when the odour stimulus is present. Each grey line indicates the average response of a fly over multiple trials in a given hour. The average response of 3 flies is shown with a particular colour for each compartment.

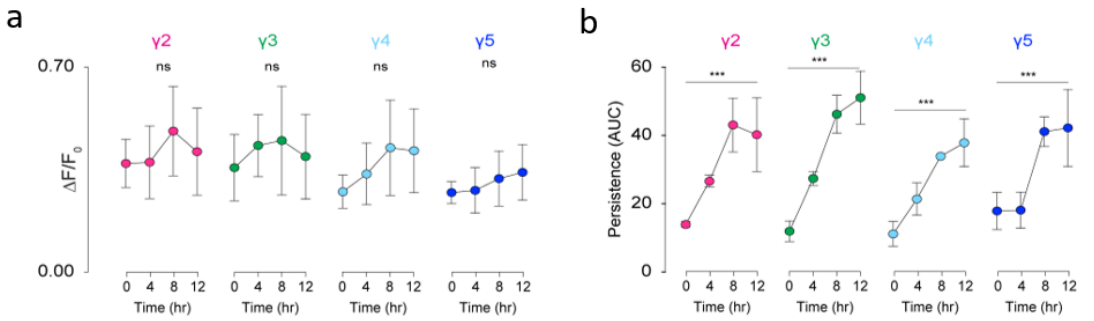

Figure 5.10: Chronic three-photon imaging of odour-evoked responses of the mushroom body Kenyon cells (a) Quantification of the peak amplitude ($\Delta F_{max}/F_0$). (b) Area under the curve (AUC) after the odour stimulus for each compartment of the γ-lobes (Two-way repeated measures ANOVA. Data are presented as mean ± SEM, ns= not significant, ***=p<0.001, n=3 flies, 3-5 trials per time point).

fly brain in response to odour stimulation to longer time scales (12 hrs). Using our custom odour delivery system, we stimulated the fly antenna with apple cider vinegar in ~10 minute imaging sessions every four hours and captured how odour responses change over time as the fly was food and water deprived (Fig. 5.9 a). During these experiments, we captured the fly's behaviour in parallel with the odour stimulation to assure that the fly stayed alive (Fig. 5.11). To determine the absolute signal level during chronic imaging, we first calculated the photon counts for representative trials at each time point from the mushroom body γ2 compartment. The photon counts per pixel per second had magnitudes above baseline similar to previously reported levels for three-photon excitation of GCaMP6 protein in the mouse brain [23, 39] (Fig. 5.12). Next, for each time point, we calculated the normalized peak fluorescent signal and the area under the normalized fluorescence curve, as metrics representing the odour response strength and persistence during chronic imaging, respectively (Fig. 5.9b-e). Our analysis shows that the peak response to food odour did not change

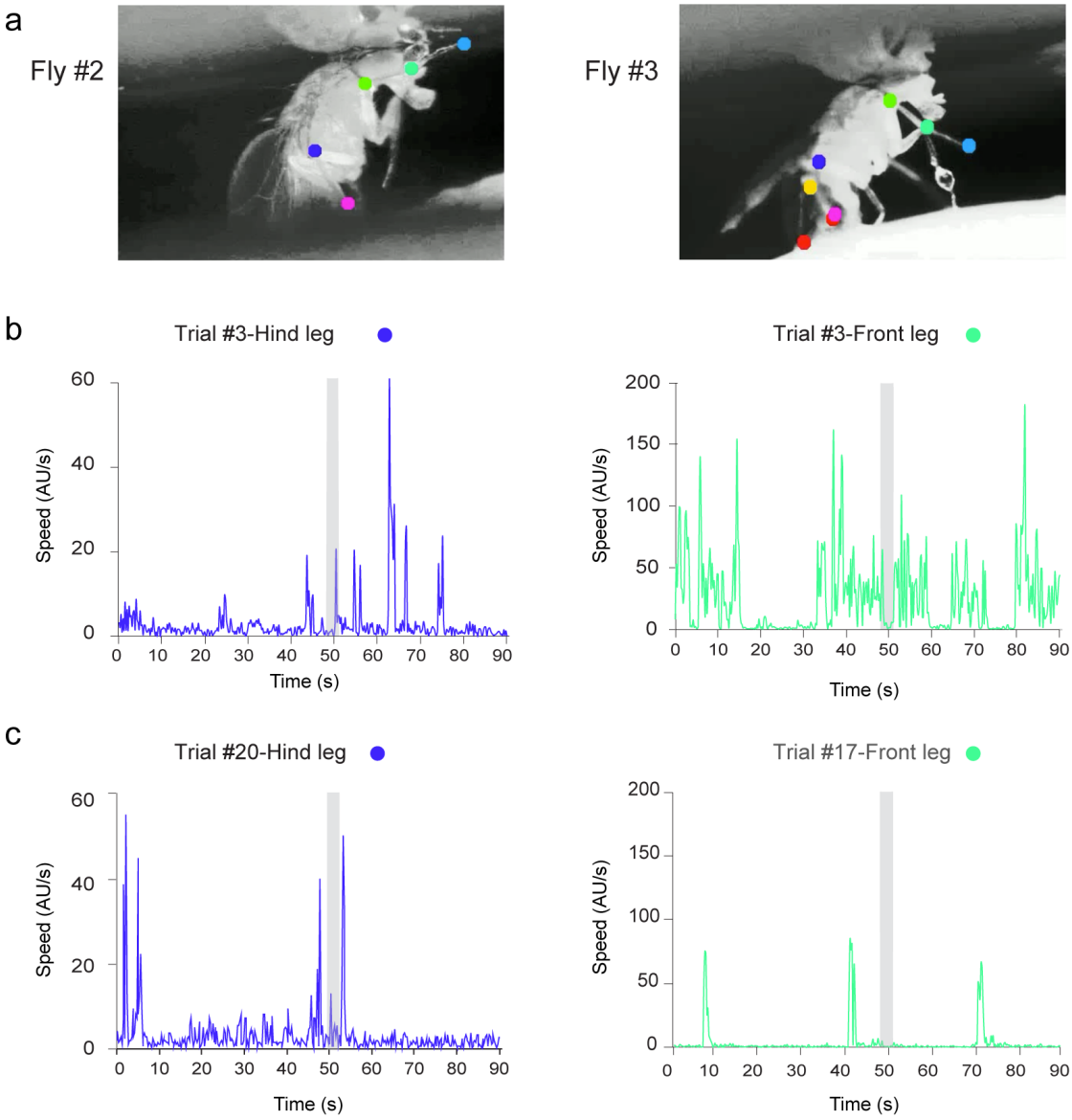

Figure 5.11: Fly motion traces during chronic imaging. (a) Picture of the head fixed fly on the polymer ball under the three-photon microscope. The coloured dots show the body parts that were tracked and used to train the DeepLabCut neural network. (b-c) The speed of indicated legs during the odour stimulus trials. Grey bar indicates when the stimulus is present. Speed is calculated as arbitrary units per second (AU/s).

with food and water deprivation in any of the γ-lobe compartments (Fig. 5.10 a). However, the persistence of the odour evoked Ca^{2+} response in all of the γ-lobe compartments increased as the experiment progressed (Fig. 5.10 b). We especially noticed a change 4 hours after the first odour trial, which may reflect a critical state change in the nervous system in response to repeated odour stimulation, food and water deprivation, or association between the stimulus and the animal's internal physiological or arousal state. Flies continued to show robust calcium activity for at least 4 hours after the change in dynamics, and our behavioural data suggest that the fly is active throughout the experiment. These results demonstrate that three-photon non-invasive imaging of the fly brain allows recording of neural activity within an individual fly over long-time scales, which was previously not possible with open-cuticle preparations.

5.4 Discussion

Plasticity in neural states and the ability to learn and remember relevant information are hallmarks of nervous systems, and allow animals to adapt and respond to dynamic environments. Investigating how neural states, learning, and memory are encoded in neural circuits requires tracking the activity of neurons over long time scales up to many hours. The three-photon imaging method developed here significantly extends the time frame of current *in vivo* imaging preparations used for anatomical and functional studies in fly neuroscience. Non-invasive chronic imaging of the fly brain will allow us to capture the activity of neural populations in changing behavioural states; facilitate decoding of neural plasticity during memory formation; and permit observation of changes in brain structures during development and aging. Our first biological applica-

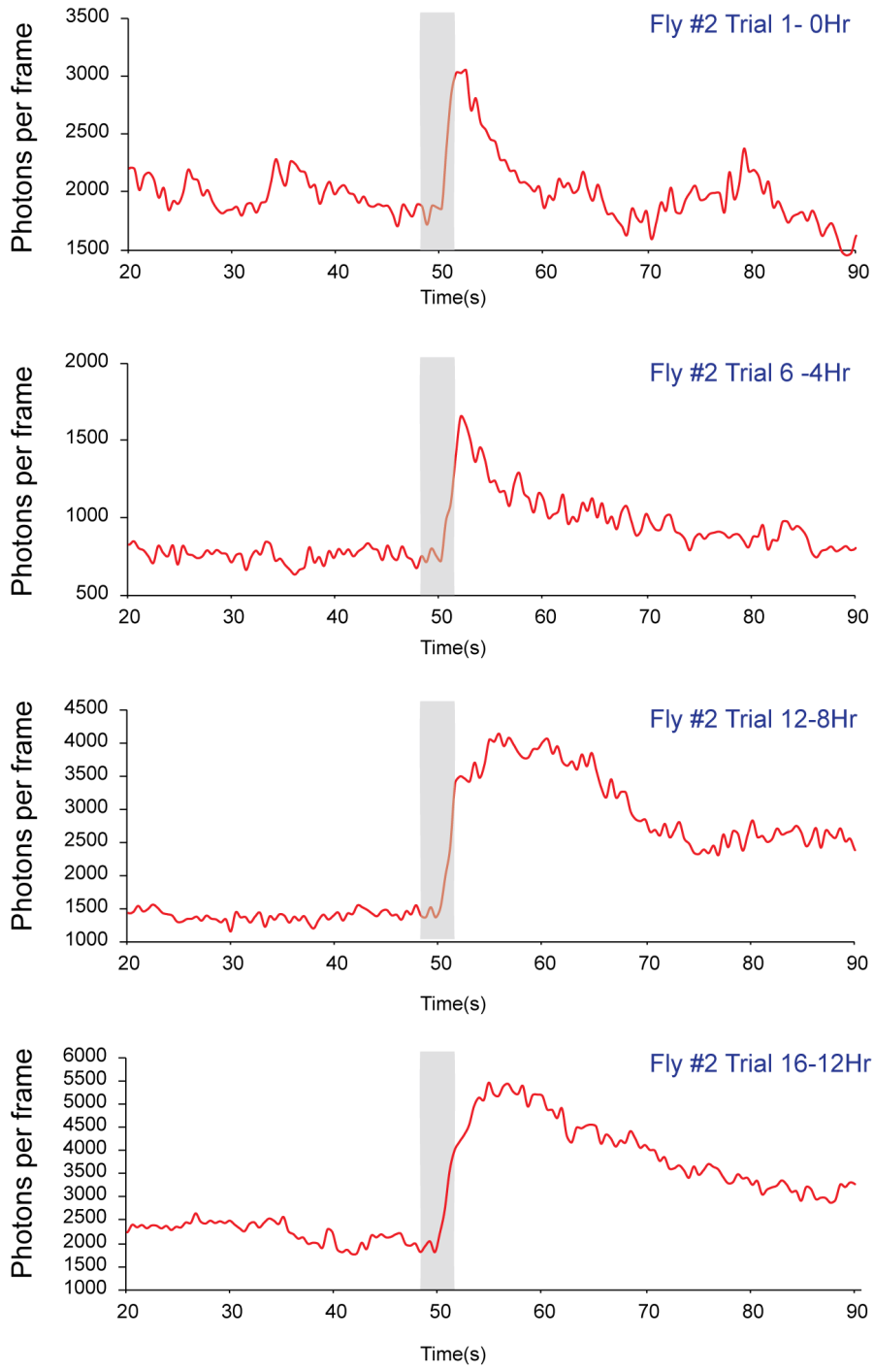

Figure 5.12: Three-photon imaging of odour-evoked neural activity in GCaMP6s-labeled Kenyon cells forming mushroom body γ-lobes. Average power of ~20 mW at 1 MHz repetition rate was used for imaging. The four plots show the activity of the γ2-compartment in fly#2 in a single trial across different time points. The fluorescence intensity is converted to photon counts per frame in the selected ROI.

tion of *in vivo* three-photon microscopy captures interesting initial observations of how odour responses evolve in Kenyon cells comprising mushroom body γ-lobes, after repeated exposure to a food odour, apple cider vinegar. Our results suggest that sharp odour evoked responses gradually transition to persistent neural activity. We hypothesize that these changes in odour-evoked activity of Kenyon cells might reflect internal physiological or arousal state changes driven by food/water deprivation or sleep-waking cycles during chronic imaging, or alternatively, changes in the novelty of the food odour with repeated application during the experiments. Further experiments will aim to understand the origins of persistent neural activity and the molecular mechanisms that mediate it. While our focus here is to develop chronic *in vivo* three-photon imaging methods for fly neuroscience research, we anticipate that there will be a wide variety of uses for this technology in other insect models including mosquitoes, honey bees, and ants in the near future.

5.5 Methods

5.5.1 Fly stocks

Flies were maintained on conventional cornmeal-agar-molasses medium at 23-25°C and 60-70% relative humidity, under a 12hr light: 12hr dark cycle (lights on at 9 A.M.). Fly strains and sources: Mef2–GAL4.247 (Bloomington # 50742); GMR15B07-GAL4 (Bloomington # 48678), 10XUAS-IVS-mCD8::GFP (Bloomington # 32186); 10XUAS-IVS-mCD8::RFP (Bloomington # 32219); 20XUAS-IVS-GCaMP6s (Bloomington # 42746).

5.5.2 Fly *in vivo* imaging preparation.

All animals used for imaging experiments were male flies with indicated genotypes kept in 25°C incubators ad libitum. Flies used for chronic functional experiments were 2-7 days old, and flies used for short term functional experiments were 1-4 days old. To perform intact brain imaging, flies were first temporarily head-fixed in a fly holder. A drop of UV curable resin (Liquid plastic welder, Bondic) was applied to the head and thorax, which was then cured with blue light (~470 nm) and fused to a cover glass. Lightly pressing the head against the glass with forceps during the curing process typically improved image quality (Fig. 5.1 b). Fly proboscises were immobilized with blue light curable resin to minimize head motion caused by muscle contractions. For short term imaging, flies were food deprived for 16-24 hours in vials with a wet Kim wipe. Flies used in long term functional imaging experiments were fed 100 mM sucrose just before the first trial to assure that the flies were in a fed state.

5.5.3 Immunohistochemistry for tissue damage assessment.

To investigate laser-induced stress in the brain during three-photon imaging through the intact head cuticle, 1-2-day old male homozygous MB>GCaMP6s flies were imaged continually at 1320 nm for 10 minutes. The laser was focused 70 µm below the cuticle with ~15 mW average power. Flies were head compressed and fed 100 mM sucrose before imaging to reproduce actual experimental conditions. A control group was prepared under the same conditions, but was not exposed to laser excitation. Laser exposed and control brains were dissected approximately 2 hours after mounting. To test HSP70 antibody effi-

cacy on fly brains, a positive control group of flies were first exposed to 30°C for 1 hour in a shaking incubator to induce HSP70 expression. These flies were then dissected along with a negative control group of flies that were kept at room temperature for 1 hour. For whole mount staining, brains were dissected in phosphate-buffered saline (PBS) and incubated in 4% paraformaldehyde (PFA) in PBS for 20-30 minutes at room temperature on an orbital shaker. Tissues were washed 3-4 times over 1 hour in PBS (calcium- and magnesium-free; Lonza BioWhittaker #17-517Q) containing 0.1% Triton X-100 (PBT) at room temperature. Samples were blocked in 5% Normal Goat Serum in PBT (NGS-PBT) for 1 hour and then incubated with primary antibodies diluted in NGS-PBT for 24 hours at 4°C. Primary antibodies used were anti-GFP (Torrey Pines, TP40, rabbit polyclonal, 1:1000), anti-Brp (DSHB, nc82, mouse monoclonal, 1:20), and anti-HSP70 (Sigma, SAB5200204, rat monoclonal, 1:200). The next day, samples were washed 5-6 times over 2 hours in PBT at room temperature and incubated with secondary antibodies (Invitrogen) diluted in NGS-PBT for 24 hours at 4°C. On the third day, samples were washed 4-6 times over 2 hours in PBT at room temperature and mounted with VECTASHIELD Mounting Media (Vector Labs, Burlingame, CA, USA) using glass slides between two bridge glass coverslips. The samples were covered by a glass coverslip on top and sealed using clear nail polish. Images were acquired at 1024x1024 pixel resolution at ~1.7 µm intervals using an upright Zeiss LSM 880 laser scanning confocal microscope and Zeiss digital image processing software ZEN. Maximum projection images of Z-stacks were generated in the ZEN image-processing software. The power, pinhole size and gain values were kept the same for all imaged brains during confocal microscopy.

5.5.4 Odour delivery.

Food odour, apple cider vinegar, was delivered using a custom built olfactometer as described previously [27]. Clean room air was pumped (Active Aqua Air Pump, 4 Outlets, 6W, 15 L/min) into the olfactometer, and the flow rate was regulated by a mass flow controller (MC Standard Series Mass Flow Controller, Alicat Scientific). Two Arduino controlled 3-way solenoid valves (3-Way Ported Style with Circuit Board Mounts, LFAA0503110H) controlled air flow. One valve delivered the odorized airstream either to an exhaust outlet or to the main air channel, while another valve directed air flow either to the stimulus or control channel. The stimulus channel contained a 50 ml glass vial containing undiluted apple cider vinegar (volume=10 ml) (Wegmans), while the control channel contained a 50 ml glass vial containing mineral oil (volume=10 ml). For odour stimulation experiments, flies were placed approximately 1 cm from a clear PVC output tube (OD = 1.3 mm, ID = 0.84 mm), which passed a 1 L/min air stream to the antennae. The odour stimulus latency was calibrated before the experiments using a photo ionization detector (PID) (Aurora Scientific). We sampled odour delivery using the PID every 20 ms and found average latency to peak odour amplitude was < 100 ms across 34 measurements. Each odour stimulation trial consisted of 50 seconds of clean mineral oil, 3 seconds of undiluted apple cider vinegar stimulus, and another 50 seconds of mineral oil. Between trials, scanning was stopped for 20 seconds to minimize the risk of imaging-induced tissue stress. Five trials were performed sequentially, and for chronically imaged flies, the five-trial block was repeated every four hours. Between trial blocks, scanning was stopped, and air passing through the stimulation tube was redirected to the exhaust valve to prevent desiccation. To further prevent desiccation, flies were placed on a water-absorbing polymer bead. Fly

behaviour was videotaped from the side to capture any movement by a CCD camera (FLIR, Blackfly S, BFS-U3-13Y3M-C) equipped with a 1.5-megapixel macro lens (Computar, COM MLM3X-MP, 3X Macro Zoom). We captured fly behaviour with videos at 4.3 Hz speed using the Spinnaker SDK (Flor) image acquisition software under IR light illumination.

5.5.5 Three-photon microscopes and laser sources.

Excitation source (Figure 5.2- 5.6 and Figure 5.5c): The excitation source is a wavelength-tuneable optical parametric amplifier (OPA, Opera-F, Coherent) pumped by a femtosecond laser with a MOPA (Master Oscillator Power Amplifier) architecture (Monaco, Coherent). A prism pair (10SF10, Newport) and a silicon wafer are used to compensate for the dispersion of the optics of the light source and the microscope including the objective, for 1320 nm and 1700 nm, respectively. The laser repetition rate is maintained at 1 MHz for both structure imaging and activity imaging.

Imaging setup (Figure 5.2- 5.6 and Figure 5.5c): The images were acquired with a custom-built multiphoton microscope. The scan lens is a C-coated achromat (AC254-030-C-ML, Thorlabs) for high transmission at 1700 nm and at 1320nm, and the transmission of the tube lens (Sutter Instrument) is 82%. For imaging experiments that use RFP, we used a custom high numerical aperture (NA) water immersion microscope objective (Olympus XLPLN25XWMP2, 25X, NA 1.05), which is specially coated for high transmission (83%) at 1700 nm. For imaging experiments that use GFP and GCaMP6s, we used a custom high numerical aperture (NA) water immersion microscope objective (Olym-

pus XLPLN25XWMP2, 25X, NA 1.05), which is specially coated for high transmission (~ 70%) at 1320 nm. 2 detection channels were used to collect the fluorescence signal and the third harmonic generation (THG) signal by photomultiplier tubes (PMT) with GaAsP photocathode (H7422-40, Hamamatsu). For GFP and GCaMP6s imaging at 1320 nm, fluorescence signal and THG signal were selected by a 520/60 nm band-pass filter (FF01-520/60-25, Semrock) and a 435/40 nm band-pass filter (FF02-435/40-25, Semrock), respectively. For RFP imaging at 1700 nm, we used a 593 nm long-pass filter (FF01-593/LP-25, Semrock) for fluorescence and a band-pass 562/40 nm filter (FF562/40-25, Semrock) for THG collection. For signal sampling, the PMT current is converted to voltage and low-pass-filtered (200 kHz) by a transimpedance amplifier (C7319, Hamamatsu). Analog-to-digital conversion is performed by a data acquisition card (NI PCI- 6110, National Instruments). The signal acquisition system displayed shot-noise limited performance, and light shielding was carefully done to achieve dark counts of 20-40 photons per second under actual imaging conditions without laser scanning. ScanImage 5.4 (Vidrio Technologies) running on MATLAB (MathWorks) was used to acquire images and control a 3D translation stage to move the sample (MP-285, Sutter Instrument Company). All imaging depths and thickness are reported in raw axial movement of the motorized stage, unless otherwise stated.

Excitation source (Figure 5.5a, 5.5b): The laser used as the excitation source for three-photon microscopy (3PM) is an optical parametric amplifier (OPA, KM Labs), pumped by the KM Labs Y-Fi^{TM}HP. A two-prism glass compressor (SF 10 glass) is used to compensate for the normal dispersion of the optics of the light source and the microscope. The Y-Fi^{TM} OPA has an operating wavelength centred at 1300 nm and output an average power of ~ 400 mW (~ 0.4 µJ at 1 MHz

repetition rate). Pulse duration is less than 150 fs. Power control of the laser was achieved using a half wave plate (HWP) (Thorlabs) and a polarizing beam splitter cube (PBS) (Thorlabs) and ScanImage module for MATLAB (Mathworks).

Imaging setup (Figure 5.5a, 5.5b): Images were acquired using a custom-built multiphoton microscope with a pair of galvanometric scanners (Cambridge Technology). The objective used was a high numerical aperture water immersion objective (Olympus XLPLN25XWMP2, 25X, NA 1.05). Signal from specimens was collected through the objective and then reflected by multiple dichroic beam splitters. (FF01-520-Di02- 25 x 36, Semrock, and FF484-Di01-25 x 36, Semrock) to the detectors. The two-channel detection system consists of a green fluorescence signal and third harmonic generation (THG). ScanImage was used to control the ILS100CC motorized translation stage from (Newport). High-resolution structural images were typically taken with 512x512 pixels/frame, 0.24 Hz frame rate, and multiple frame averages at each depth. Photon counting: To show the absolute signal strength in the unit of photon count rate, pixel values are multiplied by a calibration factor, which is obtained by taking the ratio of the photon count rate with a photon counter (SR400, Stanford Research Systems) and the average pixel value, simultaneously recorded on a uniform fluorescein sample.

5.5.6 Data analysis

Resolution measurements: We measured the lateral brightness distribution of small features within both the GFP and RFP labelled fly brains, which sets an upper bound on the lateral resolution value. Lateral intensity profiles measured

along the white lines (Fig. 5.3 b,c and Fig. 5.4 c,d) were fitted by a Gaussian profile for the estimation of the lateral resolution. Image processing for structural imaging. TIFF stacks containing fluorescence data were converted to 8 bits. When necessary, stacks were registered using the TurboReg plugin in ImageJ. Images shown in Fig. 5.2- 5.4 are an average of 3 z-stacks spanning 3 microns. 3D reconstructions of the z-stacks were generated using the Imaris v9.2, Bitplane Inc., software available at http://bitplane.com. Images shown in Fig. 5.5 are an average of 15 z-stacks spanning 15 microns.

Image processing for activity recordings. TIFF stacks containing fluorescence data were converted to 32 bits, and pixel values were left unscaled. When necessary, stacks were registered using the TurboReg plugin in ImageJ. To compute $\Delta F_{max}/F_0$ traces, γ-lobe ROIs were first manually selected using a custom Python script. A Gaussian filter with pixel radius of 1 was applied to each frame. F_0 was computed as the average of 10 frames preceding stimulus onset. The F_0 image was then subtracted from each frame, and the resulting image was divided by F_0. The resulting trace was then low-pass filtered by a moving mean filter with a window size of 3 frames. Data were analysed using Python (code available upon request) and plotted in Microsoft Excel. Peak $\Delta F_{max}/F_0$ was determined by the peak value within 20 frames after odour delivery. We measured the persistence as the total area under the normalized curve after the peak $\Delta F_{max}/F_0$ value. To prevent underestimating persistence as a result of negative values in the $\Delta F_{max}/F_0$ trace, values that followed a zero-crossing were set to zero. Averaged traces were manually inspected for each lobe and trial block, and rejected if peak $\Delta F_{max}/F_0$ was lower than the noise detected in the entire trial. These traces had lower than 0.1 peak $\Delta F_{max}/F_0$ value. These accounted for less than 15% of the total trials in three flies tested for chronic imaging.

Fly movement analysis: Fly motion traces were obtained using the DeepLabCut tracking program [19]. To train the network, we manually annotated movement in the fly bodies and legs for 340 frames across multiple cropped and contrast-enhanced videos. The data shown in Figure 5.11 show the activity of front tarsi or hind legs.

5.5.7 Statistical analysis

All statistical analyses were performed using Prism V8.0.1 (GraphPad). Data collected in functional imaging experiments are shown as mean ± SEM. Details of statistical methods are reported in the figure legends. Statistical significance in chronic imaging across time points and in different mushroom body compartments were determined with a two-way repeated measures ANOVA.

Bibliography

[1] Y. Barad, H. Eisenberg, M. Horowitz, and Y. Silberberg. Nonlinear scanning laser microscopy by third harmonic generation. 70(8):922–924.

[2] Andrew B. Barron, Kevin N. Gurney, Lianne F. S. Meah, Eleni Vasilaki, and James A. R. Marshall. Decision-making and action selection in insects: inspiration from vertebrate-based theories. 9.

[3] Tsai-Wen Chen, Trevor J. Wardill, Yi Sun, Stefan R. Pulver, Sabine L. Renninger, Amy Baohan, Eric R. Schreiter, Rex A. Kerr, Michael B. Orger, Vivek Jayaraman, Loren L. Looger, Karel Svoboda, and Douglas S. Kim.

Ultrasensitive fluorescent proteins for imaging neuronal activity. *Nature*, 499(7458):295–300, July 2013.

[4] Raphael Cohn, Ianessa Morantte, and Vanessa Ruta. Coordinated and compartmentalized neuromodulation shapes sensory processing in drosophila. 163(7):1742–1755.

[5] Jill R. Crittenden, Efthimios M.C. Skoulakis, Kyung-An Han, Daniel Kalderon, and Ronald L. Davis. Tripartite mushroom body architecture revealed by antigenic markers. 5(1):38–51.

[6] Barry J. Dickson. Wired for sex: The neurobiology of drosophila mating decisions. 322(5903):904–909.

[7] Dhruv Grover, Takeo Katsuki, and Ralph J. Greenspan. Flyception: imaging brain activity in freely walking fruit flies. 13(7):569–572.

[8] Jasmin K. Hefendehl, David Milford, Daniel Eicke, Bettina M. Wegenast-Braun, Michael E. Calhoun, Stefan A. Grathwohl, Mathias Jucker, and Christian Liebig. Repeatable target localization for long-term in vivo imaging of mice with 2-photon microscopy. 205(2):357–363.

[9] Nicholas G. Horton, Ke Wang, Demirhan Kobat, Catharine G. Clark, Frank W. Wise, Chris B. Schaffer, and Chris Xu. *In vivo* three-photon microscopy of subcortical structures within an intact mouse brain. *Nat. Photonics*, 7(3):205–209, March 2013.

[10] Cheng Huang, Jessica R. Maxey, Supriyo Sinha, Joan Savall, Yiyang Gong, and Mark J. Schnitzer. Long-term optical brain imaging in live adult fruit flies. 9(1):872.

[11] Laurence T. Hunt and Benjamin Y. Hayden. A distributed, hierarchical and recurrent framework for reward-based choice. 18(3):172–182.

[12] Kei Ito, Kazumi Suzuki, Patricia Estes, Mani Ramaswami, Daisuke Yamamoto, and Nicholas J. Strausfeld. The organization of extrinsic neurons and their implications in the functional roles of the mushroom bodies in drosophila melanogaster meigen. 5(1):52–77.

[13] Na Ji, Jeremy Freeman, and Spencer L. Smith. Technologies for imaging neural activity in large volumes. 19(9):1154–1164.

[14] Talia N. Lerner, Li Ye, and Karl Deisseroth. Communication in neural circuits: Tools, opportunities, and challenges. 164(6):1136–1150.

[15] Yen-Yin Lin, Ming-Chin Wu, Po-Yen Hsiao, Li-An Chu, Mei-Mei Yang, Chien-Chung Fu, and Ann-Shyn Chiang. Three-wavelength light control of freely moving drosophila melanogaster for less perturbation and efficient social-behavioral studies. 6(2):514–523.

[16] Susan Lindquist. Varying patterns of protein synthesis in drosophila during heat shock: Implications for regulation. 77(2):463–479.

[17] Liqun Luo, Edward M. Callaway, and Karel Svoboda. Genetic dissection of neural circuits: A decade of progress. 98(2):256–281.

[18] Henry Ltcke, David J. Margolis, and Fritjof Helmchen. Steady or changing? long-term monitoring of neuronal population activity. 36(7):375–384.

[19] Alexander Mathis, Pranav Mamidanna, Kevin M. Cury, Taiga Abe, Venkatesh N. Murthy, Mackenzie Weygandt Mathis, and Matthias Bethge. DeepLabCut: markerless pose estimation of user-defined body parts with deep learning. 21(9):1281.

[20] D. J. McFarland. Decision making in animals. 269(5623):15.

[21] Daiana Minocci, Elena Carbognin, Meena Sriti Murmu, and Jean-Ren Martin. In vivo functional calcium imaging of induced or spontaneous activity in the fly brain using a GFP-apoaequorin-based bioluminescent approach. 1833(7):1632–1640.

[22] John A. Nevin. *The Study of Behavior: Learning, Motivation, Emotion, and Instinct*. Scott, Foresman. Google-Books-ID: Uct9AAAAMAAJ.

[23] Dimitre G. Ouzounov, Tianyu Wang, Mengran Wang, Danielle D. Feng, Nicholas G. Horton, Jean C. Cruz-Hernndez, Yu-Ting Cheng, Jacob Reimer, Andreas S. Tolias, Nozomi Nishimura, and Chris Xu. In vivo three-photon imaging of activity of GCaMP6-labeled neurons deep in intact mouse brain. 14(4):388–390.

[24] David Owald and Scott Waddell. Olfactory learning skews mushroom body output pathways to steer behavioral choice in drosophila. 35:178–184.

[25] Keram Pfeiffer and Uwe Homberg. Organization and functional roles of the central complex in the insect brain. 59(1):165–184.

[26] Kaspar Podgorski and Gayathri Ranganathan. Brain heating induced by near-infrared lasers during multiphoton microscopy. 116(3):1012–1023.

[27] Davide Raccuglia, Li Yan McCurdy, Mahmut Demir, Srinivas Gorur-Shandilya, Michael Kunst, Thierry Emonet, and Michael N. Nitabach. Presynaptic GABA receptors mediate temporal contrast enhancement in drosophila olfactory sensory neurons and modulate odor-driven behavioral kinetics. 3(4).

[28] Johannes D. Seelig, M. Eugenia Chiappe, Gus K. Lott, Anirban Dutta, Jason E. Osborne, Michael B. Reiser, and Vivek Jayaraman. Two-photon calcium imaging from head-fixed *Drosophila* during optomotor walking behavior. 7(7):535–540.

[29] Johannes D. Seelig and Vivek Jayaraman. Neural dynamics for landmark orientation and angular path integration. 521(7551):186–191.

[30] Julie H. Simpson and Loren L. Looger. Functional imaging and optogenetics in drosophila. 208(4):1291–1309.

[31] Supriyo Sinha, Liang Liang, Eric T. W. Ho, Karel E. Urbanek, Liqun Luo, Thomas M. Baer, and Mark J. Schnitzer. High-speed laser microsurgery of alert fruit flies for fluorescence imaging of neural activity. 110(46):18374–18379.

[32] Nicholas J. Strausfeld, Lars Hansen, Yongsheng Li, Robert S. Gomez, and Kei Ito. Evolution, discovery, and interpretations of arthropod mushroom bodies. 5(1):11–37.

[33] Karel Svoboda and Ryohei Yasuda. Principles of two-photon excitation microscopy and its applications to neuroscience. 50(6):823–839.

[34] Xiaodong Tao, Hui-Hao Lin, Tuwin Lam, Ramiro Rodriguez, Jing W. Wang, and Joel Kubby. Transcutical imaging with cellular and subcellular resolution. 8(3):1277–1289.

[35] Niko Tinbergen. *The study of instinct*. Oxford University Press.

[36] Joshua T. Trachtenberg, Brian E. Chen, Graham W. Knott, Guoping Feng, Joshua R. Sanes, Egbert Welker, and Karel Svoboda. Long-term in

vivo imaging of experience-dependent synaptic plasticity in adult cortex. 420(6917):788.

[37] Jing W. Wang, Allan M. Wong, Jorge Flores, Leslie B. Vosshall, and Richard Axel. Two-photon calcium imaging reveals an odor-evoked map of activity in the fly brain. 112(2):271–282.

[38] Mengran Wang, Chunyan Wu, David Sinefeld, Bo Li, Fei Xia, and Chris Xu. Comparing the effective attenuation lengths for long wavelength in vivo imaging of the mouse brain. 9(8):3534–3543.

[39] Tianyu Wang, Dimitre G. Ouzounov, Chunyan Wu, Nicholas G. Horton, Bin Zhang, Cheng-Hsun Wu, Yanping Zhang, Mark J. Schnitzer, and Chris Xu. Three-photon imaging of mouse brain structure and function through the intact skull. 15(10):789.

[40] Tanya Wolff, Nirmala A. Iyer, and Gerald M. Rubin. Neuroarchitecture and neuroanatomy of the drosophila central complex: A GAL4-based dissection of protocerebral bridge neurons and circuits. 523(7):997–1037.

[41] Xiaojun Xie, Masashi Tabuchi, Matthew P Brown, Sarah P Mitchell, Mark N Wu, and Alex L Kolodkin. The laminar organization of the drosophila ellipsoid body is semaphorin-dependent and prevents the formation of ectopic synaptic connections. 6:e25328.

[42] Ryosuke Yagi, Yuta Mabuchi, Makoto Mizunami, and Nobuaki K. Tanaka. Convergence of multimodal sensory pathways to the mushroom body calyx in *Drosophila melanogaster*. 6:29481.

[43] Nilay Yapici, Manuel Zimmer, and Ana I. Domingos. Cellular and molecular basis of decisionmaking. 15(10):1023–1035.

[44] Zhihao Zheng, J. Scott Lauritzen, Eric Perlman, Camenzind G. Robinson, Matthew Nichols, Daniel Milkie, Omar Torrens, John Price, Corey B. Fisher, Nadiya Sharifi, Steven A. Calle-Schuler, Lucia Kmecova, Iqbal J. Ali, Bill Karsh, Eric T. Trautman, John A. Bogovic, Philipp Hanslovsky, Gregory S. X. E. Jefferis, Michael Kazhdan, Khaled Khairy, Stephan Saalfeld, Richard D. Fetter, and Davi D. Bock. A complete electron microscopy volume of the brain of adult drosophila melanogaster. 174(3):730–743.e22.